Thermal-Stress Characteristics of Large Area Additive Manufacturing

by

Brian K. Friedrich II

Submitted in Partial Fulfillment of the Requirements

for the Degree of

Doctor of Philosophy

in the

Materials Science and Engineering

Program

YOUNGSTOWN STATE UNIVERSITY

May, 2022

Thermal-Stress Characteristics of Large Area Additive Manufacturing

Brian K. Friedrich II

I hereby release this dissertation to the public. I understand that this dissertation will be made available from the OhioLINK ETD Center and the Maag Library Circulation Desk for public access. I also authorize the University or other individuals to make copies of this thesis as needed for scholarly research.

Signature:

_____

Brian K. Friedrich II, Student Date

Approvals:

_____

Dr. Kyosung Choo, Thesis Advisor Date

_____

Dr. Jae Joong Ryu, Committee Member Date

_____

Dr. Donald Priour, Committee Member Date

_____

Dr. Brian Cockeram, Committee Member Date

_____

Dr. Matthew Caputo, Committee Member Date

_____

Dr. Salvatore A. Sanders, Dean of Graduate Studies Date

ABSTRACT

Common failure modes to Big Area Additive Manufacturing (BAAM) are the phenomenon of slumping and excessive distortion. Slumping or sagging usually occurs when the printed structure retains excessive heat. This phenomenon is commonly seen when the build has insufficient cooling between layers and, therefore, inadequate mechanical strength due to the high-temperature material properties to support the layers above. Distortion is the planar deviation from the desired geometry. Significant residual stresses typically distort BAAM builds. Stresses often occur due to the thermal cycling and large temperature gradients found in additively manufactured parts. This study developed a transient thermal and structural simulation model to predict the slumping phenomenon and distortion, specifically applicable to overhanging features. A pyramidal model was crafted in Ansys Workbench software to simulate a large layer overhang to investigate the necessary slumping conditions. The pyramid was designed to have 53 layers and utilized symmetry to reduce the pyramid to one-quarter of the overall size and was modeled using standard ABS material. The simulation model matches the dimensions in the experimental pyramid, which had bead dimensions of 12.5 mm wide with a thickness of 5 mm. The overall structure size was 1.06 m by 0.77 m by 0.43 m. Each layer in the model independently allows for element birth/death commands and individual layer mesh parameters. The built-in element birth/death commands enable the layers to activate and progress the same way as the experimental build. As each new layer is activated, a temperature input of 200°C is applied then turned off just as the next layer is activated.

The feedstock material selected for this study is Acrylonitrile Butadiene Styrene (ABS), which was selected based on the physical properties and the availability of the temperature-dependent material properties. The availability of these temperature-dependent material properties is essential to consider during simulation since the thermo-physical properties will significantly impact the accuracy of both the thermal and structural models.

The transient thermal finite element analysis (FEA) simulation allows for customization of dwell times, allowing designers to determine when the threat of slumping is no longer predicted. The transient thermal FEA analysis reported in this work showed consistent results with the numerical method for layer temperature. This agreement shows the assumptions made in both evaluations are valid and can be used in other studies to compare against experimental builds for other materials and geometries. The experimentally measured part was also in excellent agreement with the temperature profile results from the thermal model simulation. The experiment and simulation compared results agreed within 5 %.

Additionally, the results collected in this work show an exponential temperature distribution of the build as it cools. Exponential cooling was expected as it is often seen with similar materials and offers increased stability in the printed part since the material will solidify quickly and reach low-temperature material properties soon after. It was also observed that as the print height increased, more of the immediate layers underneath had increased temperatures. The increase in temperature is due to the reduced layer print times as the height increases, reducing the overall cooling time. A mechanical structural analysis determined the deflection of each layer as the build progressed. The in-plane

deflection for both the simulation and experimental build was in good agreement, and both showed more significant deflection in the areas of high heat retention. The increase in the height of the model also increased the number of layers above the glass transition temperature. This observation was consistent with the experimental and thermal simulations results and is likely the cause for slumping.

The structural simulation was used to determine the local distortion created during a BAAM build. The simulation was built off the thermal simulation coupling the two simulations. The model was set up to recreate the environment and printing process of the experimentally produced pyramid. The model used ABS temperature-dependent material properties reported in literature, gravity, and the time-history thermal profile as the inputs. The thermal-history results from the thermal simulation were coupled with the structural simulation to effectively relate the temperature profile to distortion estimated by the structural simulation. The simulation results and experimental build measured distortions were in good agreement. Additionally, the stress profile of the model indicates that slumping is caused by geometry, heat retention, and material properties.

Acknowledgements

I want to express the utmost gratitude to my dissertation advisor, Dr. Kyosung Choo. Thank you for all of your guidance and help throughout our time together. I can confidently say that working with you has made me a better engineer and scientist.

I also want to thank all the members of my dissertation committee, Dr. Brian Cockeram, Dr. Matthew Caputo, Dr. Jae Joong Ryu, and Dr. Donald Priour. Thank you for all of your help and guidance in completing this dissertation.

I am also very grateful to the friends I made at Youngstown State University. Bharat Yelamanchi, Angel Diosdado De la Pena, Aspen Glaspell, Kerry Johnson, Tim Daugherty, Elizabeth Zell, Mike Juhasz, Kyle Myers, Travis Kneen, Ram Gullapalli, and to all the others who have helped me along the way, I cannot thank you enough.

I am also grateful for all of the help, guidance, and patience from Dr. Clovis Linkous.

There are not enough words to express how lucky I am to have such a fantastic support group with my family and friends. All my successes are largely due to the guidance and love from my parents. Thank you both for everything. To my sister and brother, thank you for always being there for me. Your support and friendship have meant everything.

Lastly, my girlfriend Katie, you have been incredibly supportive, patient, and understanding. I cannot thank you enough for always being there for me and for your constant encouragement.

Contents

List of Figures

1 INTRODUCTION

Additive manufacturing (AM), also generally known as 3D printing, traditionally creates the desired geometry by building up feedstock material layer-by-layer. Fused Deposition Modeling (FDM) is one of the most used AM techniques for 3D printing polymer structures. FDM uses a solid wire-like filament that gets heated to the melting point, extruded through a nozzle, and deposited onto a substrate or previously extruded layers. This process allows for creating complex geometries, which would be impractical or unobtainable with traditional subtractive manufacturing [1-9].

Big Area Additive Manufacturing (BAAM) was developed in the Manufacturing Demonstration Facility of Oak Ridge National Laboratory (ORNL). BAAM operates on a much larger scale when compared to with traditional FDM build sizes, with build volumes exceeding one meter cubed [10-12]. Like BAAM, the primary benefits of 3D printing extend to the more general case of Large Area Additive Manufacturing (LAAM). The benefits of LAAM include:

- the creation of complex geometries,
- increased build sizes,
- the elimination of hard tooling (for as-printed conditions), and
- the paradigm of direct digital manufacturing [5].

An example of direct digital manufacturing with LAAM was demonstrated in 2014 when Local Motors (Phoenix, AZ), in partnership with ORNL, fabricated a customized automobile's shell during the 2016 SAE World Congress conference in Detroit [13]. This example demonstrates the impressive advantages LAAM offers as compared to other manufacturing methods.

While there are clear advantages in utilizing AM over traditional subtractive manufacturing methods, such as large scope in design complexity, ability for rapid prototyping, and small batch productions; the process also presents inherent drawbacks [1]. One of the most noteworthy drawbacks for the FDM process is the need optimize the processing-structure-property relationship. This optimization process often requires an experimental design that incorporates statistical analysis or trial-and-error experimentation to better understand special path programming, printing parameters, and adjusting material properties to affect the end quality of the part [10-12]. However, process optimization by employing trial and error is time-consuming and expensive. Modeling and analyzing the print process can reduce the effort needed to optimize the print effectively, by dialing-in on the proper process parameters and material specific considerations, the build can be completed in the first attempt. Modeling the print process will also aid in predicting how existing AM materials and new AM materials, such as thermosetting polymers, such as Acrylonitrile Butadiene Styrene (ABS), will perform while undergoing the printing process [14].

The purpose of this research is to predict and determine controlling factors in material extrusion AM distortion. Material extrusion and most other types of AM are susceptible to distortion caused by thermal cycling and large temperature gradients. The printing process for material extrusion AM (e.g., FDM) deposits feedstock material at the melting point temperature, this new layer often has a much greater temperature than the previous layer. Thermal cycling occurs when the new layer is deposited, the thermal energy from the new layer is transferred to the previous layers and to the environment. Therefore, the previous layers exhibit cyclical temperature history due to the transfer of thermal energy from the new layers. In addition to the thermal cycling, large temperature gradients can be present in a build. As noted previously, the

new layer temperature is much greater than the previous layers, and the material used in FDM and similar AM methods often exhibit an exponential decrease in temperature from the top layer to the bottom layer (exponential cooling), which creates larger temperature gradients in a smaller number of layers. Materials that exhibit exponential cooling are often preferred for FDM because previous layers reach stable structural material properties quicker to be able to support the rest of the build. However, this exponential cooling also invites thermal distortion caused by the large temperature difference. Thermal distortion is caused by expansion and contraction of the material as the temperature of the layers change. These opposite forces create residual stresses, which distort the build. More specifically, in the case of large temperature gradients the contracting material at the top layer pulls against the base layers which are already at the print chamber temperature and no longer changing due to temperature. As the build increases in height, the residual stresses building up in the part can also increase, further distorting the part from the desired geometry. Similarly, the cycling temperature can cause local deformations when the material is contracting or expanding against other layers.

This research presents a method to predict thermal distortion for a material extrusion build. Thermal and structural simulations offer the ability to estimate the temperature profile of a build during the entire printing process. By coupling the thermal-history and structural simulations, the commercial software used for the analysis can show the thermal profile, associated distortion, and residual stress any area of interest or concern. Simulating the build before experimentally creating a complicated part can offer substantial time savings and material costs. The time needed to create a model and apply the correct boundary conditions is much less than the time needed to experimentally create the part and then evaluate the features of interest. The simulation can also be used to run different scenarios (e.g., different chamber temperatures,

material properties, and dwell times) that otherwise would require multiple experimental builds. The benefits of simulating material extrusion AM are exponentially increased for larger builds. As the time and material needed to build increase, the benefits of simulating the results of the build before experimentally building become increasingly important.

2 PURPOSE

This study investigates the effect heat retention has on the structural stability of a part created by additive manufacturing. As mentioned in the Introduction, there are still unexplored phenomena that occur as a direct result of the AM process. This objective of this work is to identify and explore some of those phenomena through large build AM and by means of numerical modeling (ANSYS). To date, and based on the literature, the following phenomena or characteristics have been identified as areas of interest for this work:

1. Determine the temperature profile of an AM part numerically.
2. Develop a finite element analysis (FEA) thermal model to simulate the printing process.
3. Compare the model to the experimental results to ensure the model accurately represents the AM process.
4. Using the output from the thermal model, simulate the structural stability or deformation of the model during the printing process.
5. Study the sagging phenomenon during the BAAM process. Sagging occurs when there is an overhanging or bridging feature present, and the weight of the material applies a load more significant than the yield strength, generally at elevated temperatures, of the material supporting the feature.
6. Compare the results from the structural simulation to the failure seen during experimental results.

In addition to this list, ABS material properties are explored. For the simulation to produce realistic results the material properties need to be close to or exact to the real values. Different

material characterization techniques and testing were utilized to determine the temperature dependent material properties required for the simulations. These properties are further detailed in Section 3.10.3.

3 LITERATURE REVIEW

The additive manufacturing process studied in this research work is material extrusion. The thermal and mechanical effects on the material are unique for this type of additive manufacturing. An overview of the significant types of additive manufacturing is given initially in this chapter to understand the differences between each method. Material extrusion is detailed further in this chapter since it is the AM technique used in this report. More precisely, the description will consist of its operation, benefits, challenges, and part shape challenges.

3.1 ADDITIVE MANUFACTURING

This section summarizes the different types of additive manufacturing (AM) processes as delineated by ASTM [15-16]. Additionally, there will be a description of the materials used in each kind of AM and their advantages and disadvantages technological advances needed in the AM field. This section will also include a brief history of additive manufacturing.

The term additive manufacturing means creating a product by the addition of material. Rapid prototyping (RP) and three-dimensional (3D) printing are both terms generally used to describe additive manufacturing. RP stuck since prototype models were the main application for this technology [1-3]. This technology allowed for the relatively quick manufacturing of one-off parts.

After this technology became a prevalent manufacturing technique, it was improved to produce end-line products needing little or no post-processing steps. Due to the advancements and popularity, ASTM International created a committee to agree on new terminology for this technology. They decided on the term additive manufacturing. Even more recently, the

committee also decided to break the AM technology into the following seven unique processes: material extrusion, material jetting, powder bed fusion, sheet lamination, binder jetting, directed energy deposition, and vat photopolymerization [17-18]. Each method differs based on the way the material adds to itself. Each of the processes discussed adds material in layers based on the model's design. ISO/ASTM 52900 also provides some guidance to the AM processes available today [18].

The earliest technologies, Stereo Lithography (SLA) and Laminated Object Manufacturing (LOM), provided little more than prototypes that could be used as showpieces or generally to determine fits and conceptual function since the part was of weak structural strength. In addition, LOM structures manifested as paper models and SLA structures embodied in brittle acrylates were inferior to engineered thermo-polymers [14]. Today the Additive Manufacturing technologies have matured into various technologies that yield parts with high dimensional accuracy and improved strength.

Computer-aided design (CAD) is used to create the model, which the different AM processes will then produce. AM relies on the proper CAD design for a successfully manufactured part. Without CAD, AM would not be possible as it functions today.

3.2 History and Timeline of AM

Since the first patent, placed in the 1980s, companies and researchers have competed to create the best machines for additive manufacturing. As this technology has become available to the masses, a new industry frontier has become open to anyone. Today, home 3D printers are available to anyone interested in the technology.

The timeline for AM really starts in 1980 with Hideo Kodama, who filed the first AM patent. The patent describes a photopolymer rapid prototyping technique that utilizes UV light to

cure the material. This version of rapid prototyping did not gain traction when compared to the 1983 invention of stereolithography apparatus (SLA) [1, 19]. Charles Hull invented the SLA machine and then went on to form 3D Systems Corporation in 1986 [20]. SLA printers use light-reactive thermoset materials or resins. Solid geometries are created by directing specific wavelengths of light into the resin, allowing short molecular chains to join, building up into the desired geometry. The next advancement in rapid prototyping occurred in 1987 when Carl Deckard filed a patent for the selective laser sintering (SLS) process [1, 19-20]. SLS uses a high-power laser to sinter select areas on a bed of polymer powder or particles. Post sintering, another layer of powder is pushed onto the bed, and the process repeats until the part completes. This method generally requires post-processing to get the desired finish. Another new AM technology came around in 1989, with the advent of Fused Deposition Modeling (FDM) [19-20].

Further advancements wouldn't be made until 1997 when AeroMat produced the first 3D printed metal process using the Laser Additive Manufacturing (LAM) process [19]. LAM is a parent term that encompasses SLA, SLS, and Selective Laser Melting (SLM). In this case, AeroMat produced the first SLM [19].

Since the last significant advancement in AM process and method in 1997, there have been essential milestones with what can be produced with AM. Two of the notorious achievements were in 1999, Wake Forest Institute of Regenerative Medicine printed an organ for transplant, and in 2011 when the University of Southampton 3D printed the first uncrewed aircraft [19]. As the patents have been expiring, there are now over 170 3D printing system manufacturers in the world [19].

3.3 Computer-Aided Design (CAD)

CAD software is a staple in the engineering community. There is not much designed today that does not use CAD software. CAD software has improved significantly since its creation. Some versions allow for the creation of parts specifically for AM or other manufacturing techniques. Versions also allow for mechanical and thermal simulations based on the conditions the structure will see. In addition, to improve the understanding that material selection has on the designs, many versions of CAD software include the material properties in evaluating the manufacturing process. CAD programs allowed for Computer-Aided Manufacturing (CAM). CAM provides the coding for robotic manufacturing techniques, such as computer numerical controlled (CNC) subtractive manufacturing [1, 21]. The code creates the path, process speeds, and tool selections to remove material from a stock piece to produce the designed part. CAM adapted to allow for AM processes. Generally, since the methods are reversed, models and code are not compatible between AM and subtractive manufacturing processes [21]. Therefore, if both AM and subtractive manufacturing create a similar part, only the CAD model will be the same. The manufacturing code will need to diverge based on either adding material or subtracting it.

Since the AM process creates parts layer-by-layer, the manufacturing code must reflect that process. Therefore, the manufacturing code slices the CAD model to represent the layer-by-layer building method [16]. The slicing method is like the previously discussed stereolithography technology. 3D Systems, a company at the dawn of AM technology, created the slicing algorithm and gave it the file extension of "STL." STL stands for Stereolithography [16, 21]. It is also known as Standard Triangle Language since it represents 3D structures by connecting

triangles with no overlaps or gaps. The STL file extension is the most common file format used in AM machines [16, 21].

3.4 VAT POLYMERIZATION

As mentioned previously, vat polymerization is one of the earliest forms of AM and is the umbrella term for similar additive processes. These processes include stereolithography (SLA), direct light processing, and masked stereolithography. These processes have minor differences between each other but, in general, function the same way.

Vat polymerization works using an ultraviolet (UV) light source to cure specific particles of a photopolymer resin to build up the object. The photopolymer resin is held in a vat, generally under the light source [1, 14]. Inside the vat is a platform to provide the initial build surface. The platform moves further into the resin to keep the top layer of the part just beneath the surface of the resin so the next layer can be cured. The light source path is generally the most significant difference between the different types of vat polymerization. The UV source is generally directed to move along a path using optics to create the part layer by layer [14, 17-18, 22]. The UV light can also be masked, where only the areas that require curing will be exposed to the light source at once. This process needs to change the "mask" for each layer, ensuring only certain areas are exposed to the UV source. Additionally, there is direct light processing or photon processing where the laser is directly used to create the part instead of relying on the masks or moving optic platforms. The details of the process are further explained in [14, 22].

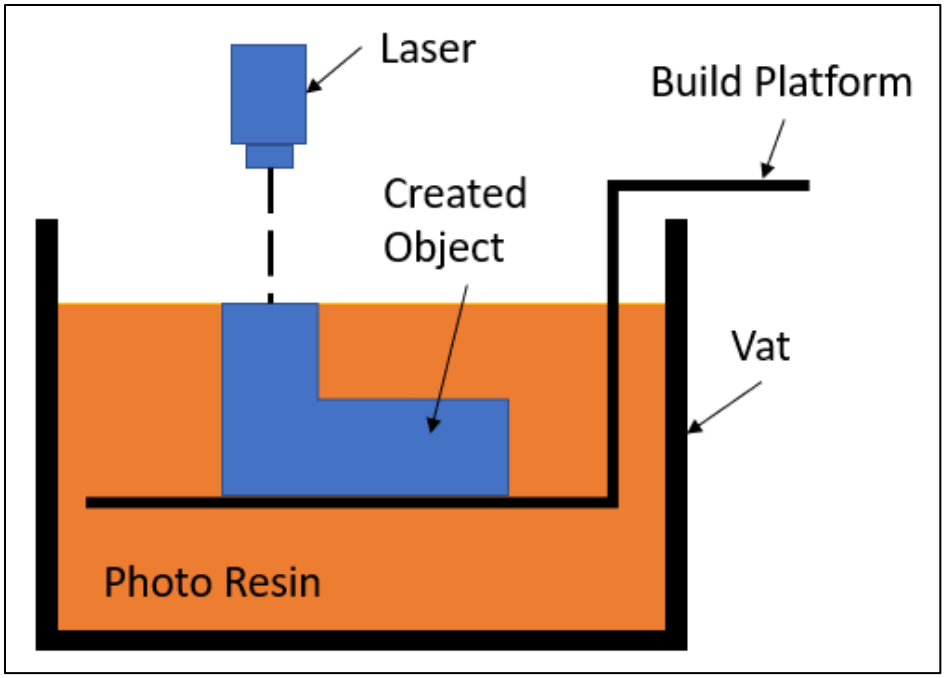

Figure 3-1. Vat polymerization diagram, showing typical features seen on commercial equipment.

Depending on the application, vat polymerization has some great benefits. However, it is not made to be used for much more than rapid prototypes. Some of the benefits include fast build times, the surface finish is generally smooth, and holding tight tolerances [2, 23]. These benefits make it very useful for rapid prototypes in most industries to visualize parts for fit and function. The disadvantages of vat polymerization include easily warped parts, hazardous material in the resin form, support structures that need to be removed from the post-production part, poor material properties, and limited part size to the confines of the vat [1, 22]. Additionally, anything designed for vat polymerization must include draining holes to allow the resin to escape after manufacturing.

3.5 Sheet Lamination

Sheet lamination (SL), also commercially known as Laminated Object Manufacturing (LOM), involves layering sheets of material on top of previously set layers. These sheets are adhered together using a variety of methods. Although for LOM, typically, they are bonded together by some thermal adhesive. After the sheets are bonded, a heated roller sets the adhesive and smooths any unwanted wrinkles. Next, a laser (CO_2) cuts the layer to its specified shape for the specific layer. A return spool then takes up the cut sheet, and the new clean sheet is rolled on, and the process continues [1-2, 17-18]. Any area that was not completely removed by the laser or is being used as a support layer typically has more minor crosshatching cuts to make removal easier once the part is made. This process works well for paper or wood materials; however, it gets more complicated when working with sheet metal. The process is similar, but the sheets are held together with brazing or, in some cases, mechanical clamps or fasteners [1, 14, 23].

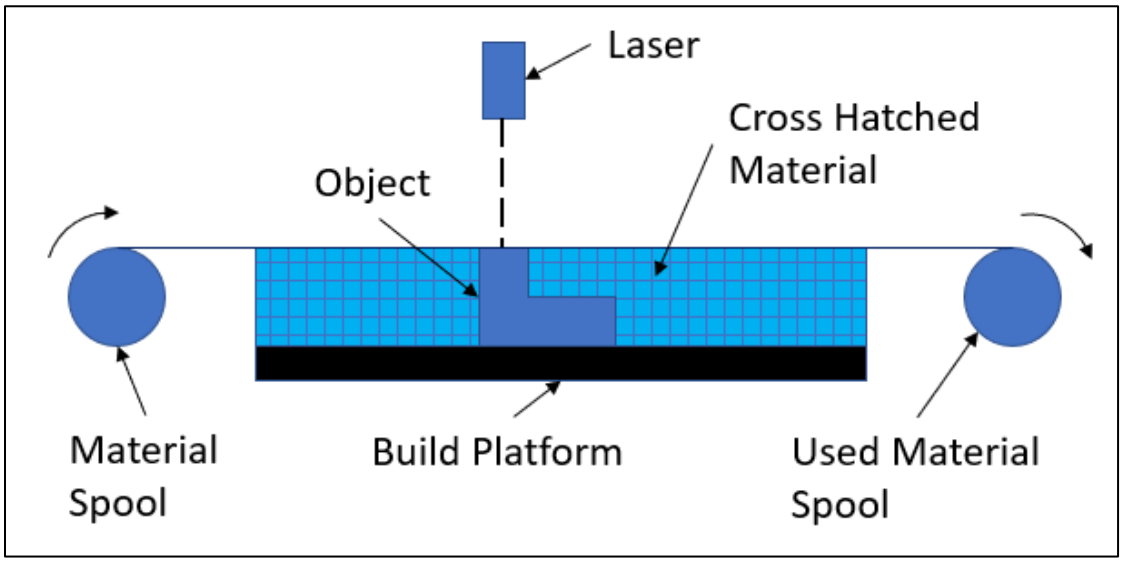

Figure 3-2. Sheet lamination diagram, showing typical features in commercial equipment.

Since these structures are being held together by adhesive or brazing, their mechanical properties are vastly different depending on the part's orientation. The anisotropic properties of these parts are crucial to consider when choosing the direction of the laminated sheet part.

This type of additive manufacturing technique has several advantages, including quick part building, low cost, little to no deformation or phase changes, being able to manufacture large parts, and no additional supporting structures are needed. These benefits make this AM technique great for prototyping [1]. However, there are also disadvantages to the SL. Several disadvantages include anisotropic properties, complex internal cavities that are difficult to build, complex parts that can be difficult to remove from the excess material, generally, there is a lower surface definition, generally poor mechanical properties, and there is a lot of wasted material with this method [14].

3.6 Selective Laser Sintering

During the development of this method at the University of Texas at Austin, it was initially called selective laser sintering (SLS) and was used primarily for plastic prototyping. The process has since been developed to be used on metals and even ceramics. There are only minor differences between powder bed fusion for metal, ceramics, and plastics. In general, powder bed fusion is defined as any process that uses thermal energy to fuse the powder to create parts selectively. The process for powder bed fusion starts with laying a powder material down and using a laser, or electron beam, to join the material together [1-2, 15, 22]. The main features involved in SLS are shown in Figure 3-3. The material is selectively joined by either sintering or melting the particles in the immediate area. Then, the powder bed stage is lowered, and another layer of powder is placed on top. The new coating is then sintered or melted to the previous layer, and the process continues until the part is finished [1-2, 14, 18, 23]. The powder bed fusion

printers can vary with laser power, spot size, layer thickness, and speed. There are three primary variants of powder bed fusion: SLS, selective laser melting (SLM), and direct metal laser sintering (DMLS) [2, 15, 17].

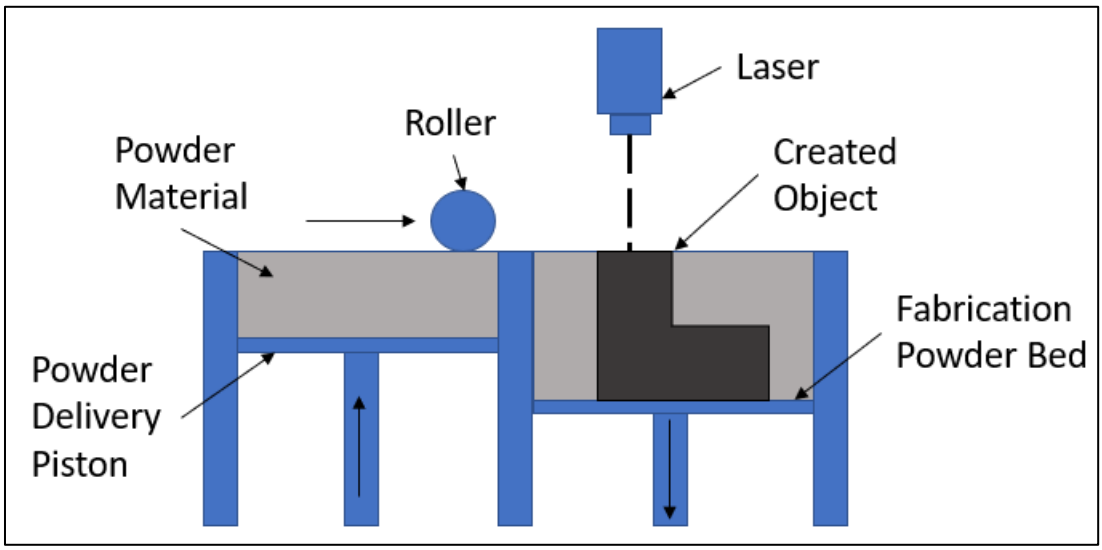

Figure 3-3. Selective laser sintering AM diagram shows typical features seen in commercial equipment.

SLS, which is typically only used for powdered polymer materials, operates by using a laser source to heat and fuse the powder. The powdered polymer generally is 50 to 90 micrometers in diameter [23]. The density of the final part depends on the size of the powder [23]. The more refined and more spherical the powder, the tighter packed the particles can be. The higher the packing density, the closer the density is to bulk material properties [2]. Direct metal laser sintering uses almost the same process as SLS. The only difference is powdered metal is used in place of the polymer and the system changes needed to accompany the higher melting temperatures of metals [1, 14].

Selective laser melting is very similar to SLS. The main difference is that SLM is used for metals and ceramics, and instead of simply sintering the layers and particles together, the

powder is melted to create higher density parts [1, 14, 23]. There are some significant advantages for all the types of powder bed fusion AM techniques in the commercial industries. Features can be built with no supports since the powder that was not sintered or melted acts as the support [20]. As long as the powdered material has sintering or melting temperature within the range of that achieved by the laser or electron beam, it is likely able to be used by this technique. The end product generally has good tolerances and typically high density [1-2, 20]. The leftover powder can also be recycled, making this process eco-friendlier. There are some disadvantages to the powder bed fusion process. First, like other layer buildup manufacturing processes, the surface finish will often require post-processing [1, 22]. Additionally, post-processing may need to be done since the parts are susceptible to warping due to the heat inputs [20, 22]. The machines themselves require specific atmospheric control to function correctly.

3.7 Directed Energy Deposition

Directed energy deposition (DED) is defined as a process that uses thermal energy to fuse the material by melting the material as it deposits [1, 17, 18]. DED is the umbrella name for this type of process. In the market, several slightly different techniques fall under this category.

Laser Engineered Net Shaping (LENS), Directed Light Fabrication (DLF), Directed Metal Deposition (DMD), 3D Laser Cladding, and Laser Direct Casting are all specific types of processes that utilize the same DED process [24]. DLF, LENS, DMD, 3D Laser Cladding, and Laser Direct Casting all vary with the method and type of laser used. Laser power, spot size, and type are all specific to the material, delivery method, and application [1, 24].

DED AM works by using a thermal source to melt the material fed onto the build plate instantly. The material can be fed to the build plate in powder form or as a filament wire. The build plate moves in the horizontal directions allowing for the planar shape of the part to be

created layer by layer. Once the layer is completed, the laser and feedstock nozzle move vertically to allow room for the next layer [2, 25]. Since the material is melted, the process allows for complete bulk density to be achieved [24].

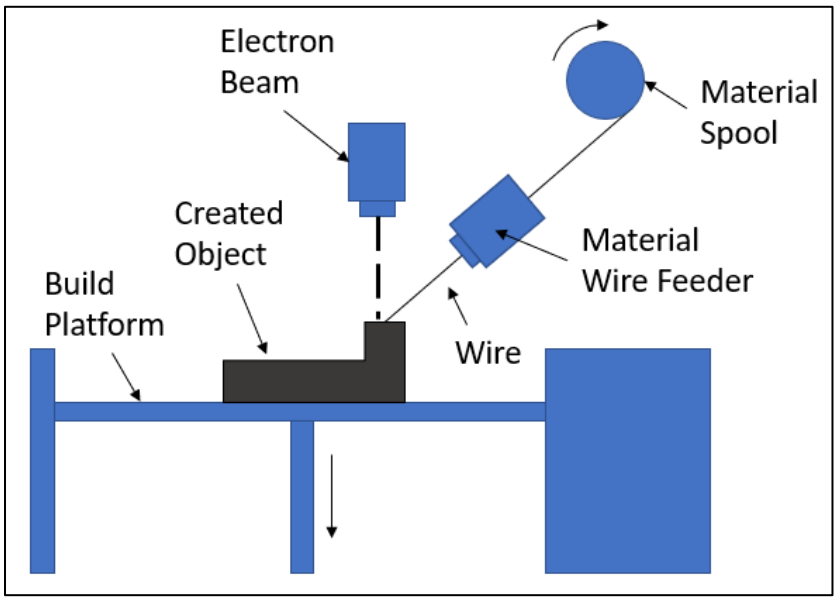

Figure 3-4. Directed energy deposition AM diagram, showing typical features seen in commercial equipment.

More often, DED methods are used on metallic parts. However, they can also be used for polymers, ceramics, and metal-ceramic materials [2]. DED can utilize multiple feed nozzles to fuse different materials, and it can even control the phase composition of the materials. DED is also often used to repair or coat preexisting components. Coating ceramics with metal or repairing a feature like welding gives this AM process a significant commercial appeal. The only disadvantages to DED are the poor surface finish created by feeding the material onto the build plate, it is a complicated process, and it can take a long time to build the component, and it also needs supports to produce more complicated parts [2].

3.8 Binder Jetting

Binder jetting combines some of the aspects from DED and powder bed fusion. Binder jetting is a process that uses a liquid bonding agent or adhesive to join powder materials selectively. Binder jetting operates by spreading powder with a counter-rotating roller or traversing blade. Once the powder is spread, a print head lays the binder down locally to hold the powder together. The build plate is then lowered to accommodate the next layer of powder. This process repeats until the desired shape of the component is created [2, 4, 18]. Once the printing process is completed, the part sits in the powder bed surrounded by the excess powder. The excess powder acts as support while the binder cures [1, 14, 17]. Letting the binder cure is essential so that when the part is removed from the powder bed, it can be handled without breaking. The next step for the printed component is sintering. The sintering process heats the structure until the solid powder bonds with the neighboring powder particles in the solid-state without reaching liquefaction. Some techniques compress the printed part before sintering to create closer packed particles and improve the component density. This process for printing has several advantages, it offers shorter build times, relatively inexpensive and reusable raw materials, and the support structures are built into the process [2, 26]. There are, however, some disadvantages as well, the parts are fragile before sintering and prone to collapse, poor surface finish, and low dimensional accuracy compared to the other methods discussed [1-2].

3.9 Material Jetting

Material jetting builds components in layers by depositing droplets of liquid materials using print heads. Typically, material jetting utilizes photopolymers and a curing source like UV light. The process for material jetting starts with heating up the liquid resin to reach an optimum viscosity for the resin. Once the resin is ready, the print head attached to the moving stage begins

to deposit the material to the desired locations. The UV light subsequently cures the photopolymer as soon as it hits the target surface. Next, the printing stage moves down to allow for the new layer, and the process continues [1, 14, 22]. Material jet printers vary in respect to the wetting properties of the material and layer height. Material jetting offers some of the smoothest AM parts when compared to the other methods. The components made through material jetting have homogeneous mechanical and thermal properties and generally high dimensional accuracy [2]. There are still some drawbacks when using this method. The material jetted parts have poor mechanical properties (i.e., low elongation at break), and since the material is photosensitive, they can degrade over time [23].

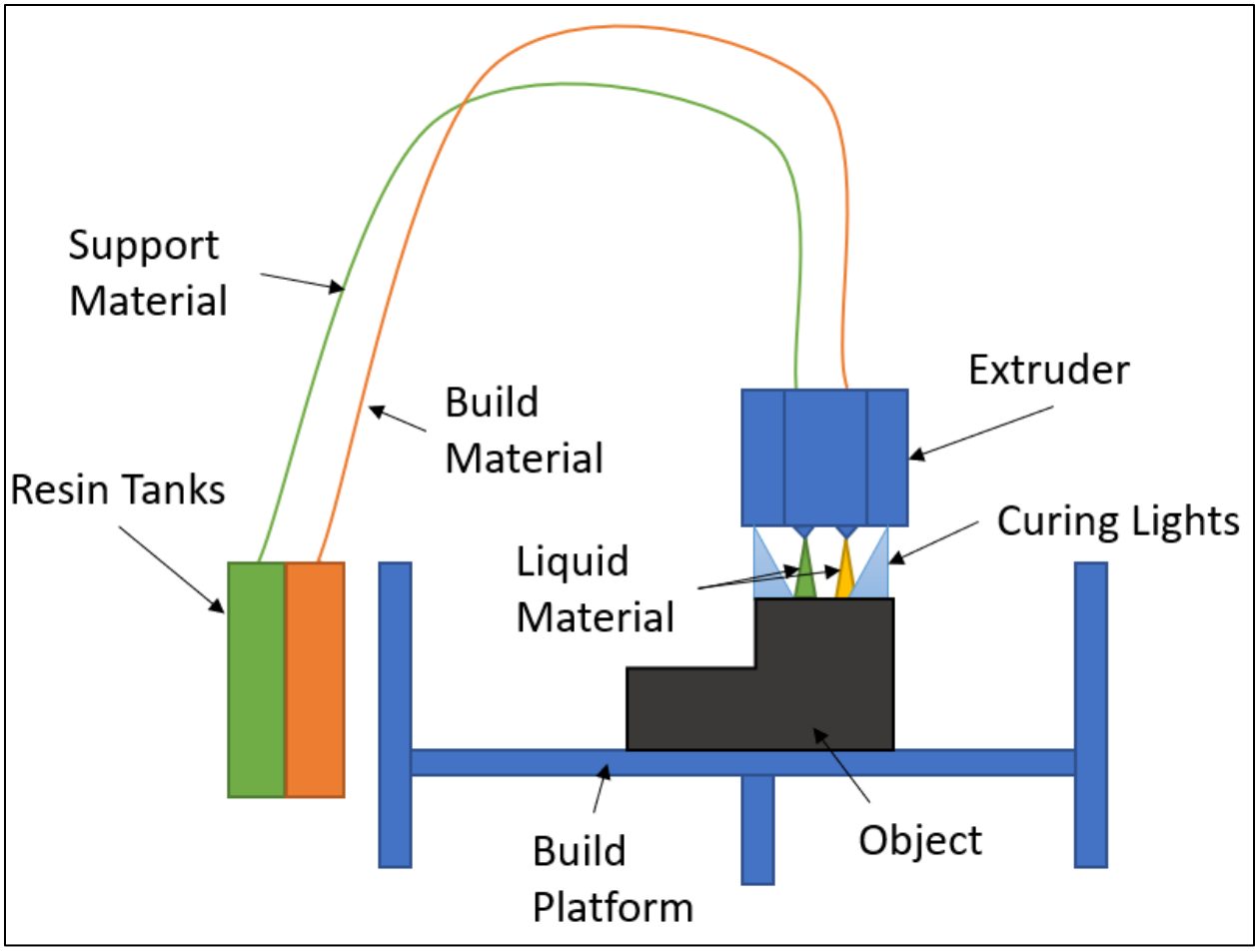

Figure 3-5. Material jetting AM diagram, showing typical features seen on commercial equipment.

3.10 Material Extrusion

3.10.1 Introduction

The AM technique of material extrusion was used in this research project; therefore, it is discussed in more detail than the other AM techniques. Material extrusion (MEX, ME-AM), Material extrusion AM is also referred to as fused filament fabrication (FFF), fused layer modeling (FLM), melt extrusion manufacturing (MEM), and fused deposition modeling (FDM) [17-18, 27]. It was developed in 1989 by Stratasys Inc., where it was initially called fused

deposition modeling [19]. Today, material extrusion has become a favorite for the at-home 3d printing enthusiast and expanded into an industry standard for rapid prototyping and actual production. This type of AM method is mainly used for polymers that are thermoplastics in nature [1-2, 14, 28].

There are a few variants to the material extrusion process. These variants are filament fed extrusion, rod extrusion, cold slurry extrusion, and pellet extrusion. For the filament-fed material extrusion process, a spooled filament is fed into a hot die by counter-rotating driving wheels in the material extrusion process [20, 28-30]. The die, sometimes referred to as an extruder, is at a temperature hot enough to cause the material to change to either a semi-solid phase or a temperature above the melting point [27-28, 31]. When the material passes through the extruder and nozzle, it contacts the target print surface. At this point, the extruded material is called a bead. The printed bead is then moved around by controlling the location of the nozzle with electromechanical actuators. Once the material extrudes for the first layer, the print head or base plate will translate vertically to allow room for the next layer [27-29]. At this point, either the production or support material is used to create this next layer. The process continues in this way until the part is completed. Typically, most material extrusion machines offer the ability to switch between the support material and the desired material for building the feature [3]. Since this AM process is one of the most popular globally, there are several different material extrusion equipment manufacturers [1, 16]. These manufacturers provide different levels of capabilities and functions. Some of the additional capabilities provided and options available for the printers are

- the heated print surface,
- isolated chambers for control of temperature,

- multiple material feeder,
- print kinematics (cartesian, delta, polar, SCARA),
- build volume sizes (ranging from small desktop printers to industrial building size printers),
- and a wide variety of printable materials (i.e., thermoplastics, resins, mixed fiber materials) [28].

For the rod extrusion process, the setup is very similar to the filament fed extrusion process. The only difference is the rods, which are larger in diameter and generally stiff, so they are pushed through the heating element and out through the nozzle by a piston or rollers [20, 27]. The cold slurry material extrusion process uses materials like concrete, which sit in a large hopper and are driven by screws or other mass movement methods to push the material out through the nozzle. Depending on the material, the material extrusion equipment will have a method to cure and solidify as it prints to ensure the structural stability of the build. The last type of material extrusion uses polymer pellets. The pellets sit in a hopper where a piston or screw pushes the pellets towards the nozzle. As the pellets make their way to the nozzle, they are heated to the desired temperature to promote proper bonding between the extruded layers and the other pellets [28, 32].

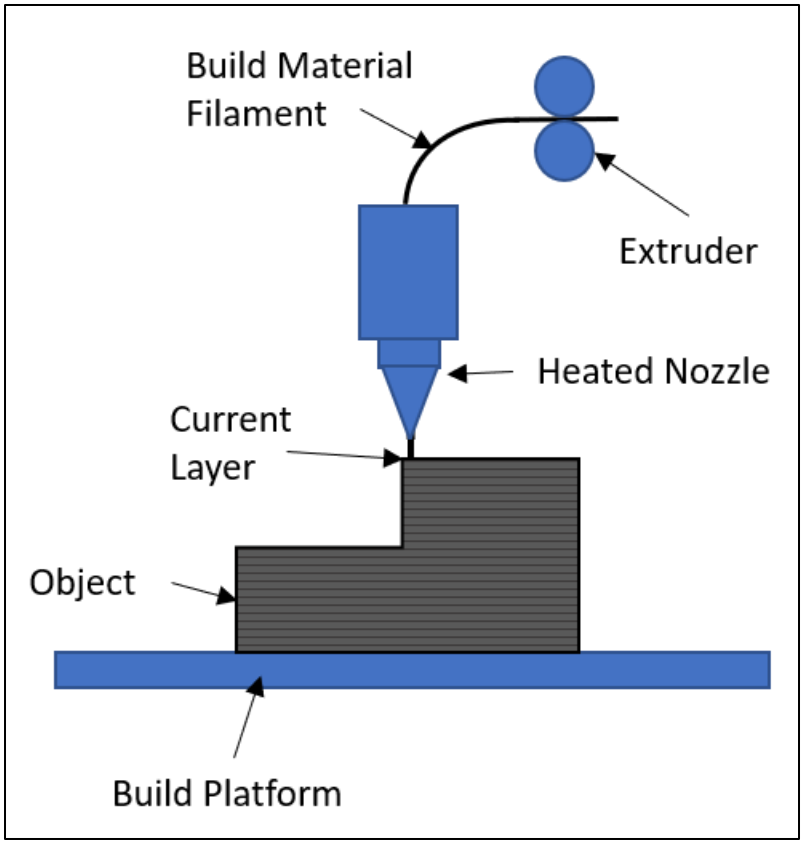

Figure 3-6. Material extrusion AM diagram, showing typical features seen on commercial equipment.

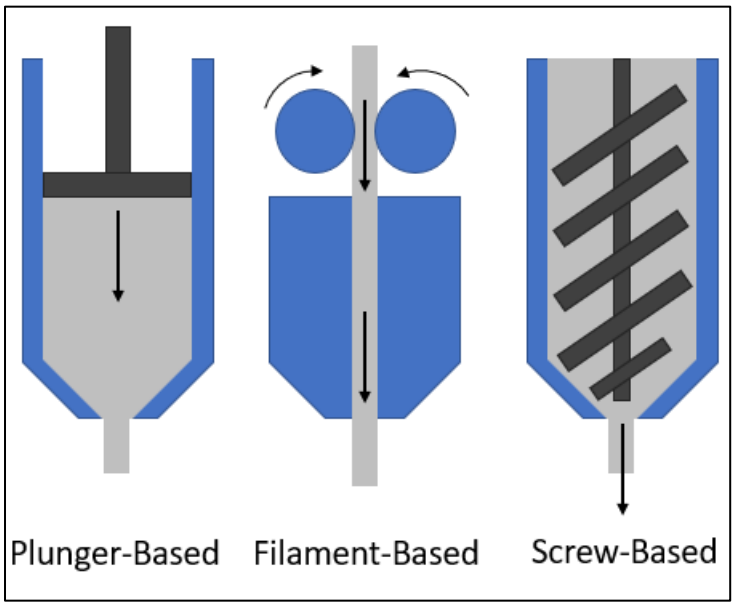

Figure 3-7. Material extrusion AM material feed options.

Material extrusion offers impressive advantages over other AM techniques, which is a reason for its growing popularity [2]. Material extrusion allows designers to use an ever-increasing number of materials, some of which offer very affordable prices. There is no need for resins to create the components. Generally, there is little to no post-processing needed for the part [2]. Material extrusion is not perfect, however. There are still disadvantages to choosing this AM process. Parts made by material extrusion have a poor surface finish. The process can take a substantial amount of time depending on the size of the build, layered parts are generally anisotropic in strength, material with large fibers may have porosity issues depending on the flow of material from the nozzle, and support material is needed for complex overhanging features [28].

The following sections will focus on more specific aspects of ME-AM. Including the materials used, applications, common issues attributing to build failures, process parameters, and ways to predict failure modes of material extruded builds.

3.10.2 Materials used in Material Extrusion Additive Manufacturing

Typically, each AM process discussed so far has had some strict material property needs, i.e., photopolymers and powdered metal. Material extrusion allows for metals, ceramics, polymers, and even combinations of these [1-2, 28]. As mentioned previously the material can start out as a resin, pellet, slurry, or even a metal filament. These options and the flexibility offered by material extrusion are some of the many reasons it has become so popular over the years. This section gives an overview of the materials typically used in Material Extrusion AM. There is extra emphasis on the polymers since the research presented herein, utilizes polymers, specifically Acrylonitrile Butadiene Styrene (ABS) [2].

3.10.2.1 Metals, Ceramics, and Fibers

Polymers are the most popular material for material extrusion AM. The popularity is due to the availability, cost, specific nature of thermoplastic material, and low extruder temperature for the material. Polymers, however, do not provide the same structural properties and support that metals, some ceramics, cement, or composites can provide. Material extrusion technology has adapted to using metals, composites, ceramics, wood fibers, and cement, and even mixed materials like carbon fiber reinforced polymers or metal powder infused polymers [2, 20, 33]. These materials give the material extrusion AM process more functionality and options for designers.

Metallic materials have been used in other AM processes like SLS and DMD, with high success [1-2, 20]. However, material extrusion with metallic materials is relatively new, but it is rapidly explored. The most common means of metallic material extrusion printing is by using fine metal powder in a binder system. The printed part is then sintered and then put through a process to remove the binder. The sintering functions the same as the other AM processes, where the metal is heated to a temperature suitable for bonding the powders together to form a part [1-2, 20, 34]. In contrast, the debinding process uses thermal, solvent, and catalytic methods to remove the binding material [35-36].

In the material extrusion process using the powder/binder system, the high consistency powder is mixed in with an organic multicomponent binder. The mixture of metallic powder to binder usually ranges from 50 to 80% in volume, depending on the application and material. Some common metals used are stainless steel, titanium alloys, aluminum, and tungsten [20]. The binders typically used are polymers or a form of wax. The mixture of metal powder and binder is a crucial factor when printing. If the mixture has too much powder, it can result in voids due to

poor processability, and in contrast, if there is not enough powder in the mixture, there can be significant distortion during the sintering process. The mixture also plays a significant role in the end material density, viscosity, material characteristics, mixing torque, and final mechanical properties [20].

The freshly printed parts are called "green" parts. Green is a general term for a newly formed part that has not yet been sintered and has no structural integrity at this point in time. After sintering, the printed structures become "brown parts." During the transition between green to brown parts, the sintering process sheds the binder material, and the part shrinks and increases in density [14, 37]. The sintering process causes one of more of the following mass transfer mechanisms: surface diffusion, lattice diffusion, grain boundary diffusion, evaporation-condensation, viscous flow of material, and plastic flow. These mechanisms control the material characteristics, porosity, final density, and microstructure, and size [20]. After the sintering process, if there is any binding material left after sintering, the debinding process can begin. Typical debinding uses a catalytic process involving nitric or oxalic acid at elevated temperatures. This process is done carefully to ensure a minimum number of impurities are included in the newly sintered part [35-36, 38].

Ceramics are another rapidly growing material extrusion-based material. Ceramics offer high strength, stiffness, strength, corrosion resistance, and more, making them a very versatile material. AM with ceramics generally uses a slurry-based process for most AM techniques. The slurry is a viscous suspension of ceramic powder (e.g., roughly 50% solid loading). Ceramic extrusion additive manufacturing (CEAM) uses a binder with ceramic powder, which is very similar to the metallic material extrusion process [35-36]. After printing the green samples, the solvent debinding baths are used to remove the sacrificial binders not needed to support the

structure before sintering. Sintering takes place in the same manner as the metallic extrusion AM process. The end product generally has 10 to 20% more porosity than what is expected [35-36]. Ceramic AM offers abilities that are usually out of reach for most common manufacturing methods, even with the higher porosity. Material extrusion can create functionally graded ceramics much easier and faster than most other manufacturing methods. Functionally graded ceramics start with one type of material and end with a different kind [9]. This is helpful when you need material properties that no one material offers [35-36].

For both metal and ceramics, the end material properties are not as good as traditional manufacturing processes. However, with interest in what material extrusion AM can offer industries, there is continued research in improving these methods [1].

Cement and concrete are the last materials discussed in this section. Material extrusion using mineral materials in the construction industry is becoming more common [1, 8, 39]. Typically, material extrusion of cementitious material is used to create slender elements like a roadside curb. However, since it is only used in a finite number of applications, this process has not been as developed as other material processes. Concrete behaves differently than most of the other material extrusion mediums. The material acts as a viscos-plastic material and exhibits non-Newtonian yield stress behavior [39-40]. Cement materials are also prone to water drainage, making them work like granular materials, making them harder to extrude. Due to the water drainage, extrudability plays a decisive role in determining the characteristics of the final material. Some of the ways researchers have combated the problems with extrudability is through systematically optimizing material mixtures to ensure a homogeneous mixture [39-40].

The extrusion process for cementitious materials is either by ram extrusion or screw extrusion [40-41]. These extrusion techniques utilize the same respective features discussed

previously. The ram extrusion process is not optimal due to the periodic refilling of material in the extrusion barrel. However, the ram extrusion process is generally used for study or other limited-run applications. Screw extrusion is the most common process. The screw function allows for the material to be continuously fed into the extruder. An additional piece of equipment that accompanies the screw extruder is a de-airing system, which increases the material density, strength, and durability by removing the entrapped air [39-40].

As the cement or concrete exits the extruder, the actuators move the concrete bead around to the programmed locations. Generally, as the cementitious material contacts the print surface or previous layer, the material needs to be adequately cured. Otherwise, the bead will begin to deform due to gravity. The material is unable to support itself without some drying or curing process. When the material is properly cured, it can be built into complete buildings and structures [40]. Since the systems being built are on the large side of AM builds, the equipment is often assembled in the desired location for the end structure. Portable cement material extrusion allows for building in remote areas where local build materials can be used.

3.10.2.2 Polymers and Composites

Polymers are by far the most common material used in the material extrusion process [2, 14, 22, 28]. Some of the most common polymers are:

- Acrylonitrile Butadiene Styrene (ABS)
- Polycarbonate (PC)
- Polystyrene (PS)
- Polylactic acid (PLA)
- Polyamide (PA)
- Polyethylene Terephthalate Glycol (PETG)

- Nylon
- Thermoplastic Polyurethane (TPE)
- High Impact Polystyrene (HIPS)
- Polyvinyl Alcohol (PVA)
- Acrylic Styrene Acrylonitrile (ASA)
- Polypropylene (PP)
- Polyoxymethylene (POM)
- Polymethyl Methacrylate (PMMA)
- PolyEther Ether Ketone (PEEK)

These materials are popular due to the availability, cost, and low extruder temperature for the material. The polymers listed have characteristics that allow for efficient flow, proper fusing, and harden quickly. Thermoplastic polymers, like the ones listed above, are typically used in material extrusion due to their low melting temperature, low thermal expansion coefficient, and high glass transition temperature, which allow for more minor internal stresses during the manufacturing process [14, 22].

Polymers, however, do not provide the same structural support and structural properties that metals, some ceramics, or composites can provide. Many polymers are mixed with additives (i.e., carbon and metal powders) to provide adequate support and strength to the printed part [2, 11]. These additives also improve mechanical properties, heat distortion, and thermal stability. Improvements in mechanical properties showed elastic modulus increases of over 150%; ultimate tensile strength could also be increased by over 40%, and lower elongation by almost 500% when tested in the printed direction [14, 32].

The material extrusion process relies heavily on the rheology of the molten filaments or pellets. Rheology is a crucial factor in determining if a new material can be adequately printed [42]. As a polymer is pushed through the nozzle, which decreases near the exit, shear and elongation flow are created. The molten polymer must have shear-thinning characteristics (reduction of viscosity as shear strain is applied) at elevated temperatures to allow for flow [28, 43]. This is a balancing act, and the material needs to have high viscosity at low shear rates to avoid premature extrusion and low viscosity at high shear rates to be extruded. The viscosity also controls how easily the molecules in the molten polymer can slide around [2, 28, 44]. If the molecules can move freely then, then the stored elastic energy is reduced in the extruded part. During the material extrusion process, polymer chains align with the flow direction. The end of the nozzle has the smallest diameter, and therefore the location for the greatest shear stress and creates a higher alignment of polymer chains [28, 45]. Generally, the polymer chains return to their initial state due to the elasticity of the polymer.

Since the material used in the experiment and simulation is ABS, the following section dedicates reporting more specific properties of ABS.

3.10.3 Acrylonitrile Butadiene Styrene (ABS)

Acrylonitrile Butadiene Styrene is often referred to as ABS. ABS is one of the most widely used polymers in AM and traditional manufacturing techniques. ABS is an impact-resistant thermoplastic and amorphous polymer [22]. Three monomers comprise ABS: Acrylonitrile, Butadiene, and Styrene [2, 44]. Acrylonitrile is a synthetic monomer created by combining propylene and ammonia. Butadiene is created through a by-product of ethylene production. Styrene is produced by the dehydrogenation of ethylbenzene [46]. Combining these three monomers provides a chemically resistant material, stable at wide temperature ranges,

increased toughness, impact strength, and relatively rigid when compared to most other polymers [32]. The standards used to define ABS materials are ISO 19062-1:2015, ISO 2580-1:2002, and ISO/ASTM 52903-1:2020. Therefore, the feedstock to feedstock variation for different manufacturers is expected to be minimal.

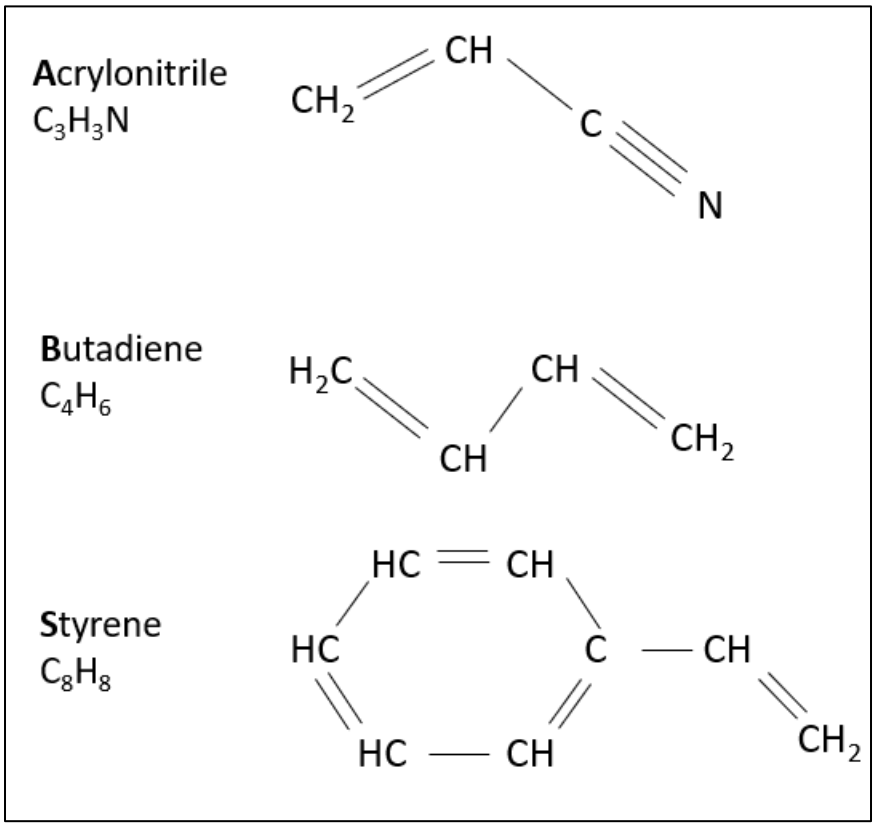

Figure 3-8. ABS structure.

ABS is created by emulsion techniques or continuous mass techniques [42, 46-47]. Emulsion polymerization occurs by the following process: a monomer is emulsified in a solution of surfactant and water which creates droplets, the extra surfactant forms micelles (an aggregate) in the water or oil, next a water-soluble initiator is used to react with the monomer in the micelles, the monomer in the micelle polymerizes, and the chain stops growing [48-49]. At this stage, the monomer has turned into a polymer particle. The monomers continue to diffuse into

the growing polymer particle. Eventually, the only remaining monomer is in the particles. This leaves the final product, a dispersion of polymer particles in water or oil. In the continuous mass technique or bulk polymerization, a soluble initiator is added to a pure monomer in a liquid state, where the initiator dissolves in the monomer [48-49]. A reaction then occurs when heated or exposed to radiation. The product of the reaction creates a viscous mass of polymers [48].

A variety of equipment can be used to process ABS. ABS's typical processing is by injection molding, blow molding, or extruding [32, 46]. The parts that come out of these processes have similar physical properties. ABS material properties are known to have high rigidity, good impact resistance, good insulating properties, good abrasion and stain resistance, good weldability, good dimensional stability over time, and high surface brightness when dyed [32, 46]. ABS also offers excellent chemical properties, such as high resistance to dilute acid and alkalis. ABS is also a thermoplastic which behaves as a thermoviscoelastic material, in that its viscosity decreases as it approaches a glass transition temperature and continues to reduce as it reaches its melting point. The viscosity will remain relatively high through its melting temperature making it desirable for material extrusion. Thermoplastics liquefy instead of burning, which allows them to be easily injection molded and then recycled [4]. They can be heated to their melting point, cooled, and reheated again without significant degradation in properties.

During the extrusion process, the material temperature at the nozzle is generally between 200 to 280C [28, 32, 50-52]. ABS prints, therefore, experience a temperature range from room temperature to at least 200C. Most material properties are a function of temperature, with ABS being no exception [53]. The following plots, Figure 3-9 through Figure 3-16, show a graphical summary of the mechanical material properties of ABS reported in the literature [55, 63, 64, 69,

74, 77, 81]. Two other material properties of ABS, which are not plotted, are emissivity and Poisson's ratio, which are 0.92 and 0.37, respectively, [16, 54].

Note that the material properties are assumed to be isotropic and homogeneous for this study. Any considerations for the lower strength of mechanical properties due to orientation are addressed in Section 4.3.4.

ABS storage modulus and loss modulus values as a temperature function are shown in Figures 3-9 and 3-10, respectively. Since ABS is a viscoelastic material, it is expected to behave both perfectly elastic and as a viscous element. Therefore, the storage modulus is reported since it quantifies the amount of energy required to distort the sample, which occurs under low stress in the elastic region. The loss modulus is reported since it quantifies viscous response of the material under low stress. Distortion in the elastic region generally shows a viscous element to the material. Therefore, under load there is a time independent elastic strain and a time dependent viscous flow. The storage modulus and loss modulus values (combined the storage modulus and loss modulus are called the dynamic modulus) used in this study were based on the dynamic mechanical analysis (DMA) in [55]. DMA is a common technique used to determine elastic and viscous responses of polymers under oscillating load and monitored against temperature, time, and frequency [56-58]. The oscillating load stresses the material where the resulting strain is measured. The measured stress, strain, and parameters can then be related to the complex modulus or, more specifically, the storage modulus.

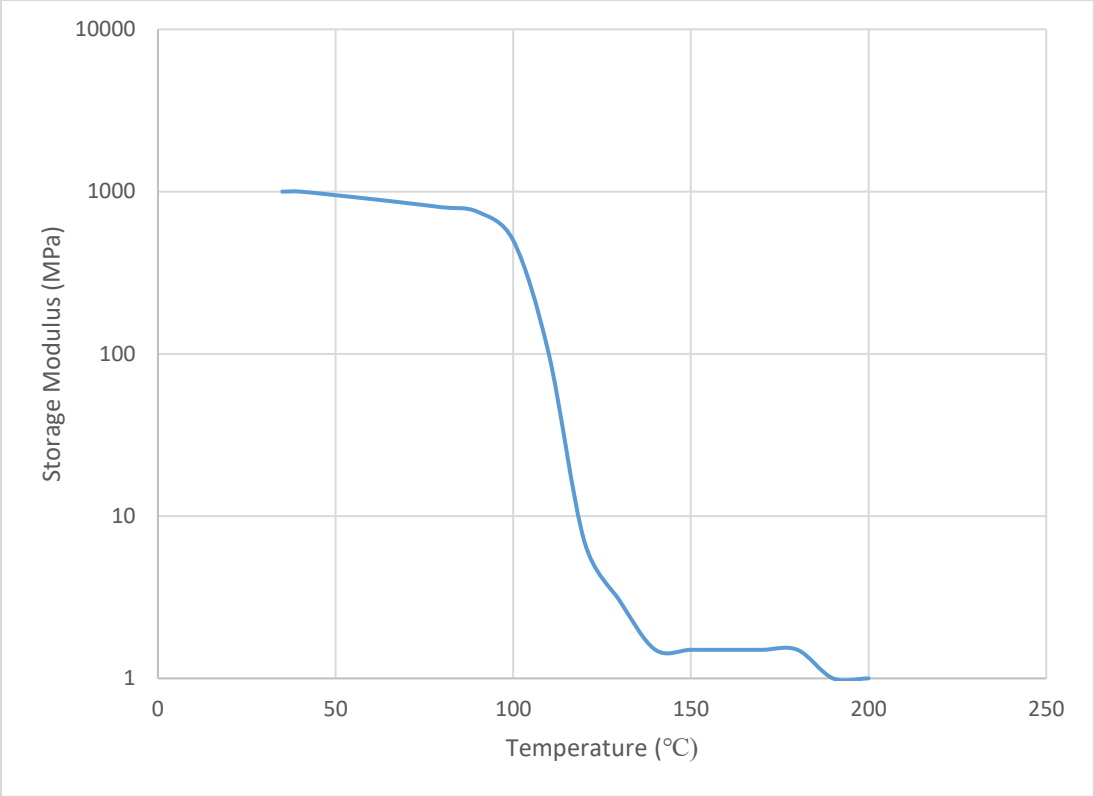

Figure 3-9. Storage modulus responses to temperature for pure ABS pellets [55].

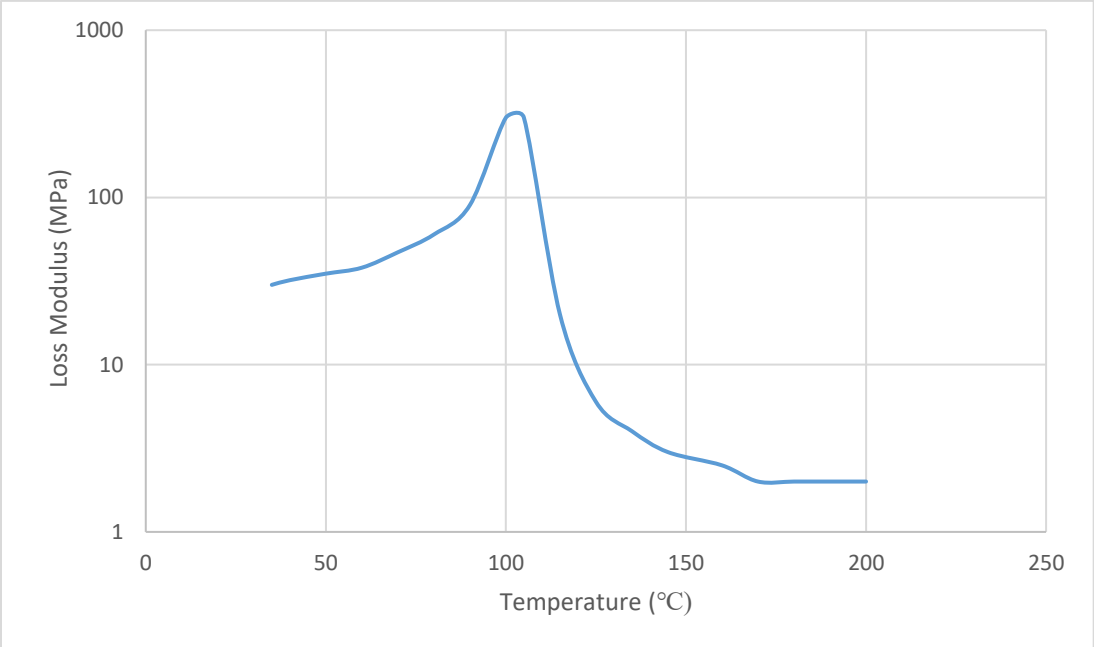

Figure 3-10. Loss modulus responses to temperature for pure ABS pellets [55].

The linear expansion values for ABS in this study were based on the results from a thermal dilatometer in [55]. Dilatometers are commonly used to measure the dimensional changes in metallic alloys, polymers, and organic matter under changing temperatures. The dilatometers work by increasing the temperature and recording the expansion or contraction in solid material [57]. The measured values and test parameters can then be used to determine the thermal expansion coefficient. The test specimen for both the storage modulus and thermal coefficient of expansion were made by FDM from Reference [55]. In addition, the work in Reference [55] shows the typical trend seen in ABS material for linear expansion measurements, but the actual coefficient of thermal expansion can significantly vary from 7.0 to 15.0 x 10^{-5}/°C [59]. The large differences in the coefficient of thermal expansion between ABS manufacturers show the importance of conducting tests to verify the material's properties. As an example of the importance of the coefficient of thermal expansion, it was also discussed in Reference [55] that it plays a prominent role in the amount of warpage seen at the end of the build. The greater the coefficient of thermal expansion, the more warpage is present in the final part. This relationship was also confirmed by [60-61].

Young's modulus is the measurement of a material's elasticity and measures the resistance to non-permanent deformation, essentially the inherent stiffness of a material [62]. The values for Young's modulus presented here are based on the results from [63]. The values in Reference [63] were determined using standard precision tensile testing.

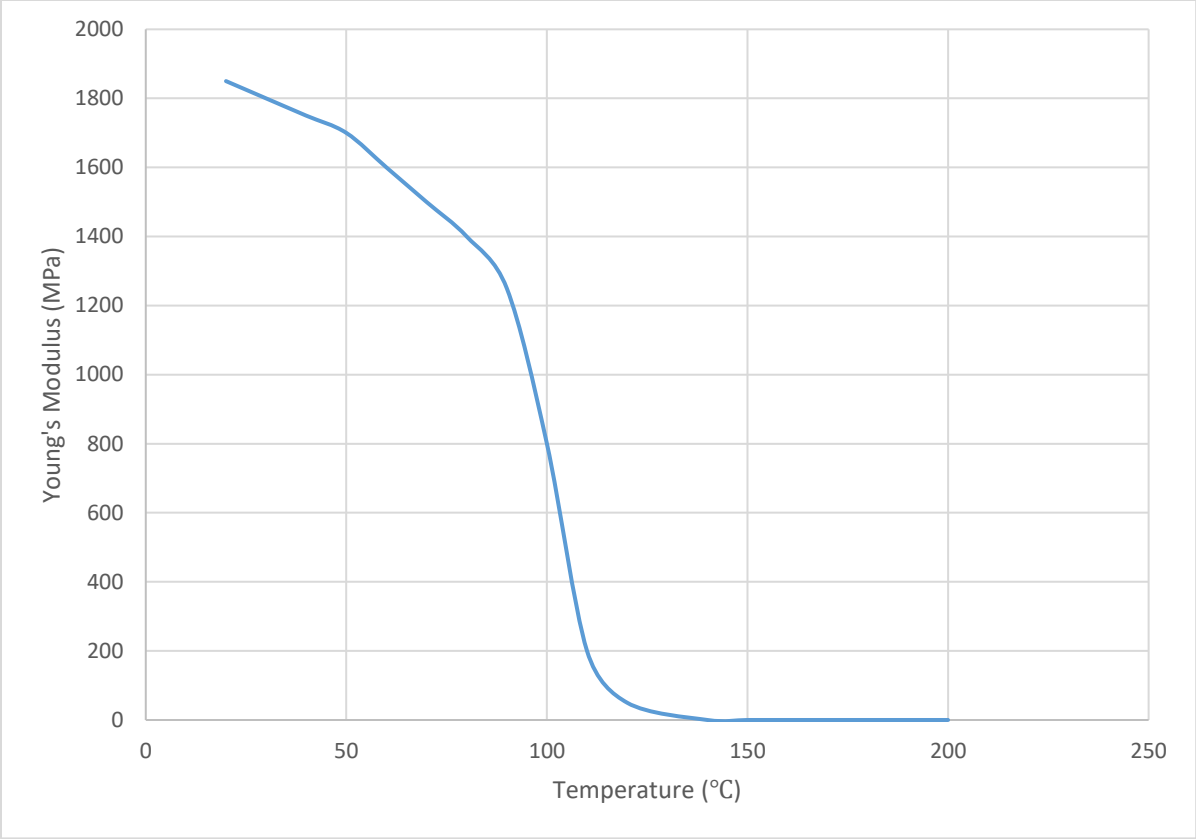

Figure 3-11. Young's modulus (MPa) response to increasing temperature (°C) [63].

Yield strength corresponds to the stress value when a material transitions from the elastic to the plastic region [62]. This is one of the most important properties for choosing the proper materials needed for structural applications. The values for ABS yield strength presented here are from [63]. The values in [63] were determined by using standard precision tensile testing over a temperature range, as shown in Figure 3-12.

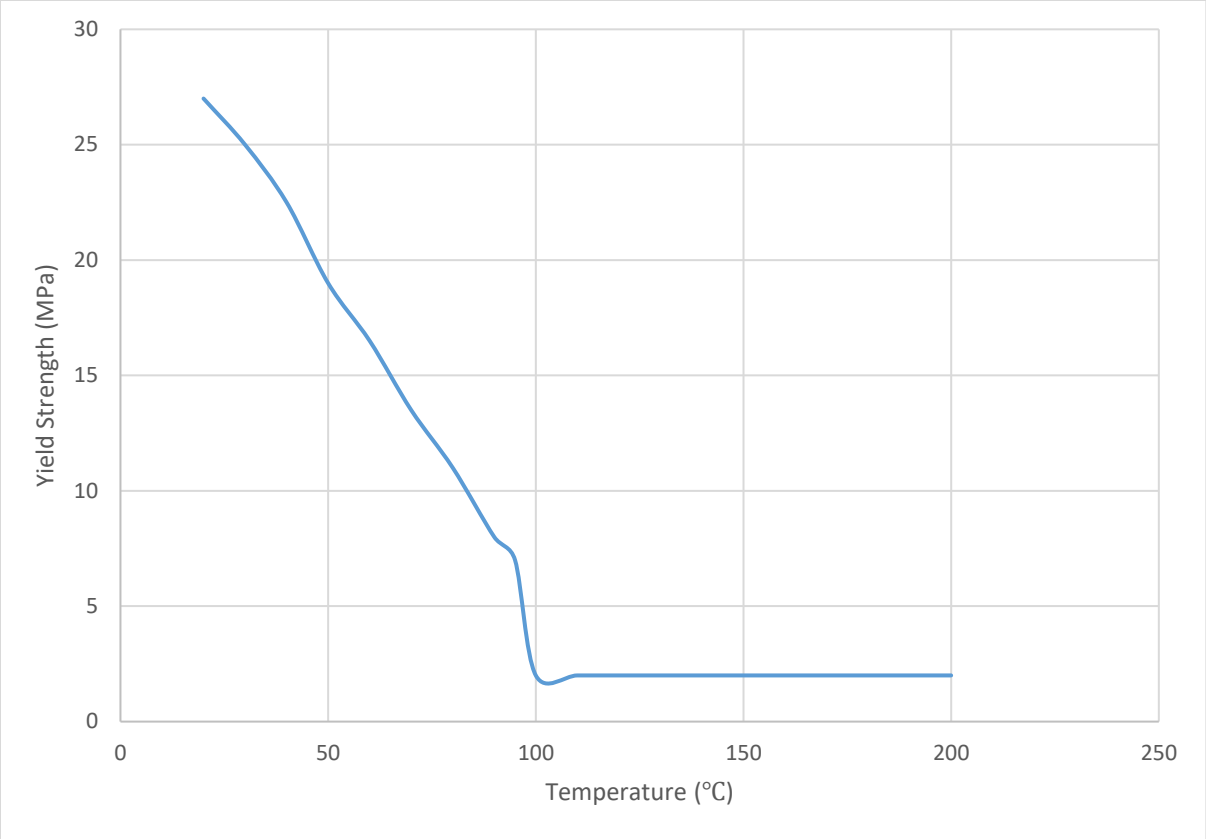

Figure 3-12. Yield strength (MPa) response to increasing temperature (℃) [63].

Ultimate tensile strength is defined as the maximum load that a material can withstand until fracture or failure begins. This is another common material property used for choosing the proper materials for structural applications. Tensile strength is tested through standard tensile tests, which in this case, the values from [64] were tested over an extensive temperature range, as shown in Figure 3-13.

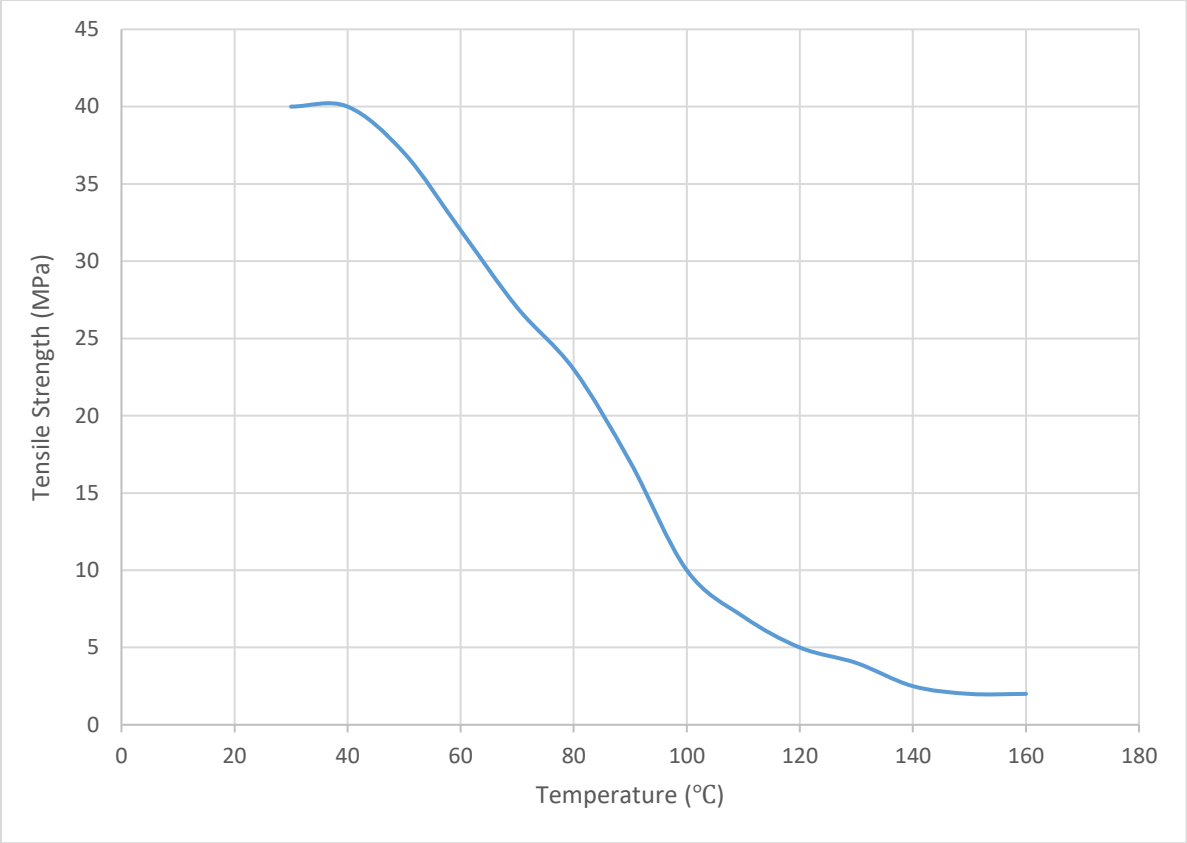

Figure 3-13. Tensile strength of ABS response to increasing temperature [64].

Thermal conductivity refers to the ability of a material to transfer heat by conduction. Thermal conductivity in polymers occurs by means of molecular agitation and the energy transferred by the free flow of electrons in the solid. Heat is transferred along the temperature gradient from hot to cold sources through conduction. This thermal energy transfer occurs until the material reaches thermal equilibrium [65]. Polymers, such as ABS, have a much lower thermal conductivity than metallic materials, making them useful as insulating materials. Lower thermal conductivity values reduce the amount of energy able to be transferred through conduction. This is an essential consideration for AM from a strict heat transfer perspective since the new layers should have minimal reheating effects on the previous layers.

Thermal conductivity is a function of temperature. Some materials show an increase in value as temperature increases, as seen with ABS in Figure 3-14. Often, for smaller temperature ranges, the value used for the thermal conductivity is an average of the values over the specific temperature range. However, the temperature-dependent values should be used for studies with a large temperature range and if a more accurate model is required.

Several testing methods can obtain thermal conductivity values, which fall under steady-state or transient methods. Guarded hot plate, heat flow metering, comparative-axial-heat-flow are examples of steady-state methods. Steady-state methods apply constant heat to the sample, where the heat transmitted through the sample can be determined, and the thermal conductivity can be calculated. Modified transient plane source, transient plane source, transient line source, and laser flash diffusivity are examples of transient testing methods. Transient testing methods use a heat source that cycles temperature. The thermal conductivity can be calculated using the time and feedback response after activating the heat source [66]. Either transient or steady-state methods can test polymers. One of the more popular testing methods for polymers is ASTM D5930 which specifies the transient line-source technique.

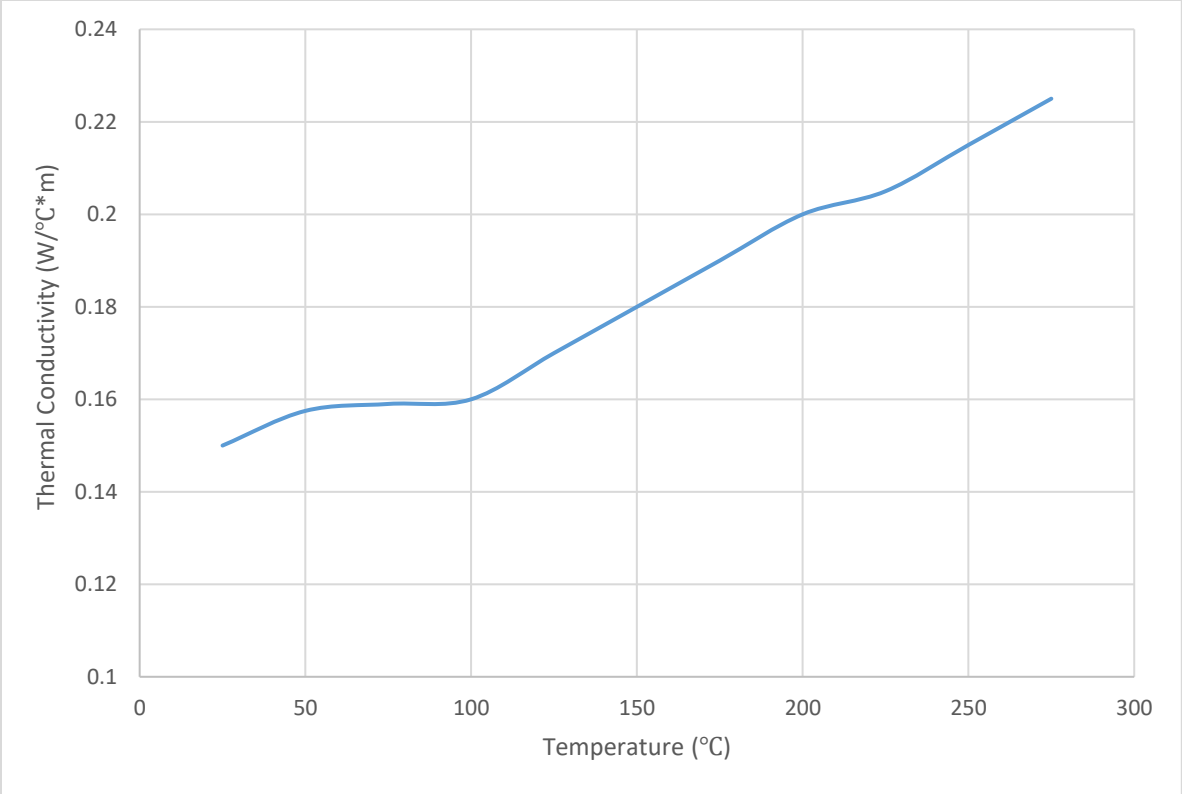

Figure 3-14. Thermal conductivity of ABS as a function of temperature [63].

Specific heat is defined as the amount of heat (energy) per unit mass to raise the temperature of a substance by one degree Celsius [65]. Specific heat is often used to determine the energy transfer to or from a system. In general, there are two kinds of specific heats of interest, specific heat at constant pressure and specific heat at constant volume. However, the specific heats of incompressible substances can be considered identical. Like thermal conductivity, the specific heat depends on temperature, but the value is often chosen from the average temperature of the substance. However, for studies with an extensive temperature range and if there are potential benefits of a more accurate model, the temperature-dependent values should be used.

The specific heat for ABS is shown in Figure 3-15, where it can be seen that the value increases with temperature. The values shown in Figure 3-15, were first presented in Reference [63], where ABS was tested to determine its heat transfer characteristics. Specific heat can be experimentally determined by differential scanning calorimeter (DSC) methods. DSC test methods heat the substance at a controlled rate and controlled environment. The temperature increases until the point of interest is reached. The difference in heat flow between the test material and the reference material due to energy changes is recorded [67]. ASTM E1269 is often used as the test reference for DSC testing methods. Per ASTM E1269, the difference in energy, mass, and the known specific heat from the reference is used to calculate the specific heat of the test material.

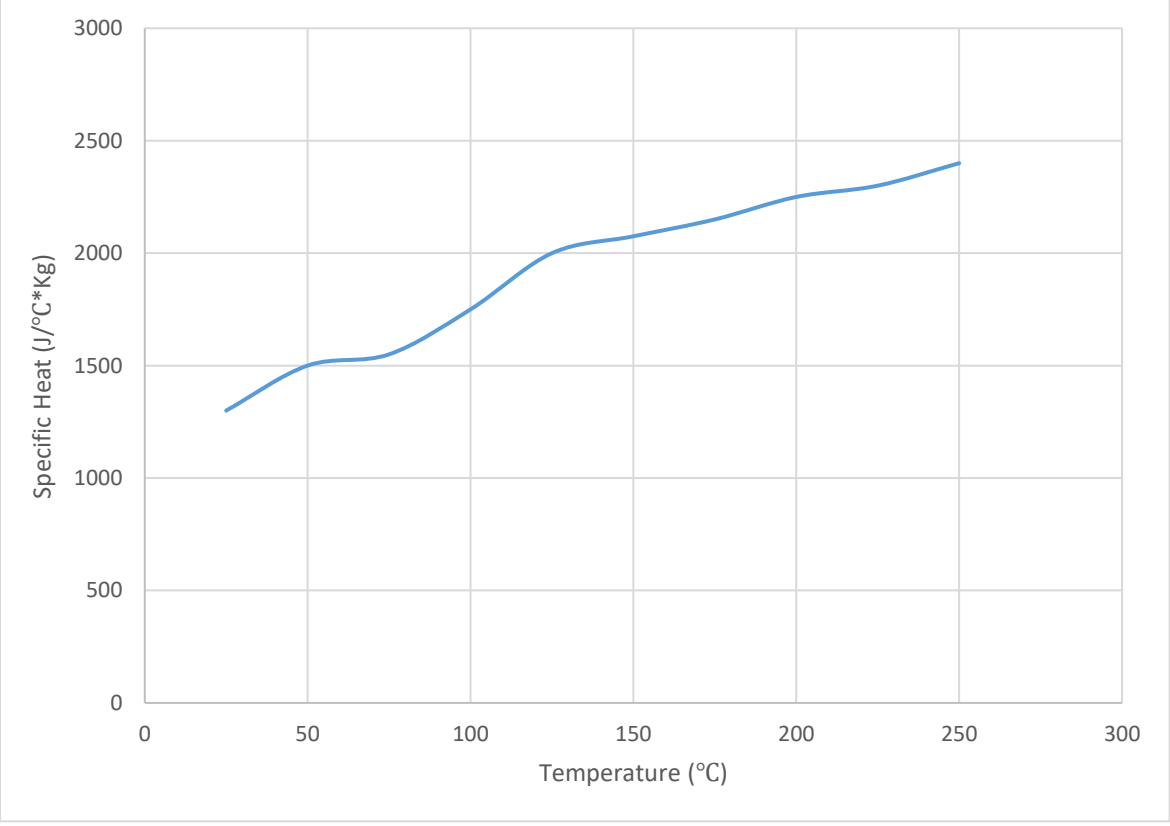

Figure 3-15. Specific heat capacity of ABS as a function of temperature [63].

Density is a temperature and pressure-dependent material property. The value of ABS density under atmospheric conditions can be seen in Figure 3-16. Density can play an important role in the material extrusion process. Since the extrusion process pushes material out through a heated nozzle, pressure can build up around the material, and the added heat input can significantly affect the bulk density of the material. These factors are essential to consider when determining the amount of pressure to apply to the material when extruding and deciding on the proper nozzle diameter [68]. While the change in density of the material may be more vital to consider for the extrusion process, density is also important for the build. Density affects the heat transfer performance of the material [65]. Therefore, it is important to include density's temperature and pressure effects in any simulations.

The density values shown in Figure 3-16 were determined by Pressure-Volume-Temperature (PVT) test methods in [69]. The piston die technique is a common way to test the PVT relationship. A material sample is inserted into the die, where the specimen can be pressurized. As the pressure and temperature are varied, a piston records the change in volume [70-71]. The PVT relationships can be made with the pressure, temperature, and volume recorded. Density can then be calculated for the material at all the temperatures and pressures recorded. Another standard method to determine density is by dilatometer. The density values from a dilatometer will result in density at different temperatures but at atmospheric pressure only. The density values shown in Figure 3-16 is assumed to be for a fully dense material (i.e., no porosity), since the model being created for this work is one bead thick there is no voids or large porosity that needs to be considered.

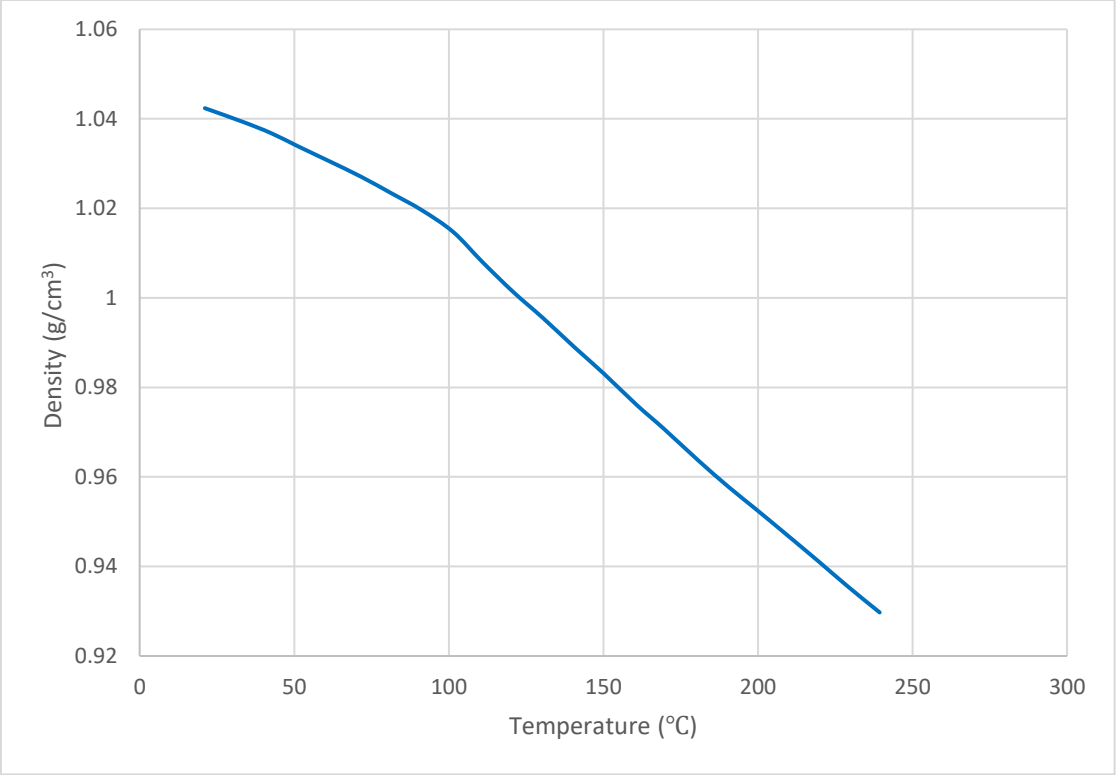

Figure 3-16. ABS density response to increasing temperature at atmospheric pressure [69].

Another property that can be gleaned from the temperature-property plots, mainly storage modulus, Young's modulus, and tensile strength is the glass transition temperature. The glass transition temperature for ABS is between 95-110℃ [30, 55, 63, 72-73]. Thermoplastics enter a rubbery state at a specific temperature where the material behaves like a viscous solid, called the glass transition temperature (T_g). Glass transition temperature is a term applied to materials where above this temperature the material no longer behaves solid, but behaves more rubbery with some flow characteristics. ABS still has structural integrity at temperatures just below the glass transition temperature. As the temperature increases and passes this point, the mechanical properties become almost nonexistent, and eventually, the material reaches a liquid state with low viscosity at higher temperatures well above T_g [44, 72]. The main difference between the melting point and the glass transition temperature is that the melting point occurs when the

ordered polymer chains fall into disorder (liquid state) and the viscosity is low enough that the material is able to flow easily. In contrast, the glass transition temperature marks the beginning of the polymer chain becoming disordered (rubbery region).

As mentioned previously, the glass transition temperature separates the typical viscoelastic region from the rubbery region for thermoplastic polymers. After the temperature increases past the rubbery region, a purely viscous region (liquid region) is present, which allows for easy flow of the material. This information is essential for modeling material extrusion as the temperature of the material transitions between these regions [72].

Since material extrusion is operated by heating the polymer to roughly its melting temperature, the material's rheology is essential to consider. ABS is a viscoelastic material, which means it exhibits both elastic and viscous properties when deformed. Whether the viscoelastic material exhibits viscous, elastic, or both properties depends on temperature and time. Generally, polymers will behave more elastically at lower temperatures or short timescales, and at higher temperatures or longer timescales, a polymer will have a more vicious behavior [72].

The viscosity is essential to consider, notably when the material temperature is above the glass transition temperature. Viscosity is a measurement of a material's ability to resist flow and deformation. Lower viscosity materials flow easier than higher viscosity materials. High viscosity materials polymers need to be at high temperatures or be subjected to an arbitrary load for long periods to initiate viscous flow. In contrast, the opposite is generally true for lower viscosity materials [65].

Viscosity can be determined through several different testing methods. However, no one test method can determine the viscosity of a material through all phases present in the ABS

material. DMA can determine the viscosity of solid materials. DMA, as discussed previously, calculates the storage and loss modulus. Viscosity can be calculated using the recorded test frequencies and the storage and loss modulus values [72, 74]. Since DMA requires a solid specimen to be held in a load frame, it becomes increasingly difficult to impossible to determine viscosity as the sample becomes increasingly viscous. Dynamic oscillatory shear tests can be used to find the elastic, viscous, and complex modulus of the material in the rubbery to a molten state (as defined in ASTM D4440). This was the method used in [74], and the results are shown in Figure 3-17. Dynamic oscillatory shear tests work by subjecting the sample to a sinusoidal deformation and measuring the material's response as a function of time [75]. Capillary rheology testing is helpful for material that is in a viscous state. This method pushes a viscous material through a capillary hole and measures the material's response [76]. While these methods can cover the entire range of phases present in the material, not all shear rates, timescales, and temperatures can be evaluated.

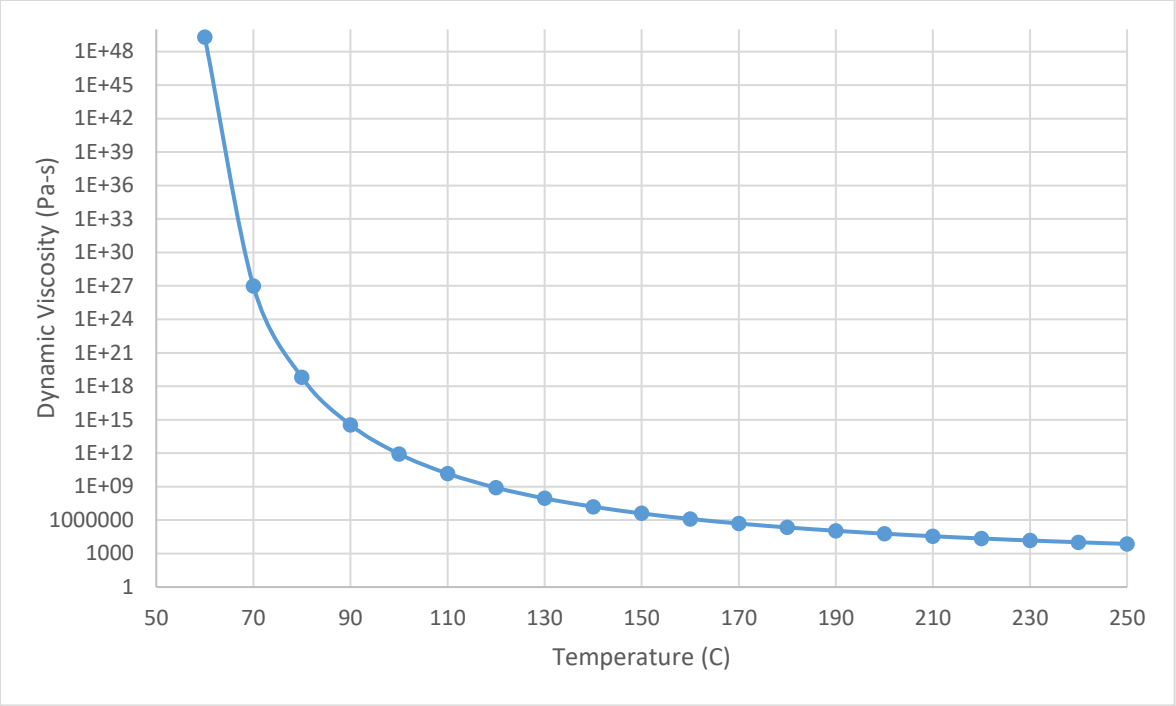

Figure 3-17. ABS zero shear viscosity response to various temperatures [77].

The viscoelastic material properties are both time and temperature dependent, therefore if a shear force is applied to a specimen for a long time at low temperature the resulting response could be the same as a specimen under the same shear force at a short time and higher temperature. Polymer time-temperature superposition (TTS) capitalizes on this phenomenon by equating the responses at short holds and high temperatures to long holds and low temperatures. This allows temperature and time-dependent material properties to be determined from available properties at a reference temperature [32, 72, 78]. The reference temperature is generally defined as the glass transition temperature, but it can be any temperature above the glass transition temperature where there are time and temperature responses are known. The resulting responses can be shifted to account for longer or shorter timescales or applied frequencies [78]. Therefore, if the viscosity was determined by DMA, dynamic oscillatory shear test, or capillary rheology

tests, the results could be shifted to account for any conditions. The William-Landel-Ferry (WLF) shift function (Equation 3-1) is commonly used to calculate the shifted response in polymers. The viscoelastic response is interpolated with temperature by considering the relaxation time of the material. Using the WLF method is essential when modeling the material extrusion process since relaxation time can be accounted for to ensure proper viscoelastic material response when modeling. For ABS the C_1 and C_2 constants are 4.47 and 105.14 from [74]. By using the WLF shift function, the viscosity at various temperatures and shear rates can be determined. The following plot, Figure 3-17, shows the zero-shear viscosity as an example.

$$\log(A(T)) = \frac{-C_1(T - T_0)}{C_2 + (T - T_0)} \qquad \text{Equation 3-1}$$

where

$A(T) =$ Shift function,

$C_1 \; and \; C_2 =$ Material dependent constants,

$T =$ Temperature,

$T_0 =$ Reference temperature (170°C).

In addition to the WLF shift function, a Prony series is also needed to properly capture the material relaxation. The relationship between the relaxation modulus and relaxation time shows that over longer periods of time stress can relax due to the viscous effects of the material. The relationship shown in Equation 3-2 was determined by dynamic oscillatory shear tests in [74]. The storage and loss modulus values were used to determine the relaxation modulus values needed for the Prony series parameters. The formulas to get those parameters are shown in Equations 3-3 to 3-5 [112]. Note that the parameters are found at a reference temperature above the glass transition temperature, in this case 170°C, the WLF shift function can then slide the relaxation responses to the desired temperatures making the results also temperature dependent.

$$G_i = (39323)\lambda_i^{0.321} \qquad \textit{Equation 3-2}$$

$$G'(\omega) = \sum_{i=1}^{N} \frac{G_i \omega^2 \lambda_i^2}{1 + \omega^2 \lambda_i^2} \qquad \textit{Equation 3-3}$$

$$G''(\omega) = \sum_{i=1}^{N} \frac{G_i \omega \lambda_i}{1 + \omega^2 \lambda_i^2} \qquad \textit{Equation 3-4}$$

$$g_i = \frac{G_i}{G(0)} \qquad \textit{Equation 3-5}$$

where

G_i = Relaxation modulus (Pa),

λ_i = Discrete relaxation time (s) for the reference temperature (170℃).

g_i = Shear relaxation modulus (Pa/Pa),

$G(0)$ = Elastic shear modulus (Pa),

$G'(\omega)$ = Storage modulus (Pa),

$G''(\omega)$ = Loss modulus (Pa),

ω = Frequency (Hz).

In this next section, which discusses related research, it is noted that all studies found in the literature in which material extrusion with ABS is simulated do not use thermally dependent material properties. The reason behind the change in value over an extended temperature range is for reduced computational time, and it significantly complicates the model [79-80]. However, as seen in the plots above, there are sufficient differences in material properties as temperature changes. The printing process relies on laying a bead down while the previous layer is still above the glass transition temperature, ensuring the proper bonding between the layers [55, 79]. Since this research aims to determine the deflection and slumping that occurs while printing due to heat retention, it is vital to have accurate material properties at various temperatures. Therefore, the

same argument for not using temperature transient properties can apply here, but temperature dependent properties are used in this work to improve the model accuracy.

The experimental build in [5] used ABS/glass fiber material. This combination has been found to reduce the final build's warpage compared to pure ABS material [13]. Pure ABS material can cause significant warpage in the larger parts due to significant residual stresses caused by the heat input and cooling of the layers [13]. However, due to the geometry of the build being a single wall thickness, it is not expected that the difference in material properties would significantly affect the results. A slight difference in thermal conductivity, heat capacity, and Young's modulus do not significantly affect the predicted warpage. However, it has been found that one of the most influencing factors for warpage is the coefficient of thermal expansion (CTE) [60]. Although pure ABS has a larger CTE than ABS/glass fiber material, but as mentioned previously, the CTE can significantly vary from 7.0 to 15.0 x 10^{-5}/°C [59]. Therefore, a lower value (9.5 x 10^{-5}/°C) of pure ABS was chosen for this model [81]. A sensitivity study to determine the effects of different CTE determined that increasing the CTE increased the warpage by the same factor [60]. Therefore, the warpage should be similar by using a CTE closer to the actual test material CTE. As described herein, there is no expectation that a model using these material properties should behave significantly different than the experimental model used in [5].

3.11 Common Build Failure Mechanisms for Material Extrusion

This section is dedicated to reporting research that helped shape the methods, models, and assumptions made in this work. To sufficiently design an experiment and simulation that will cause excess heat retention to drive failure, confirming the overall hypothesis of this project, it is essential to know what failure mechanisms are common to material extrusion. This allows for the isolation of heat retention on one failure mechanism. Different mechanisms that can cause

part failure are detailed here; these include part geometry, material, temperature, and process parameters. This is not an all-inclusive list of publications reviewed for this project; however, these topics were chosen to help illustrate common trends seen during literature reviews.

3.11.1 Elastic Buckling and Plastic Collapse

There has been much research into additive manufacturing, and due to its popularity, material extrusion is no exception. Material extrusion, as mentioned before, is used for a vast array of materials. Failure modes are not unique to only one type of material. Reference [8, 39, 82] details failure in material extrusion for cementitious material. Reference [82] breaks the failure modes into two categories: (1) plastic collapse and (2) elastic buckling. Plastic collapse occurs when the weight of the printed part applies a force equal to the current yield strength of the material. It begins to fail and deform in a way that causes a complete failure of the print bead geometry, as shown in Figure 3-18.

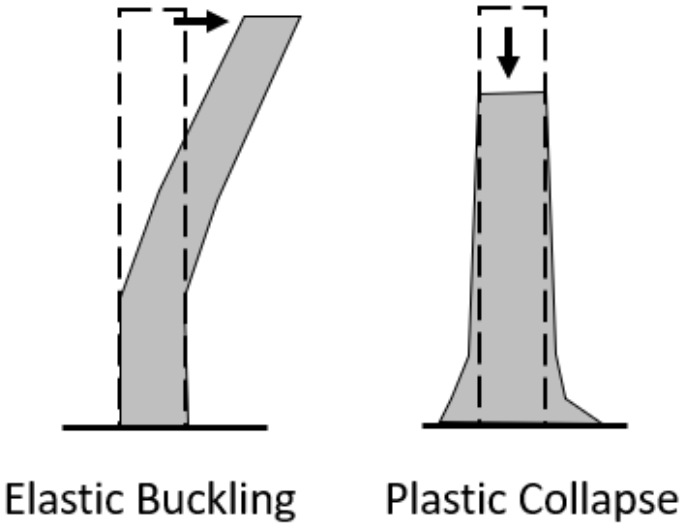

Figure 3-18. Elastic buckling and plastic collapse diagram.

In contrast, elastic buckling occurs when the geometric stability of the part is compromised. In other words, elastic buckling is typically seen during polymer material extrusion. This would be an example of a wall collapsing due to insufficient support material. Since the printing filament or pellets are designed to be used with material extruder equipment, there is little risk for the print bead to deform in such an extreme manner, as seen with plastic collapse failure modes. The risk of plastic collapse becomes more of a concern only when new materials are being tested and developed. Reference [82] identified a few parameters that control whether the part can experience elastic buckling. The parameters that were deemed the most important for cementitious material are solidifying material rate and printing velocity. These two parameters go hand-in-hand. Generally, the greater the print velocity, the less time the material has to harden before applying the next layer. This can cause print failures if the structure is not sufficiently supported [8, 82]. It was concluded in the research that a higher curing rate for cementitious material reduces the risk of part failure. This translates to polymer material extrusion by suggesting that elastic buckling part failure is more likely when the polymer stays at a higher temperature or in its semi-amorphous form when subsequent layers are added. This is also evident in work done in Reference [12].

3.11.2 Bridging Collapse

Other works have also tried to categorize the failures of material extrusion prints past elastic buckling. Reference [12] identifies many ways a material extrusion print can fail. One of the common failure mechanisms is bridging. Bridging occurs when a bead is laid across two buildups at a distance apart. Bridges are fixed at both ends, and the horizontal distance the bridge can span is based on material, material extruder, and environment. When a bridge spans too long for the material to support its weight, the bridge will slump and ultimately fail [12, 23]. This is

exacerbated by increased heat in the print chamber or retained in the printed layers. As the heat increases, the material strength is reduced, which shortens the allowable span length. This bridging collapse is also evident in cavity geometries. Typically, any design that utilizes an overhanging feature, which is self-supporting over a considerable span, is susceptible to failure by slumping and eventual collapse [23, 63].

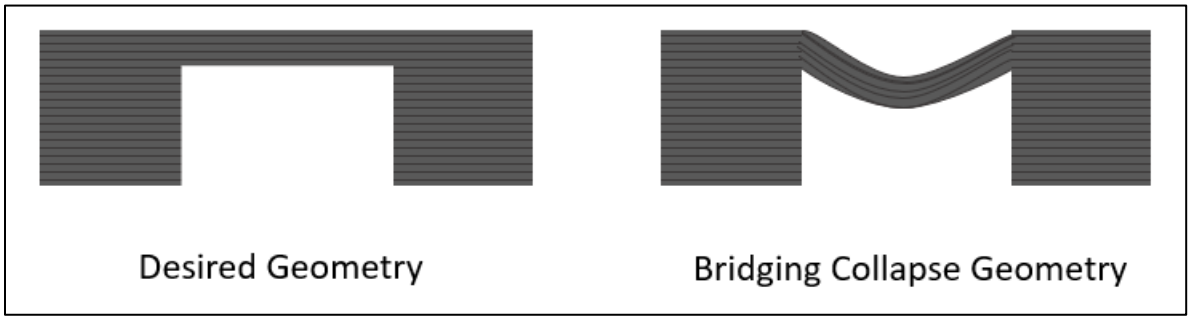

Figure 3-19. Example of a bridging collapse.

The bridging failure mechanism can be easily solved with support material, but support materials are costly and time-consuming for large prints. Therefore, it is ideal to know in advance if the bridge can successfully span the distance. The are several ways to improve the distance a bridge can span. One of the methods used for smaller printed parts is to allow the material to cure or solidify faster, giving the bridge a greater chance to withstand its weight. This can be done by directing cooler air towards the bead or by reducing the print chamber ambient temperature [20, 63].

3.11.3 Delamination

Delamination occurs when two connected layers separate from each other. This failure can occur in any size print. The layer temperature is the main cause of this type of failure [23].

When there is too much time between printed layers, the bottom layer has cooled to a temperature that does not facilitate proper bonding [12, 83]. The bottom layer is cool enough that it contracts and solidifies, but then a new or top layer is printed, the bottom layer is heated again and causes expansion of the bottom layer. The expansion and contraction of the bottom layer are dependent on the thermal expansion of the material. The expansion and contraction are not always detrimental to the print, but when the contraction causes high internal stresses, it can pull the print apart on its weakest orientation, Z-axis. This is also how part distortion, or curling, is created [12, 83].

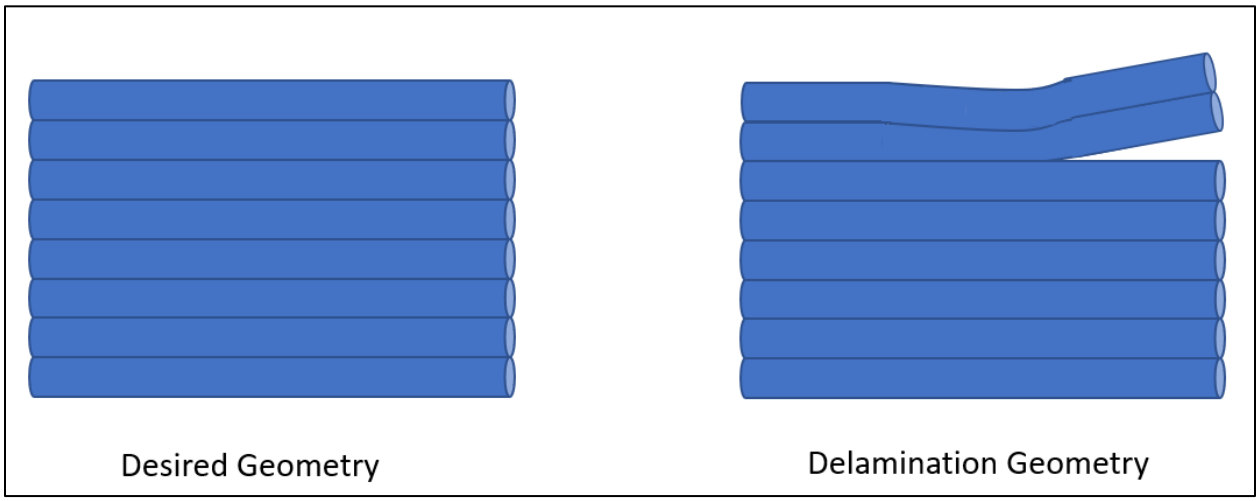

Figure 3-20. An example of printed part which failed by delamination.

It has been identified in [12] that this issue is more prevalent in larger prints, this means that there will be larger thermal gradients throughout the build. More than likely, the delamination will occur in the areas which see the most residual stress or are under greater thermal fatigue than the rest of the print. Geometry can also play a part in the delamination

mechanism, and deposits with a thin bead and low volume and high surface area are the most likely candidates to fail by delamination [84].

Delamination can also occur between the bare build plate and the first layer [23, 83]. This type of delamination occurs when the thermal expansion is significantly different between the part and the print base plate. If the build plate, or substrate, is made of a material that has a larger thermal conductivity than the print material, and the temperature of the build plate is cold enough, then the printed bead will be unable to adhere to the build plate and warp [43]. This can be overcome by heating the build plate. However, if the temperature of the build plate drops rapidly or significantly enough, then the thermal contraction and expansion of the two dissimilar materials is enough to lose contact.

Polymers go through a glass transition temperature. This temperature is identified as the moment a polymer gains rigidity and no longer is an amorphous and viscous solid that can be easily extruded and shaped. It is noted in Reference [83] that the glass transition temperature should be used by designers as a print cutoff line. If the temperature of the top layer, right before the next layer is added, goes below the glass transition temperature, then the part should be scrapped due to the high probability the part will suffer from delamination or more extreme warping. This cutoff line is more applicable to large prints that are difficult to control ambient temperature, slow print velocity printers, and the geometries mentioned previously.

3.11.4 Sagging/Slumping for Overhanging Features

Overhanging features can fail in a similar manner to bridging features. These features generally overhang at an angle. Reference [12] notes that best practices would dictate not to design a part with overhanging features that protrude out at an angle less the 45 degrees from the X-Y plane. Anything less than 45 degrees would need support material or redesign. The reason

overhanging features have this cut-off is due to the small amount of contact between the layers. The lower the overhanging angle, the less contact area between them, which reduces the strength of the feature. Any unsupported features in this realm are highly susceptible to falling off, sagging, or cause print failure. This type of failure is exacerbated by the larger prints, larger bead sizes, and higher temperature print atmospheres [5, 7, 12].

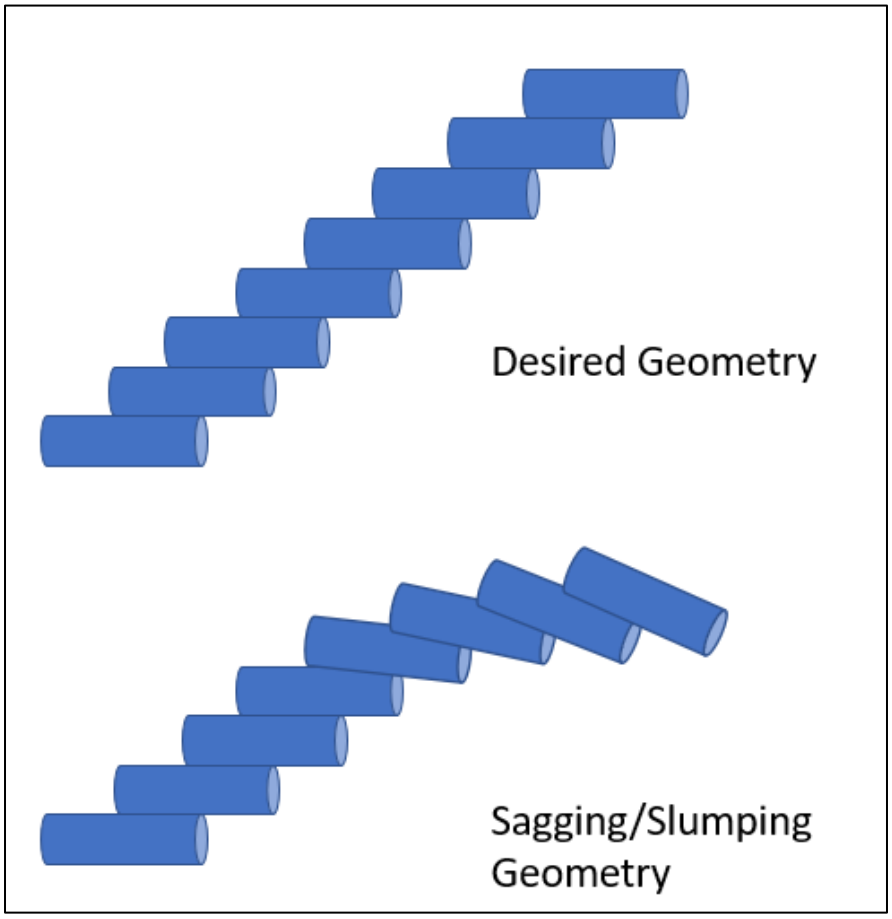

Figure 3-21. Example of an AM structure sagging.

In addition to the cases mentioned above, thermal retention is a primary cause of this type of failure. When a bead retains enough heat and the next layer is added, the previous bead is still prone to slumping or collapse [3, 23]. As more beads are added, the weight increases enough to

cause this failure. Several studies have looked at the process to optimize and find solutions to this process. Reference [12] and [43] performed studies to determine the greatest angle that can be created without the need for self-supporting features. One study, Reference [12], led to the conclusion that if the print stayed within the process-specific minimum angles and the overhanging features could be built in the Z-direction, then there was no need for support material. Reference [12] further tested the overhanging feature angle by designing a test to reduce the angle until it was parallel with the build plate. The tests showed that only on one occasion was the print able to make it past the 45 degrees recommended max angle. However, most tests were unable to make it past 40 degrees.

3.12 Big Area Additive Manufacturing

Big area additive manufacturing (BAAM) utilizes the same techniques as other material extruders, however, is it on a much larger scale.

The typical material extrusion printer has a print volume ranging from 11 X 7 X 6 inches to 36 X 34 X 36 inches (X, Y, Z), while BAAM printers offer sizes such as 20 X 8 X 6 feet (X, Y, Z) [7, 11, 12, 85]. Figure 3-22 shows a graphic comparing the overall print volume size for BAAM and common material extrusion AM equipment. BAAM, or in more general terms, Large Area Additive Manufacturing (LAAM), offers the same benefits as its smaller versions [86]. Elimination of hard tooling and creating increasingly complex parts are all benefits carried over into this new realm of material extrusion.

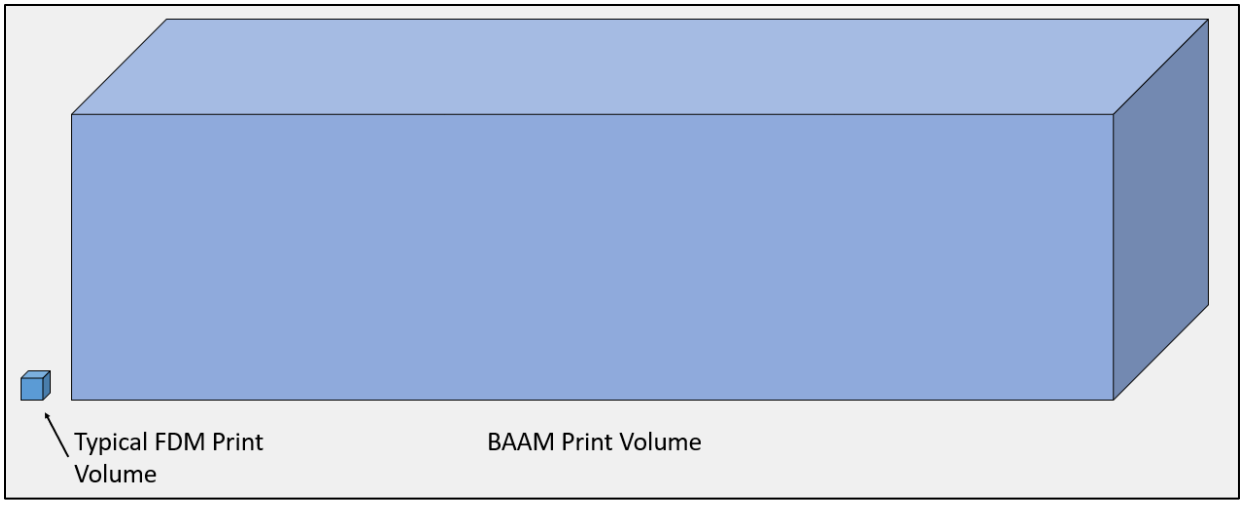

Figure 3-22. Print volume comparison between BAAM and common FDM equipment [21].

Since the printing scale is larger than the typical AM size, process parameters need to be optimized to produce faster and more cost-effective parts. Typically, these printers will utilize pellets since it offers greater speed than using filaments, and the pellet hopper can be refilled while printing [11, 87]. It is also less expensive than thin filament options. Most polymers printed by LAAM are reinforced with some fiber or other strengthening and stiffening agent to improve part quality and printability [7, 11, 85-87].

Early design LAAM printers will create an oval-shaped bead depending on the process, material, and print parameters (i.e., speed, temperature, standoff distance, flow rate, extruder nozzle shape, and viscosity) [11, 55, 83]. These oval shapes would create voids when additional layers were laid down, where the void size is dependent on printing parameters. As materials and AM technology improved, better bead layers can be created, which allow for minimal voids and can make beads better suited for layered building [11, 44, 83]. Support material also needed optimization. In smaller prints adding support material would increase the print time and cost to finish the part [12, 50]. With this much larger printing area, the support material has an even

more significant effect on the time and cost of the printed parts. The time it takes for support material to be created can affect the temperature of structural material, detrimentally affecting the piece's strength. It also can add residual stresses into the part that can lead to part failures [12, 50].

Additionally, the added cost of including a dual extruder system for the support material and the material itself significantly increases the overall cost to build. In most LAAM/BAAM builds, the support material is not used unless it is essential. Unfortunately, this limits what designers can create on this large scale [12]. Simulations can be used to determine where support material might be needed and determine the layer temperatures to ensure the best outcome. The role simulations play in additive manufacturing is addressed in the following section.

Over the years, some impressive LAAM/BAAM builds have been created. One of the most notable was making a classic Shelby Cobra vehicle [13, 21]. This rapid vehicle powertrain development explored the challenges faced when creating a printed prototype mule. Once the vehicle was completed, the total weight was 690 lbs., and the total print time was roughly 24 hours. This feat was only accomplished at that time due to the BAAM system. The polymer-extruded nozzle fitted to a multi-axis servo system was able to deposit on average 20 lbs./hr. Each bead was extruded out of a 0.2-inch diameter nozzle, which only resulted in about 0.030-inch surface variation [13]. As mentioned previously, these types of large AM systems utilize single-screw extruders to heat up the pellets to their molten state. This is one of the main reasons the print only took about 24 hours. This could have taken about 500 to 1,000 times longer with more common AM processes [13].

It was determined for this study, [13], that carbon fiber reinforced ABS was needed for proper manufacturing. Using pure ABS material can cause significant warpage in the larger parts

due to significant residual stresses caused by the heat input and cooling of the layers. At the time of the study, adding carbon fiber to ABS was a relatively new practice. However, it turns out that higher amounts of carbon fiber (greater than 15%) led to significant reductions in warping.

Warping of the printed frame was one of the biggest concerns for the build [13]. Even though the material chosen was adequate to resist the residual stresses, the printed design was robust and not designed in a way to reduce cost or weight. This robust design would have retained much heat and could have caused elastic buckling of parts or slumping of overhanging features. The designers utilized support features to build up areas that could not have support themselves during the print. These supports, added time, material/cost and could have been an additional site of failure. The print failing due to support structures is possible since they also are exposed to the same thermal gradients and are often designed to use the least amount of material to build in the least amount of time. In this case, the material is printed along the length of the frame to maximize the strength of the part. Since the printing path dictates how the material will be deposited, support material will be needed if any areas do not allow for a slow build-up of overhanging features. Therefore, the support material is needed for this design.

As mentioned, the frame was built with the bead running along its longest dimension [13]. This print orientation provides the highest strength and stiffness. Layered processes all tend to have anisotropic mechanical properties [11]. The material, and in this case the carbon fiber, tends to align itself with the tool path [81]. The weakest part of material extrusion AM is typically the strength between the layers. This is discussed further in the next section.

3.12.1 Structure and Mechanical Behavior of Material Extrusion AM Materials

The earliest rapid prototyping equipment made parts that were only suitable for a 3D visual representation of desired parts. There was very little structural integrity at that point. After

years of improvements in both the AM materials and printing techniques and equipment, the manufactured parts can be used in everyday life applications. Even though there has been much improvement over the years, BAAM and FDM printed parts strength is very dependent on the material orientation. It is generally known that the strength between the beads is weaker than the strength of the bead longitudinally [11]. This is due to a reduction in volume at the fusion areas.

The beads that come out of the extruder are deposited with an oval shape. BAAM applications have a typical width of 0.33-inches and a thickness of 0.15-inches if using a 0.3-inch diameter nozzle [11, 83]. The oval shape's specifics depend on the material and process (i.e., extrusion temperature, standoff distance, flow rate, viscosity, and head speed) [11, 83]. These oval shapes create triangular voids between neighboring beads [11]. These voids reduce the contact area between adjacent beads. Reference [11] estimates there is roughly 30-50% contact area between neighboring beads and 75% contact area with the layer beneath. This reduction in contact area can severely degrade the expected strength of the part [11]. The total porosity in a LAAM deposit will rely heavily on the printing parameters and geometry.

In addition to the oval bead triangular voids, it is also possible to have voids caused by improper processing of the material. The voids are most likely caused by air trapped in the material as it processes or due to impurities in the polymer, which outgas the volatile components [11]. Fiber-reinforced polymers also tend to have a higher concentration of internal porosity when used in the BAAM systems [11]. The fibers usually are cut into small strands, and it is believed that these strands can alter the flow field during extrusion, which can create nucleation sites for bubble formation. One of the main differences between fiber-reinforced polymers for FDM and BAAM is in the way the fibers orient during the extrusion process. In FDM, the fibers orient along the extruded tool path, whereas only the outermost portion of the

bead will have oriented fibers with the BAAM system. The internal fibers will remain randomly oriented [11].

In material extrusion AM the direction of the lowest strength is often considered to be across the successive layers (Z-axis) [11, 88]. The lower strength is due to a more significant temperature difference between the layers, making it less likely to have a stronger bond than the other layers. BAAM, however, seems to be weaker in between the interface of neighboring beads (along the Y-axis). This is due to the greater contact area between the Z-axis beads. The manner of deposition also can play a role in determining the weakest orientation. If the deposition is controlled to allow for warmer material bonding in a certain direction, it is likely that orientation will have a stronger bond. It has also been shown that a 45/-45-degree crosshatch pattern will significantly improve the X and Y-axis inter-bead strength and will consistently show that the Z-axis is then the weakest orientation [11, 16, 88]. Figure 3-23 and Figure 3-24 show mechanical properties of a printed test specimen, tested in X, Y, and Z orientations.

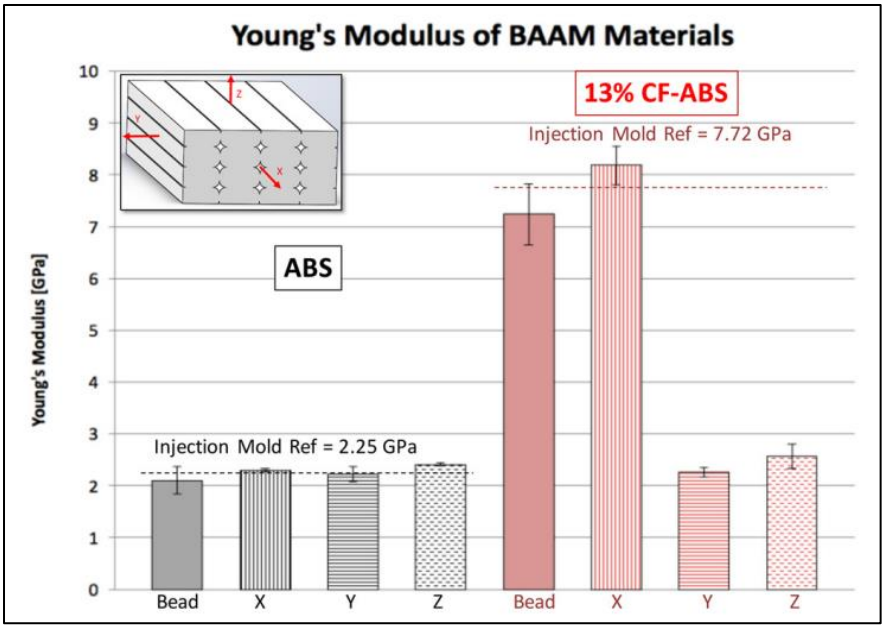

Figure 3-23. Young's modulus of ABS and 13 per cent CF-ABS for a BAAM-deposited bead and each primary load direction [11].

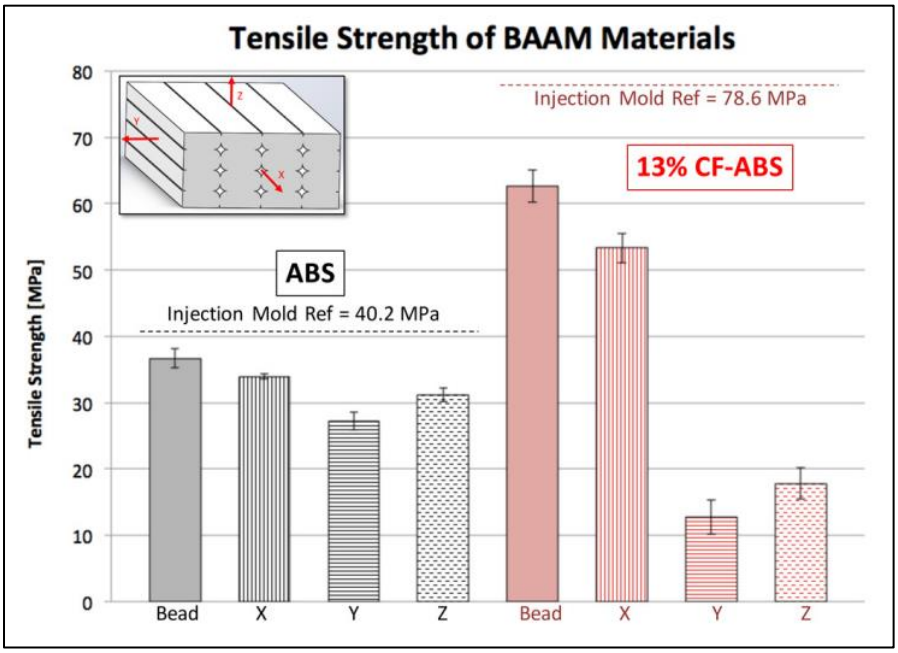

Figure 3-24. Tensile strength of ABS and 13 per cent CF-ABS for a BAAM-deposited bead and each primary load direction [11].

3.13 Material Extrusion AM - Finite Element Analysis

Numerical simulations for material extrusion fall into two categories: (1) mesh-free methods and (2) mesh-based methods. Finite volume and lattice Boltzmann method are considered mesh-free methods [80]. These methods are generally not used in solid structure numerical studies. The mesh-free methods are more commonly seen in fluid dynamic studies. Mesh-based methods, i.e., finite element method (FEM), are the most popular choice for numerical analysis. FEM utilizes the ability to reduce the problem to a limited number of unknown variables discretizing the domain. Finite element analysis (FEA) is a technique that finds approximate solutions to partial differential equations [80]. The solutions of these partial differential equations are based on dependent variables, which are expanded into linear combinations of polynomial functions, which are defined over elements. Most FEM software can customize the mesh to allow for each finite element to better represent the entire model as a whole. FEM also has become more powerful over the years, allowing users to solve more complex scenarios [80]. Newer software has also given users the ability to complete a parametric optimization study, which has become more popular with AM design processes.

Historically, most AM parts were not vetted by FEM. Optimization was found by trial and error [80]. As AM parts became more complicated and exceeding large, the trial-and-error process was becoming too time-consuming and expensive. Now, the FEA of AM parts has been gaining traction and is being used for entire parts and critical features. Certain FEM software packages, such as ANSYS and ABAQUS, offer a suite of AM add-ons so that users have built-in AM material databases, build parameters, and environmental considerations available for a quick analysis. Those add-ons are generally used for only metallic materials and are limited in how the part and print can be customized. Since using FEM for AM is relatively new, researchers are still

working out which methods offer the most realistic results that can effectively couple thermodynamic history with mechanical structure stability [80]. It should be noted that this can also be a time-consuming task, and most simulations of builds are very complex and require a lot of processing power to run. The run time and processing power are two of the main reasons simulations are not used. There are different methods for predicting the thermal and structural characteristics of material extruded parts. These methods often create simplified elements to get a rough idea of where problems may arise. The simplified models may incorporate constant material properties, simplified geometries, and the incomplete thermal history created by the part. All these simplifications significantly reduce the run time and processing requirements of a model. However, the simplifications also degrade the accuracy of the simulation. Therefore, it is essential to know the effects of the changes on the results when simplifying a model.

For the purposes of this section, FEA can be classified by what type of analysis is studied. Thermal analysis, mechanical analysis, and thermo-mechanical analysis are the three most common evaluations for AM parts. The mechanical analysis looks at how the completed part will function in service. Thermal analysis typically looks at how the part is created to glean information about the manufacturability of the part and temperature distribution during the process. The thermo-mechanical analysis looks at the entire history of the part, from the heat retention in the printing process to the residual stresses created during manufacturing to finally how the part will function in service. The thermo-mechanical analysis gives a complete picture of the part's life. However, this is also the most complicated and time-consuming analysis.

3.13.1 FEM - Structural/Mechanical Analysis

Typical uses for FEM structural or mechanical analysis are to simulate how different process parameters will affect the mechanical characteristics of an AM design. These

characteristics include uniform elongation, tensile strength, fracture toughness, and others. The analysis combines these characteristics to estimate the structural performance for parts made by FDM. All FEM analyses provide a best estimate prediction of what is happening in a printed part. Assumptions need to be made, and it is impossible to apply exact real conditions in a simulation. However, as FEA programs improve, the accuracy of the simulations is also improved. This section reviews some notable FEA studies that are applicable to the topic research.

Reference [89] completed tests on four specimens, where the raster angles were varied. The results were compared to classical Lamination Theory and Tsai-Wu failure criterion. Where lamination theory is used to establish a computational method for predicting stress and strains in fiber-reinforced laminated composite structures. Tsai-Wu criterion is used to improve the computational method used for isotropic material properties, as the material properties in each orientation are considered [89]. The failure load values, and numerical analysis showed good agreement between the predicted values and experimental results. However, the model had to make several assumptions about the material, and there was no information about the thermal history to know if the bonding of material played a more important role in the estimated failure.

Reference [90] detailed how modeling test specimens can be used to aid in predicting mechanical properties of different print parameters. The FEA model was able to accurately predict the tested results for elastic modulus. However, the research reported suboptimal results for comparison with tested values for the Poisson's ratio. The reported values differed by roughly 20%. This approach was recommended as an early attempt to understand how the material and structure would behave before doing any time-consuming experimentation.

Similar to [89], Reference [84] used an ABAQUS to model an ABS FDM specimen for tensile testing. The FEA model was created to closely resemble an actual printed part by creating a textured internal and external surface to match raster printing angles (0 degrees, 0/90 degrees, and 90 degrees), as shown in Figure 3-25. Three different layer thicknesses (0.254mm, 0.178mm, and 0.330mm) were also tested. The elastoplastic behavior simulation was experimentally validated by comparing the qualitative responses in the experiment. The results of the study showed that elongation, tensile strength, yield stress, and strain are dependent on layer thickness. It was shown that the greater layer thickness had higher tensile strength due to the greater intra-layer bond area. However, the thinner layers showed higher elongation than the greater layer thickness specimen. It was also confirmed in both the simulation and testing that the fibers laid longitudinally (length of the specimen) would fracture through the fibers. In comparison, the transverse fiber specimen would fracture through the welded region.

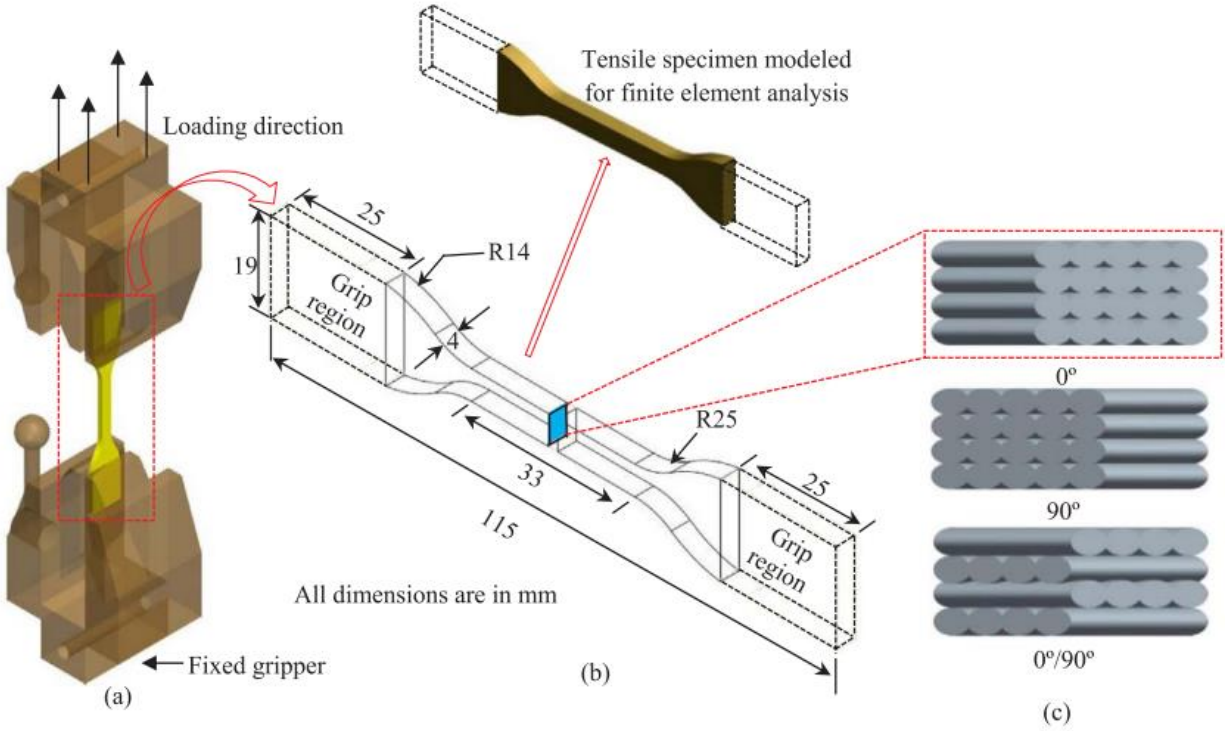

Figure 3-25. (a) Schematic of gripper arrangement, (b) tensile specimen as per ASTM D638 standard, (c) schematic illustration of different raster angles [84].

In Reference [91], the effect of layer thickness and infill percentage on the mechanical characteristics of FDM was studied. A porous model was created in ABAQUS to simulate the different voids created by the changing layer thickness. The model was able to accurately predict the bulk material mechanical characteristics as verified by experimental testing. However, the model was unable to predict the local non-uniform strains which were observed experimentally. This was postulated to be due to the residual stresses from the manufacturing process that were not accounted for in the model.

These and other mechanical and structural simulations, References [90, 92-93] used assumptions to simplify their model. One of the significant assumptions made was that FDM parts had isotropic properties, despite numerous studies proving otherwise. This assumption

greatly reduced the complexity of the FE model. Another source of stress unaccounted for is residual stress. This additional stress is produced during the printing process, where it might not cause any warping in the printed part but may greatly increase or reduce the predicted mechanical characteristics of the part in comparison to the FEM model results. Comparing to experimental results may prove to show more significant differences or, worse, validate an incorrect model if residual stress is not considered. Predicting residual stresses can be accomplished by obtaining a thermal history and completing a thermo-mechanical analysis to account for the residual stresses.

3.13.2 FEM - Thermal and Thermo-Mechanical Analysis

Improvements in numerical methods and increased computational speed have given rise to more accurate predictions of thermal histories for AM processes. Typical FEM software used for this type of analysis is commercially available ANSYS and ABAQUS. During an FDM process, the temperature gradients change and move along with the print nozzle. This causes a significantly uneven distribution of temperature. Due to the heat retention in printed parts, there is potential for deformation and thermal borne defects [3, 27, 50]. Convection, conduction, and radiation all are significant modes of heat transfer. One or more of the modes can be of more significance depending on the material and environment [65]. Process parameters and material selection are important factors that reduce the temperature gradients, and in turn reduce the development of thermal stresses. Thermal and thermal-mechanical analyses are combined in this section since most thermal analyses are aimed at determining the residual stresses in parts.

In order to get a more accurate thermal history of a part being printed by the FDM process, element activation is often used. Element activation or element birth and death is a method that turns on or off elements at specific time intervals [52, 79, 94]. This is how the

thermal history is more accurately replicated with an FDM process. As time progresses, an element is activated ("element birth"), which is assigned a temperature. The temperature is also assigned a time range for activation. The process and outcome of the element birth and death can be seen in Figure 7 from [79]. Controlling the temperature-time range simulates the nozzle moving on from that element onto the next element, just like a print nozzle depositing a bead over a specific area. Element death refers to the case when the stiffness and conductivity of an element is reduced, 1E-6 Pa and 1E-6 $Wm^{-1}K^{-1}$, to essentially non-existent, and having extremely little influence on the surrounding elements, Reference [95].

Reference [50] studied the thermal history of an FDM part and applied the history to determine residual stress distributions. Reference [50] also utilized the element birth and death functions to apply a likely tool path. It was determined that the tool path played a large role in the locations where the most significant heat retention was focused. The tool path turning points created larger thermal gradients and stress accumulation marks. The study also showed that deformation trends followed the trends seen from the heat dispersion along the printed surface. Longer raster paths tended to create warpage along the length of the part, while shorter raster lengths tended to create warpage along the width of the parts. However, the material properties and boundary conditions for this work were more theoretical and lacked actual validation comparison with experimental data. Reference [96] also used element birth and death for a 3-D transient thermal non-linear FE model. The model simulated an FDM process using ANSYS parametric design. The study found that more significant heat gradients are found near the part edges and that the temperature field distribution is in the form an ellipse across the face of the part.

Reference [95] experimentally tested the filament temperature at deposition by using an infrared sensor. A simulation (ANSYS) was then used to predict thermal stresses and the thermal history for the FDM process. The model was made as a thin-walled box and utilized the element birth and death functions in ANSYS. The temperature history was saved and applied to a structural FE analysis where the thermal history could be applied to determine the thermal induced stresses. The study also identified the effects of substrate temperature, nozzle temperature, layer thickness, and deposition speed. Both the simulation and experiment showed that the time it took for the material to go from the extruded temperature to the glass transition temperature was greatest when the nozzle temperature was highest, layer thickness was greatest, low printing temperature, and high substrate temperature. While the model showed a good correlation with the experiment, it assumed some material properties were constant during the cooling process. This could have introduced errors that would have produced higher thermal induced stresses or caused further deviations from the experimental results.

Reference [97] studied the effects of radiation, convection, and conduction within the model. It was determined that the convection and conduction were the most influential on the thermal profiles of the model. Air pockets were also evaluated in regards to how they can affect the thermal profile. It was determined that the air pockets created by the ellipse-shaped bead have a negligible effect on the thermal profile. This confirms that using rectangular cross-sections to represent each layer can sufficiently predict thermal profiles.

References [50, 98] used an FEA model to determine part distortions after the FDM process. Like the other studies, element activation was used to simulate the manufacturing process. This parametric study looked at three factors and three levels to evaluate the effect deposition has on the residual stresses and part distortion. The three examined factors were road

(bead) width, layer height, and raster speed. Three levels for each of the factors were tested, low, medium, and high. The experiment and model were designed around creating a thin plate to create residual stresses easily. The results showed that scan speed had the most significant effect on the part distortion. The layer thickness was found to have the second most important effect, whereas the bead width had almost no effect. However, the bead width and thickness have a considerable impact on the residual stress. The simulation and experimentation showed similar trends, but there was no quantitative correlation between the experimental results and model results. This could be due to the material properties being inadequately modeled or environmental conditions that were not appropriately captured.

Part distortion was also studied in [87]. This study used Thermo-Mechanical Analysis (TMA) and Dynamic Mechanical Analysis (DMA) to determine the thermal expansion coefficients and temperature-dependent stiffness, respectively, for an ABS reinforced carbon fiber (20% wt.). This study considered the fiber orientations to use in comparison with its FE analysis. A thin wall was printed using BAAM processes with longer dwell times for the purpose of inciting warpage. The wall consisted of 100 layers which had a layer thickness of 3.81 mm. An IR camera was used to determine the experimental temperatures, while the warpage was determined by using a linear variable differential transformer (LVDT) to measure the deflection. Comparisons were made between the experimental study and the FEA model of the same part. Most of the material properties were considered temperature-dependent, i.e., Young's modulus, conductivity, specific heat, and tensile and compressive strength. The thermal analysis was used to determine the temperature field, then used in a thermo-mechanical study. The thermal model considered radiation, convection, and conduction. The results from the experiment and simulation showed similar trends in terms of the warpage and were in good agreement

quantitatively. It is unclear if the model took into account other temperature-dependent material properties, such as density. Including the temperature-dependent properties could have improved the match between the simulations to experimental results.

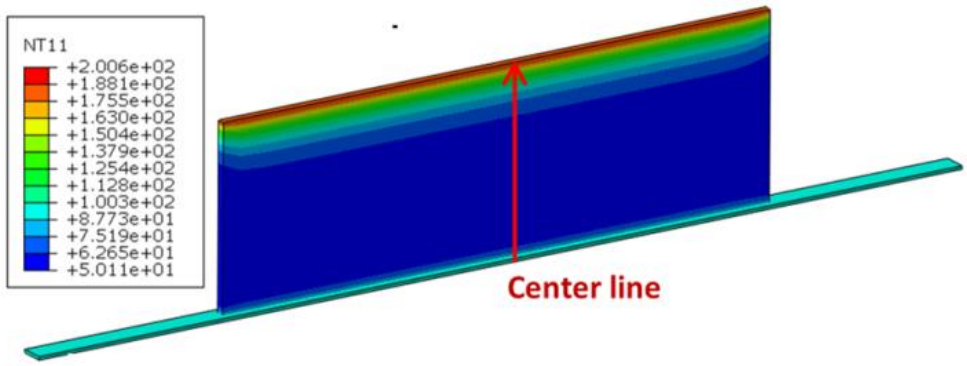

Figure 3-26. Temperature field at a specific time during the AM build, Reference [87].

Like the previous studies, References [45, 52] also used a FE analysis to determine the residual stress and warpage in a 3D printed semi-crystalline polymer. The parameters tested were the effect of ambient temperature, substrate temperature, raster pattern, layer thickness, and nozzle speed. The crystallization kinetics of the semi-crystalline polymer and the thermo-mechanical property of the whole part is evaluated. The model created was a thin plate with dimensions of 50x50x2 mm. The raster pattern was simulated by activating elements in the same material deposition pattern. The pattern-filled out the material in the X-Y plane and then proceeded up the Z-axis to the next X-Y plane. The material used in the study is polypropylene (PP), which tends to crystallize fast and has a higher shrinking rate than other commercially available polymers. The FE model accounts for the temperature-dependent properties, viscoelasticity, gravity, and crystallinity of the polymer. The results compared the experimental data to the numerical model at locations on the top and bottom of the printed part. The nozzle

speeds evaluated are 30 mm/s and 60 mm/s, while the ambient temperatures are 25 and 75 C. The study concluded that the increased ambient temperature (i.e., 25 to 75C) promotes increased bonding between the beads. It also reduces thermal stress due to the more homogeneous cooling conditions. Increasing the nozzle speed reduces the time between printed layers, which leads to lower crystallization. However, the thermal stresses can be reduced by an annealing effect created when a new bead is laid over an existing bead, and the existing bead is reheated. The increased nozzle speed enhances the annealing effect from the reheating of the lower bead. Raster patterns can reduce the warpage by 36 percent (zigzag pattern), and the decreased layer thickness can decrease the warpage by a staggering 89 percent. Both studies showed good agreement between the model and the experimental results.

More complex structures were studied in References [63, 99]. Reference [63] studied the effects of mesh size, material model, and time step size on the outcome of the simulation, and then compared the model to the experimental measurements. The design tested is a structure with multiple overhanging features or bridging, which required support structures in the experimentally printed model. They also modeled and tested a planar spring geometry. The work utilized element activation to simulate the thermal history. The model predicted the warpage within 23% error but was able to predict the deformation shape accurately. The research concluded that the time step used in the simulation has a more significant effect on the thermal profile but less of an impact on the overall warpage results. They also concluded that both the mesh size and overall part size used in the FEA models had a significant effect. The fine mesh produced very similar results to a coarser mesh for large models, when local effects are considered negligible. Reference [99] studied the temperature histories of different filling paths. The filling usually is incorporated in parts where increased surface area is needed, and there is no

need for solid material to fill the volume. This filling can have a honeycomb (hexagonal) cross section, grid, wiggle, or rectilinear geometry. The geometry is generally specified if there is a certain need for additional strength or to incorporate more connection points for complex features. The study revealed that the honeycomb pattern had the smallest temperature gradient. The stress field for the fill patterns was also studied. The honeycomb pattern also had the least amount of deformation, showing that the honeycomb pattern is the optimum choice for standard filling paths.

4 RESEARCH

4.1 INTRODUCTION

Big Area Additive Manufacturing (BAAM) provides the same overall benefits of general material extrusion AM. However, BAAM significantly increases the size limits, which restrict standard commercially available material extrusion equipment. Typical material extrusion printers allow for various size print envelopes but are commonly in the 0.20 m x 0.20 m x 0.20 m print chamber size [12]. Conversely, BAAM offers sizes in the range of 6.0 m x 2.3 m x 1.8 m. This size increase allows for designers to create large complex geometries, eliminate the need for hard tooling, and further enhance the concepts of direct digital manufacturing. While BAAM offers many benefits, there are design considerations that need to be accounted for that are not necessarily problems for traditional material extrusion parts. The larger bead sizes of BAAM introduce increased heat retention and weight not generally seen with common material extrusion AM equipment. At-risk features, areas susceptible to failure due to overhangs or bridging, require support material, which is proportionally larger to match the size of the parts. This support material increases the heat to the build. All the added heat from the build and support material exacerbates different failure scenarios. The increased applied heat can lead to part warping while layers start cooling, delamination, and sagging or slumping. In addition to the structural failure, BAAM builds have additional challenges, such as large step features when the layers are offset, and poor surface roughness which can become very prominent with increased layer sizes and nozzle diameter.

This research looks at the sagging phenomenon during the BAAM process. Sagging occurs when there is an overhanging or bridging feature present, and the weight of the material

applies a load more significant than the yield strength, generally at elevated temperatures, of the material supporting the feature. This phenomenon is dependent on the material properties, heat applied to the affected areas, and overall geometry of the build. This work uses an experimental model created in Reference [5] to validate the numerical models for the thermal analysis created in this work. Validation of the build's thermal history is critical as this information is needed to evaluate the build's stress history, which is used to predict the conditions where slumping can occur.

The experimental design was created to simulate the slumping failure mode. The design of the experimental structure allows for each layer to be produced at incrementally quicker print times. As the printed layers move upward, the combination of thermal retention and shortened time between layers produce the conditions for failure by slumping. The increase in average layer temperature reduces the strength of the material, which facilitates the failure of the build by slumping. During the experimental build, the structure failed when there was insufficient solidification of a layer before the subsequent layer was added. The quicker print times do not allow for each layer to cool below the glass transition temperature of the polymeric material. The warmer bead temperatures result in slumping beyond the plane of displacement threshold, [5]. This threshold is a value chosen where the part no longer can meet the functional needs due to the deviation from the designed geometry. Figure 4-1 shows the pyramid was almost completed before failure by slumping occurred.

Often in smaller parts created with typical FDM methods, overhanging features will utilize support structures. These support structures are either made of a sacrificial material or a less dense lattice structure to be removed after the build has been completed. However, in BAAM, the use of support structures increases the total print time, material costs, and can

increase the heat retention in areas. The increased time it takes to build the support structures could increase the chances of delamination due to greater layer cooling before the next layer can be added. Therefore, adding support structure should only be considered for situations where necessary.

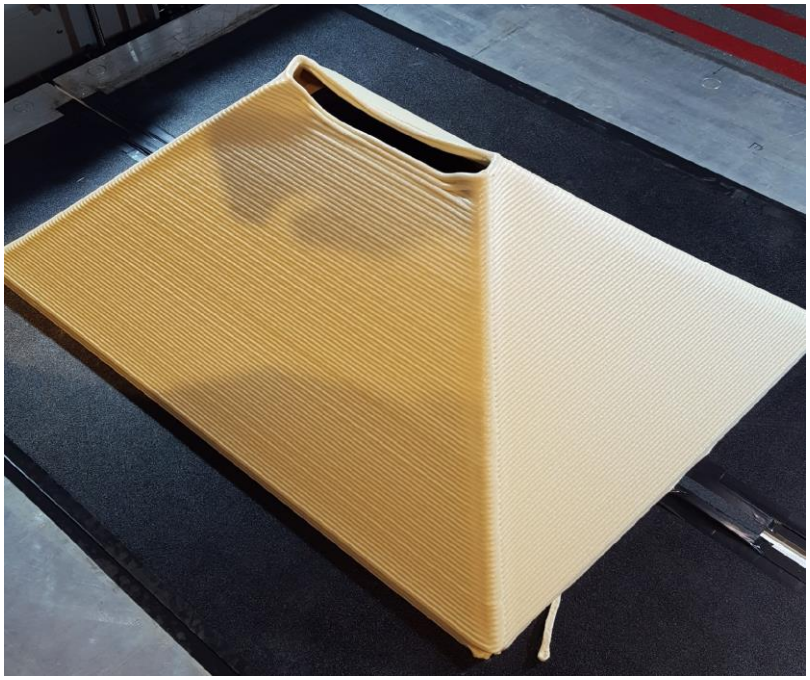

Figure 4-1. The fabricated structure from [5], designed to exacerbate the slumping failure.

Figure 4-1 shows structural failure at the top where enough heat is retained in the experiment to initiate slumping. The temperature recorded near the failed region was above the glass transition temperature when failure occurred. The glass transition temperature has been the cut-off point for successful bonding in ABS AM builds. However, if the temperature is greater than the glass transition temperature, then the material properties have little strength to support its weight, and the part is susceptible to failure, as noted in [83]. To prevent elastic collapse or deformation, the temperature in the supporting layer must be below the glass transition

temperature, which will serve as support for subsequent layers. Thermal monitoring and modeling in polymer extrusion 3D printing have both been explored in order to balance the trade-off between maintaining sufficient heat for bonding between layers versus solidifying one layer sufficiently before depositing the next. Infrared imaging has been explored as a quality measurement tool for thermal monitoring during additive manufacturing but remains absent mainly in production systems [12, 30, 72, 83, 100]. This work demonstrates the apparent value of tightly controlling the temperature envelope and geometry. For effective printing, the temperature should remain between two temperature limits. The low-temperature limit should cause sufficient solidification in which overhanging features do not deflect. The high-temperature limit should be warm enough that layers still bond well but not hot enough to cause the plastic collapse of the material. Therefore, it is essential to understand the BAAM system's thermal characteristics to enhance the stability of the BAAM part and decrease the failure factor of the printing systems.

4.2 Mathematical Transient Thermal Model

An additional general numerical study was created to further validate the finite element model results. Similar to the work done in [5, 44, 83], a numerical model is developed in Ansys Workbench 2021 R2 to determine the time-dependent temperature history of the built part. In this case, a model was developed to obtain the temperature variation over the entire build time. This allows for the temperature history of any layer in the build to be estimated. The numerical model evaluates the same pyramid geometry with one bead road thickness as the experimental build and the thermal simulation. However, due to the complexity of the numerical approach, all the material properties are assumed constant and that the entire bead thickness is a constant

temperature, as discussed further below. Therefore, this type of analysis may be well suited to estimate some geometries, materials, and processes but not all.

Figure 4-2 shows the schematic of a cross-sectional view for the printing process. Note that the layer cross section is shown as rectangular instead of a more oval shaped layer as seen experimentally. This was acceptable based on the work [97] where it was found that the air pockets inside the builds, caused by the oval bead cross sections had little to no effect on the heat transfer mechanisms of the build. The first layer is in contact with the print base, which has an isothermal boundary condition of 50°C ambient temperature assumed for the chamber. The ambient temperature used in the modeling is based off the ambient conditions of the experimental build. Layers one through seven were printed vertically, then subsequent layers were printed with an inclination to build a pyramid-type structure. Each bead has a slightly different heat transfer pathway, as shown in Figure 4-2. Figure 4-2 shows a schematic of the heat transfer paths, including conduction (denoted by the straight lines), radiation, and convection (denoted by the curved arrows). Following the schematics in Figure 4-2, the first printed layer transfers heat to only the base plate from the bottom surface by conduction and then to the environment by convection and radiation from the three free surfaces. When the second printed layer is deposited on top of the first, there is a conduction path from the second layer to the first. Convection and radiation paths are shown from the three free edges of the new top bead and two free sides of the first bead. At this point, there is still a conduction path between the first bead and the base plate. This pattern continues as each layer is added until the overhanging feature is reached.

The overhanging feature creates different heat transfer paths starting from layer eight. Once layer eight is deposited, heat is transferred through the contact area between bead eight and

bead seven by conduction. The eighth bead transfers heat to the atmosphere by convection and radiation from its open sides, including a partially open bottom side. As more layers are added to the build, the model continually transfers heat to the surrounding atmosphere or between the layers. These heat transfer mechanisms continue until the entire build has cooled and is in equilibrium with its surrounding environment.

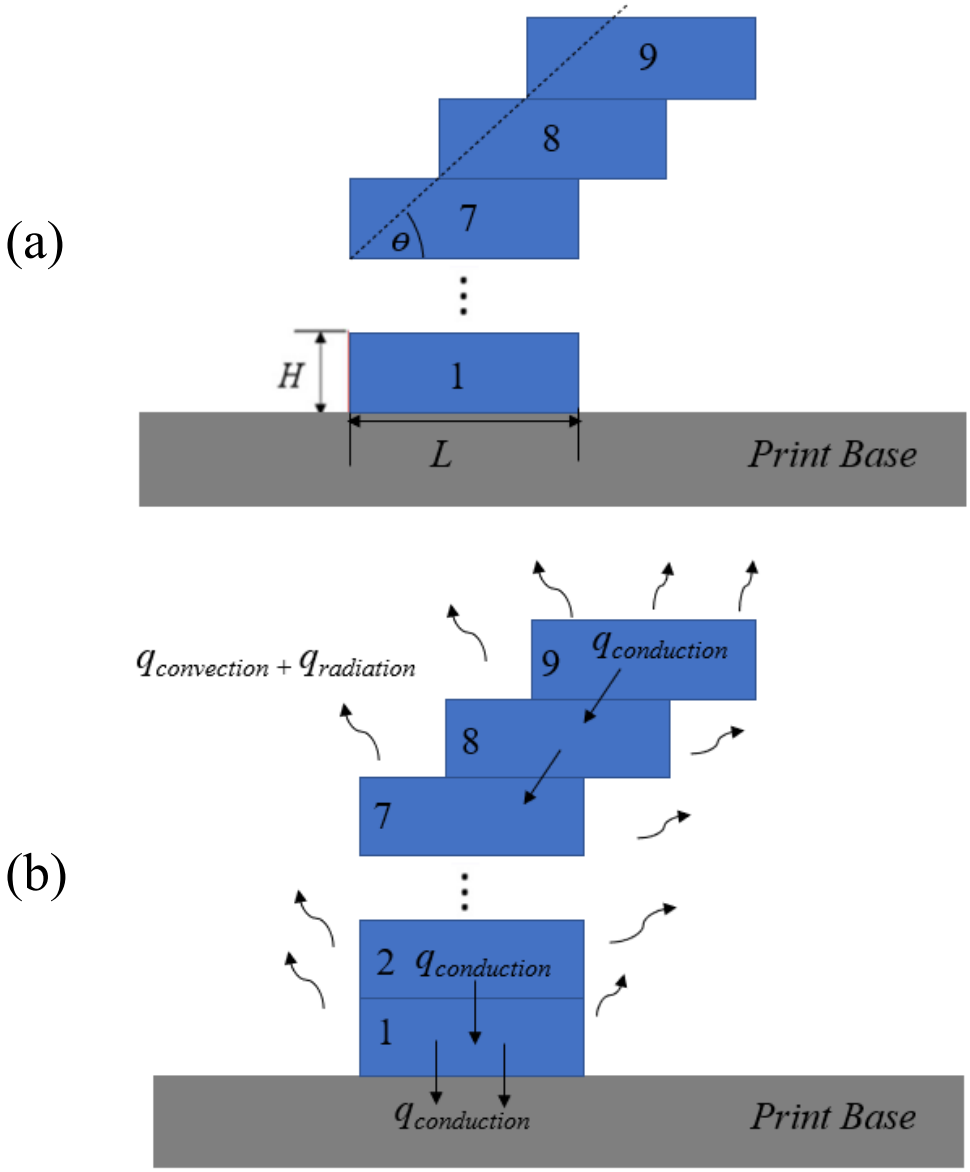

Figure 4-2. (a) Schematic of the printing beads and sequence for each layer, (b) schematic of the heat transfer paths for the print sequence.

The overhanging feature creates different heat transfer paths starting from layer eight. Once layer eight is deposited, heat is transferred through the contact area between bead eight and seven by conduction. The eighth bead transfers heat to the atmosphere by convection and radiation from its open sides, including a partially open bottom side. As more layers contribute to the build, the model continually transfers heat to the surrounding atmosphere or between the layers. These heat transfer mechanisms continue until the entire build has cooled and is in equilibrium with its surrounding environment.

In order to determine how to treat the transient thermal model, the Biot number (dimensionless) was used to determine if a lumped system analysis was sufficient for the transient heat model. A calculated Biot number under 1 determines that a model with convection, conduction, and radiation boundary conditions was sufficiently small enough to be "thermally thin," allowing the temperature to be assumed constant through the thickness [65]. The Biot number here is 0.38. Therefore, convection, conduction, and radiation are the main heat transfer mechanisms for the system. Additionally, the heat transfer due to heat of fusion from the phase change by crystallization is usually around an order of magnitude smaller than the total heat transfer by convection, conduction, and radiation, which is the reason it was neglected in this study [101].

The energy balance equation method, Equation 4-1, was used to find the temperature profiles for each layer over a range of time. This was completed by dividing the medium into enough volumetric elements, which in this case is each bead, and then applying the energy balance method for each element [5, 65, 79, 83]. The energy balance equation is defined as follows:

$$mc_p \frac{dT}{dt} = hA_s(T - T_{film}) + \varepsilon\sigma A_s(T^4 - T_{surr}^4) + kA_{contact}\frac{T - T_{contact}}{L} \quad \textit{Equation 4-1}$$

where

$m = \rho V$ = mass, Kg

ρ = bead density, Kg/m^3

V = volume, m^3

c_p = heat capacity of the bead material, (J/K)/Kg

T = bead temperature, ℃

T_{surr} = temperature of the surroundings to which the element radiates, ℃

T_{film} = film temperature for natural convection, ℃

$T_{contact}$ = temperature of neighboring beads in contact, ℃

ε = emissivity

t = time, s

h = heat transfer coefficient, W/(K*m^2)

k = thermal conductivity, W/(K*m)

L = bead width, m

A_s = surface area, m^2

$A_{contact}$ = surface area in contact between beads or first bead and base plate, m^2

σ = Stefan-Boltzmann constant

Each bead has four different surrounding temperatures, T_{surr}, the temperatures are associated with the top, bottom, right, and left surfaces of a bead for heat transfer by radiation

(assumed as 50°C). The T_{film} is the film temperature for natural convection, in this case it is the average of the ambient and surface temperatures (140°C). The surface area, A_s, is specified per bead element number. This value is calculated by determining the node number, incline angle, contact length, and printing sequence. The heat transfer coefficient was obtained by calculating the Nusselt number, Nu, which is the natural convection equation and a function of both the Rayleigh, Ra_L, and Prandtl, Pr, numbers [65]. Since the heat transfer coefficient depends on the geometry of the feature in question the following equations are used to determine the heat transfer coefficient for different geometries and orientations:

General definition: $$Nu = hL/k$$ *Equation 4-2*

Vertical Surface: $$Nu = \left[0.825 + \frac{0.387Ra_L^{1/6}}{\left(1 + \left(\frac{0.492}{Pr}\right)^{\frac{9}{16}}\right)^{\frac{8}{27}}}\right]^2$$ *Equation 4-3*

Horizontal upper surface: $$Nu = 0.54Ra_L^{1/4}$$ *Equation 4-4*

Horizontal lower surface: $$Nu = 0.27Ra_L^{1/4}$$ *Equation 4-5*

Equations 4.3 through 4.5 are used to determine the Nusselt number for the different geometries and those solutions are used in Equation 4.2 to effectively determine the heat transfer coefficient for that portion of the element [65]. This iterative calculation is validated by confirming the values from the experiment in Reference [5] as well as by the transient thermal FEA model. Note that the above equations are dependent on the geometry of the layers and are different if other geometries are assumed.

Since Equation 4.1 is an explicit model, the printing speed and length of the print path was used to determine the print time for each layer. As the material is extruded to make the overhanging feature, the time to create each layer is reduced due to the ever-decreasing print path. The printing time for each layer after layer seven can be calculated by the following expression:

$$\Delta t_i = \frac{2(L_1 + W_1) - 8(\tan(\theta))(i-7)H}{u} \qquad \textit{Equation 4-6}$$

where

Δt_i = printing time for each layer, s

L_1 = length of the bead, (1.06 m)

W_1 = width of the bead, (0.77 m)

H = bead height, (.005 m)

i = layer number

u = print speed, m/s

θ = angle of inclination, deg.

The printing speed from the experiment in Reference [5] was set to 0.041 m/s and the angle of inclination was set to 40 degrees. The relationship between print time and layer number is linear. As the number of layers increases the time it takes to complete the layer is reduced.

4.2.1 Mathematical Transient Model Results

The results from the thermal transient model for a one bead road structure is shown in Figure 4-3. The thermal profile shown is a snapshot for the temperatures of each layer as the 25 layer is added to the build.

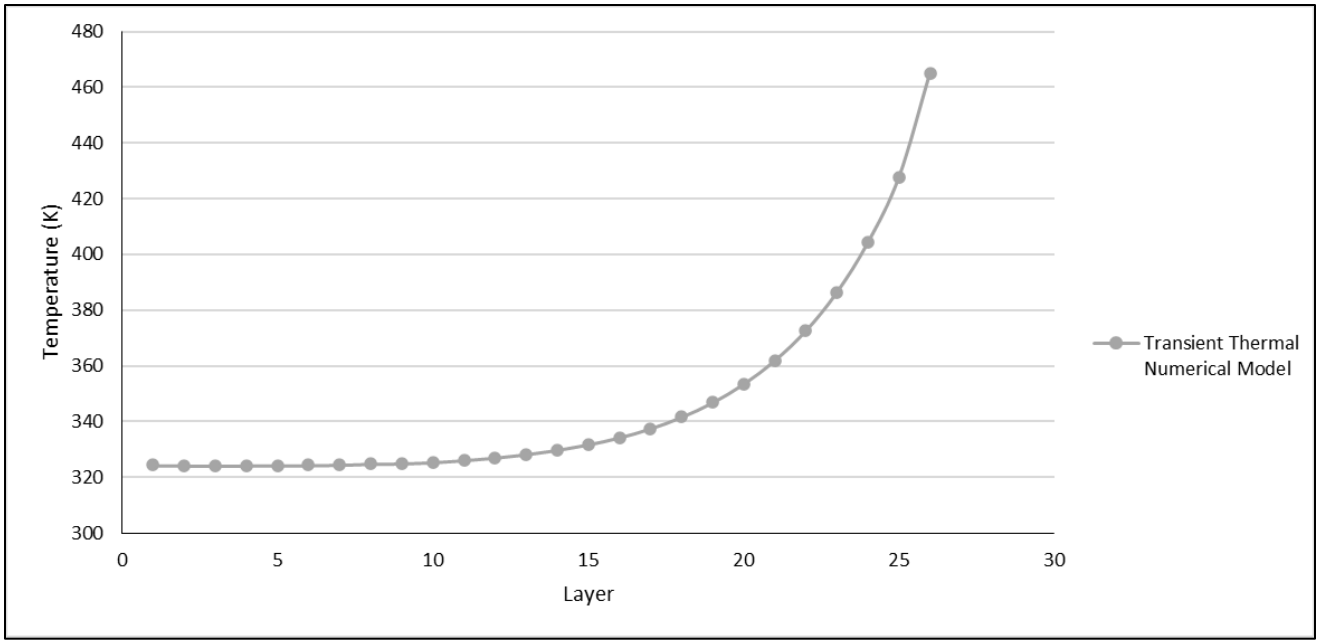

Figure 4-3. Temperature profile for the numerical model with 25 layers.

The results show an exponential decrease in temperature from the top layer to the bottom layer (exponential cooling) for the build temperature profile. The newest layer is at the extrusion temperature while the one bead thick layer is rapidly cooling until it reaches equilibrium with the baseplate and/or ambient temperatures. This is the expected outcome and matches the results seen in References [83, 102]. A comparison between all the results is included in the results chapter.

4.3 Finite Element Analysis

4.3.1 Structure and Simulation Model

The model for ABS experimentally built-in Reference [5] is shown in Figure 4-4. The model was designed to incite the slumping failure as seen in Figure 4-1. The bead road width used in this experiment is 12.5 mm while the thickness is 5 mm. These are typical sizes for

creating BAAM models. The geometry used in this experimental structure allows for changing cooling rates to be studied. The difference between the overall length and width of the model allows for examination of how the geometry can affect heat retention. Additionally, the decreasing print path for each layer should increase the heat retention in the model sufficiently to show the effects of decreased cooling between layers.

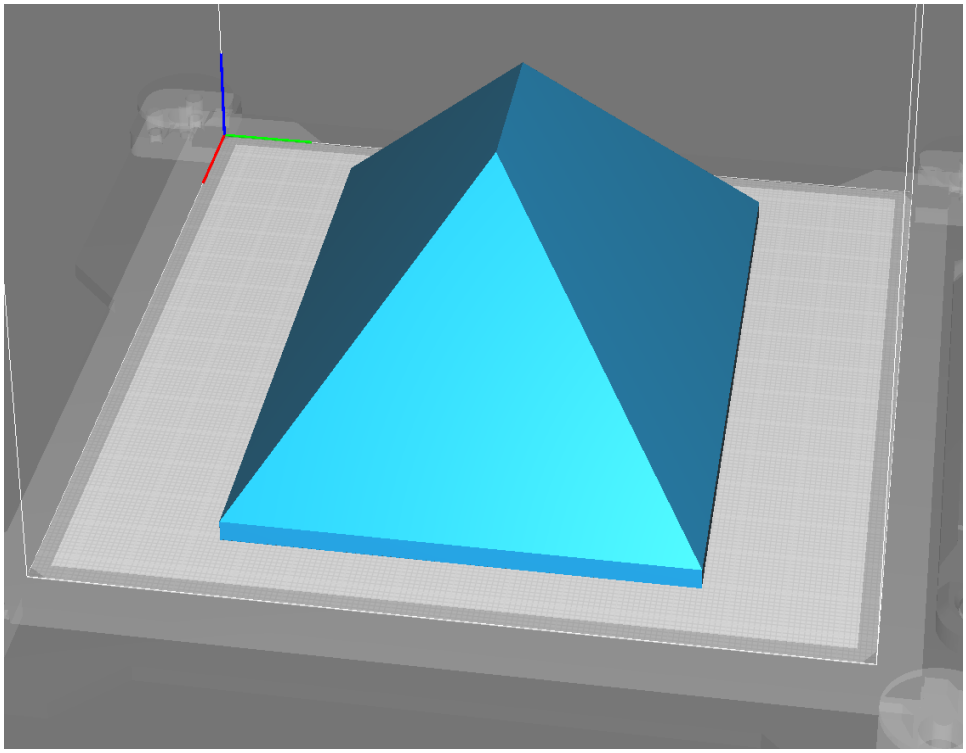

Figure 4-4. Benchmark structure used in the experimentation and modeling with ABS (Acrylonitrile Butadiene Styrene)[5].

The simulation model was created in Ansys, where the walls were created to match the dimensions in the experimental pyramid. The experimental pyramid had bead dimensions of 12.5 mm wide and a thickness of 5 mm. The overall size was 1.06 m by 0.77 m.

The simulation model was created to analyze one-quarter of the total size and match the deposition parameters in the experiment. By utilizing symmetry, only one corner was built in the

model. The simulation model was built up to 54 layers. Figure 4-5 shows the simulation model created for the coupled thermal-structural analysis. The model was created from the base up, which allows for the model to sit on the datum planes and in the proper orientation for the simulation. Once the base plate was created, a new plane was inserted on the extruded structure. A new plane was added after each solid geometry. The new planes allow for the proper direction and starting location to extrude the next layer. Each layer was created separately, which is indicated by the different colors seen at each layer. Independent material properties, temperatures, and heat transfer mechanisms can be specified by isolating each layer. More importantly, each layer can be independently activated and deactivated by the element birth/death functions. Note that the first seven layers are combined into one layer for model simplicity and reduction in computational power required to run the simulations. Combining these layers into one layer is justified since the layers of interest are far enough away that no compounding effects manipulating the results.

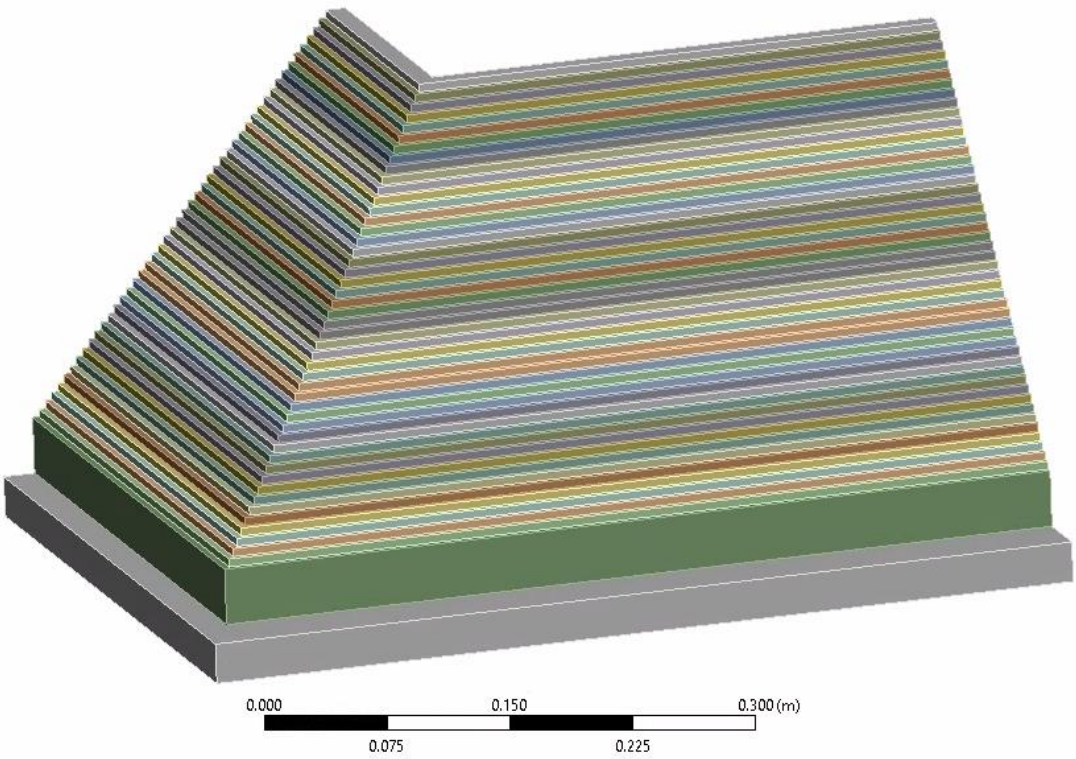

Figure 4-5. Simulation model geometry

The mesh created for each layer and base plate used the same recommended settings. The meshing method created tetrahedron element geometries and was refined once to obtain the final mesh. The mesh sizing was set for adaptive sizing and mesh defeaturing. The element geometries were set to have slow transitions and medium span angles. The resolution, defeature size, element order, element size, and element quality were all set to default and program controlled. The program recommended controls created a total of 194,831 nodes and 83592 elements and the average mesh area was found to be 3590 mm^2. Figure 4-6 shows mesh and node locations of the floor and layers. Additionally, the mesh refinement was set to 2 for the mesh sensitivity studies (i.e., the average mesh increased by a factor of 2). The mesh created for the sensitivity studies is shown in Figure 4-7. Other mesh geometries were considered, but the tetrahedron mesh geometries were better suited to match the layer nodes when set to programmed control.

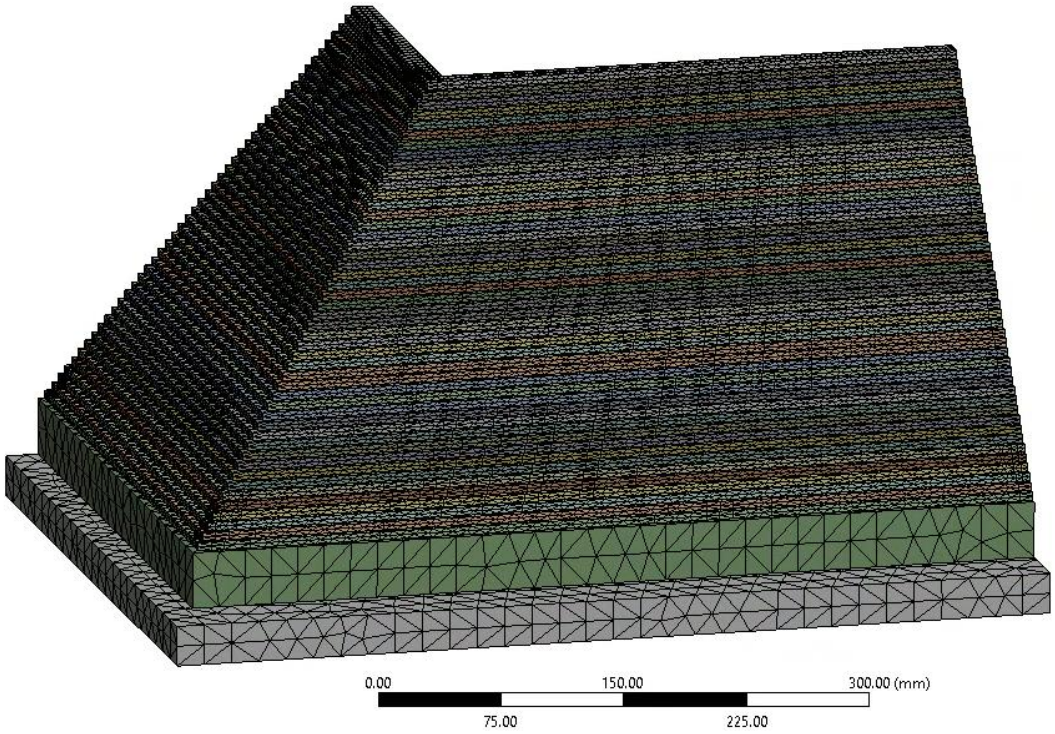

Figure 4-6. Mesh distribution for the FEA model.

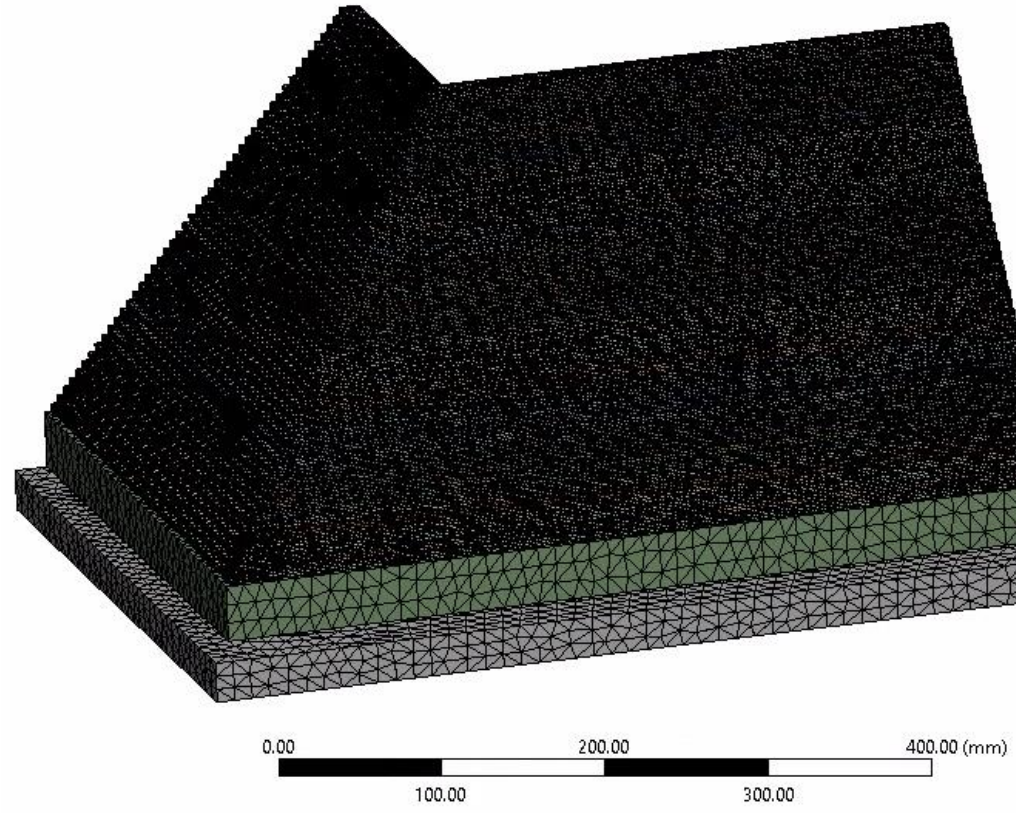

Figure 4-7. Mesh distribution for the FEA mesh sensitivity model.

4.3.2 Simulation model – Transient Thermal Analysis

This section details the specific inputs to the simulation model needed for the thermal analysis. The steel base plate was created to provide a constant base temperature during the simulation, this isothermal boundary condition matches the experimental set-up. The base plate was set to have standard structural steel thermal properties and was considered rigid for the analysis. Each layer was created independently, the layer isolation allowed for element birth/death commands and for layer-specific mesh parameters.

Using the built-in element birth/death commands each layer is activated one-by-one until the model is built. The birth/death interface assigns each layer as "Dead" or "Alive" on each step created. Element death refers to the case when the stiffness and conductivity of an element is reduced, 1E-6 Pa and 1E-6 $Wm^{-1}K^{-1}$, to essentially non-existent, and having extremely little influence on the surrounding elements [95]. Where element birth refers to the state where the layer regains its typical stiffness and conductivity. Each layer was marked as dead until its designated step was reached, where it would then be assigned alive. The element birth/death functions were implemented into the model by creating separate steps for each layer. Each step is independently defined by time. This allows for the simulation to match the time for each layer as it was created in the experimental model. The layers, steps, and associated time are shown in Table 4-1. As each new layer is activated, a temperature input of 200°C is also activated and then the temperature is accordingly turned off as the next layer is activated. Once an element is activated it is not deactivated again. Once the temperature is turned off it no longer is adding heat into the system but instead is now able to transfer heat to/from the layers around it. All the new layers activated have the extrusion temperature of 200°C applied through the thickness of the bead.

Table 4-1. Layer number and step for associated activation time.

Layer No.	Step	Time (sec.)	Layer No.	Step	Time (sec.)	Layer No.	Step	Time (sec.)	Layer No.	Step	Time (sec.)
0	0	0	21	15	3651.6	36	30	5642	51	45	7087.4
7	1	1302.5	22	16	3801.3	37	31	5755.4	52	46	7238.9
8	2	1485.6	23	17	3948.5	38	32	5866.3	53	47	7310.9
9	3	1666.7	24	18	4093.3	39	33	5974.7	54	48	7380.7
10	4	1845.5	25	19	4235.7	40	34	6080.8			
11	5	2021.8	26	20	4375.7	41	35	6184.4			
12	6	2195.7	27	21	4513.2	42	36	6285.6			
13	7	2367.1	28	22	4648.3	43	37	6384.4			
14	8	2536.2	29	23	4781	44	38	6480.7			
15	9	2702.8	30	24	4911.3	45	39	6574.6			
16	10	2867	31	25	5039.1	46	40	6666.2			
17	11	3028.7	32	26	5164.6	47	41	6755.2			
18	12	3188.1	33	27	5287.6	48	42	6841.9			
19	13	3345	34	28	5408.2	49	43	6926.1			
20	14	3499.5	35	29	5526.3	50	44	7007.9			

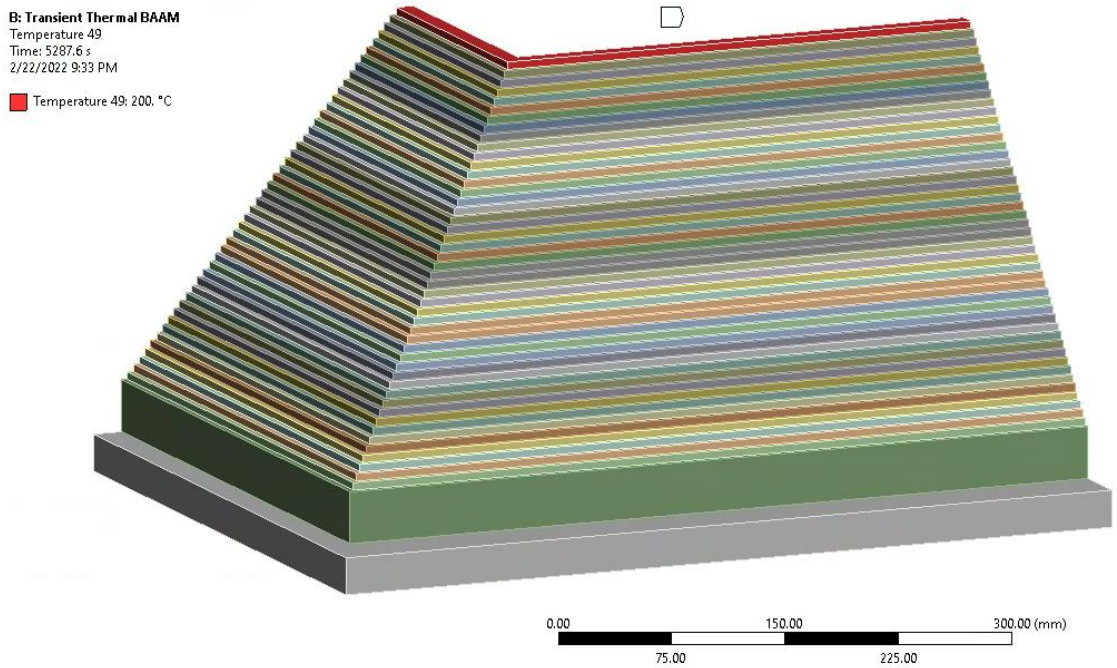

Figure 4-8. Temperature input on the 54th layer.

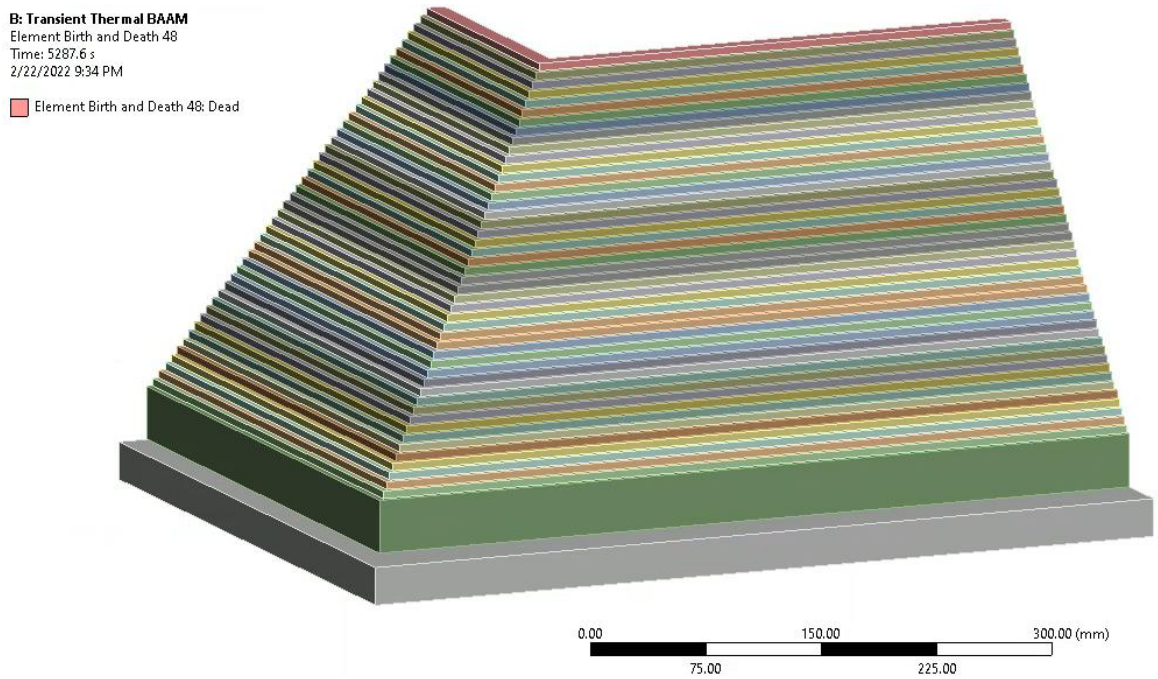

Figure 4-9. Element/birth and death applied to the 54th layer.

The ABS material properties and heat transfer coefficient of the structures were input as a function of temperature. The material property values were added to the model to ensure all characteristics were captured within the 22°C to 200°C temperature range. All the material properties used in the thermal analysis are further detailed in Section 4.3.4.

The ambient temperature of the model was set at 50°C for the convection and radiation conditions. The temperature monitoring during the experiment build confirms that the ambient temperature can be considered constant. The open surface of each layer was selected for convection and radiation heat transfer mechanisms to be active once the layer was active, as shown in Figure 4-10 and Figure 4-11. Since the model was created to account for symmetry of the experimental build, the section edges needed to be perfectly insulated, so there was no heat loss through the cross section of the symmetry planes. Figure 4-12 shows the heat flow was set to

0W, creating an insulating boundary condition to the model. The contact areas between two layers were chosen as being bonded, allowing for conduction between the surfaces, as shown in Figure 4-13. Conduction values were then program controlled, which updates the values as the temperature between the faces varies.

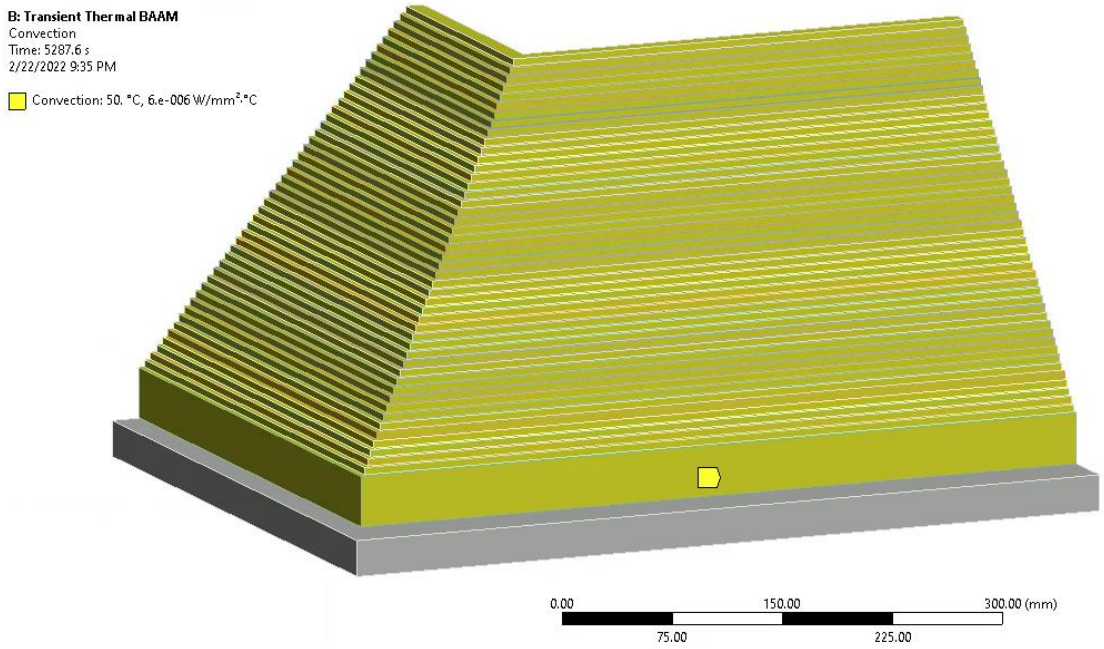

Figure 4-10. Convection boundary conditions for the thermal simulation.

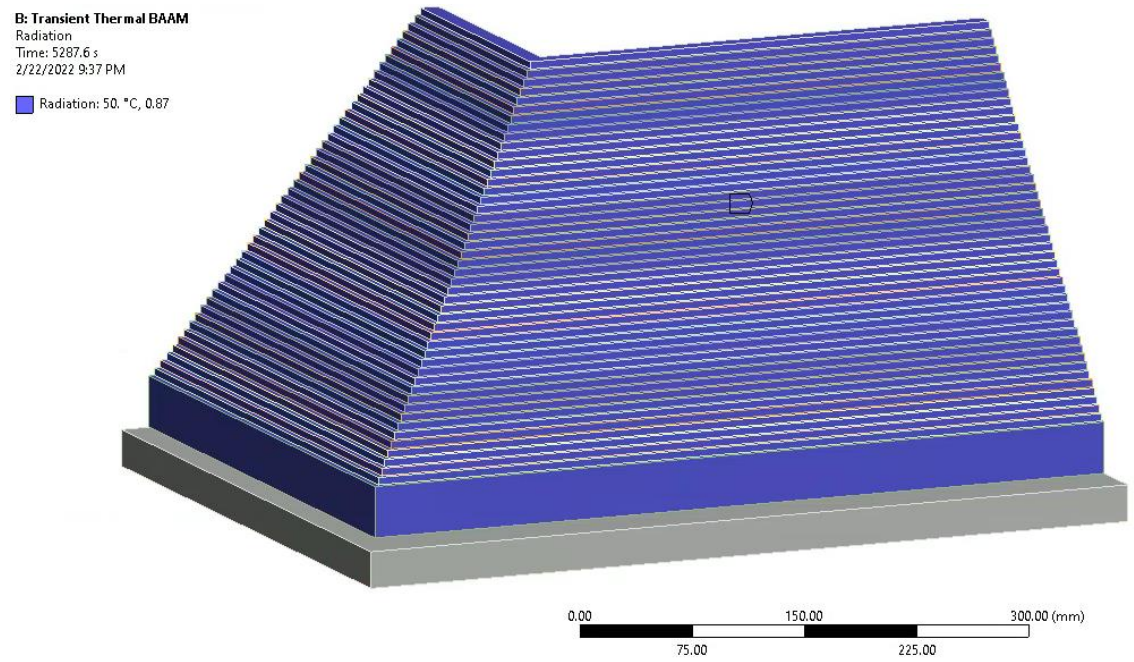

Figure 4-11. Radiation boundary conditions used for the thermal analysis.

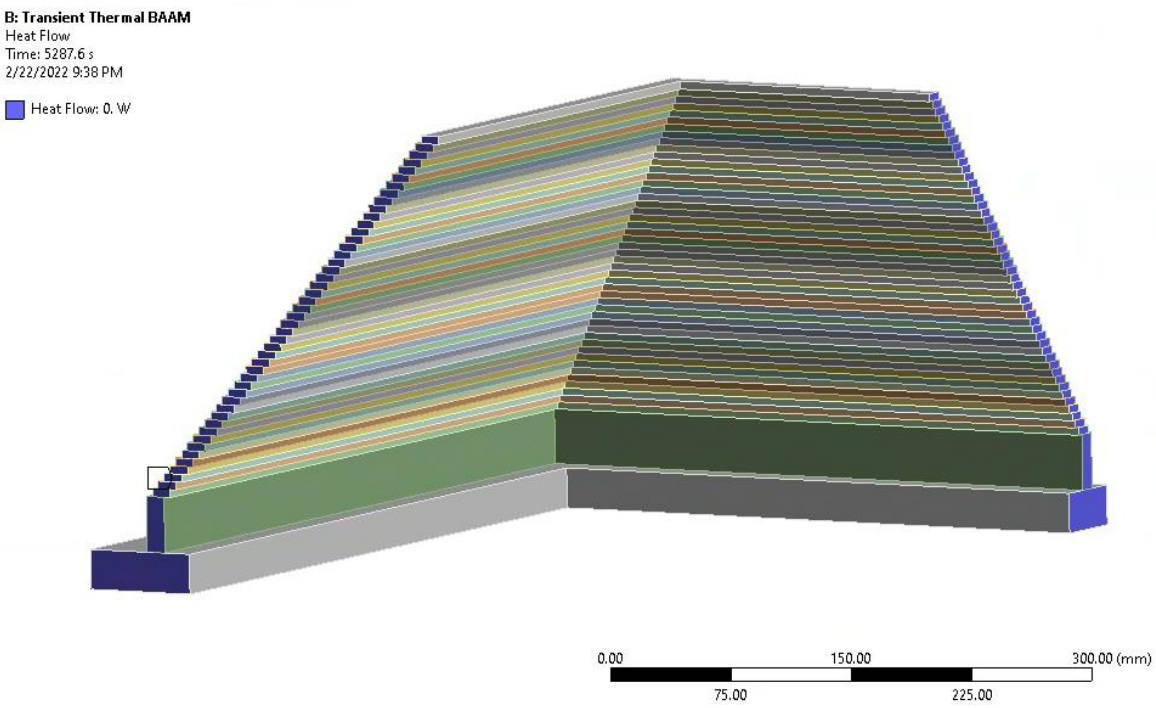

Figure 4-12. Heat flow boundary conditions used for the thermal simulation to produce proper symmetry for the heat transfer mechanisms.

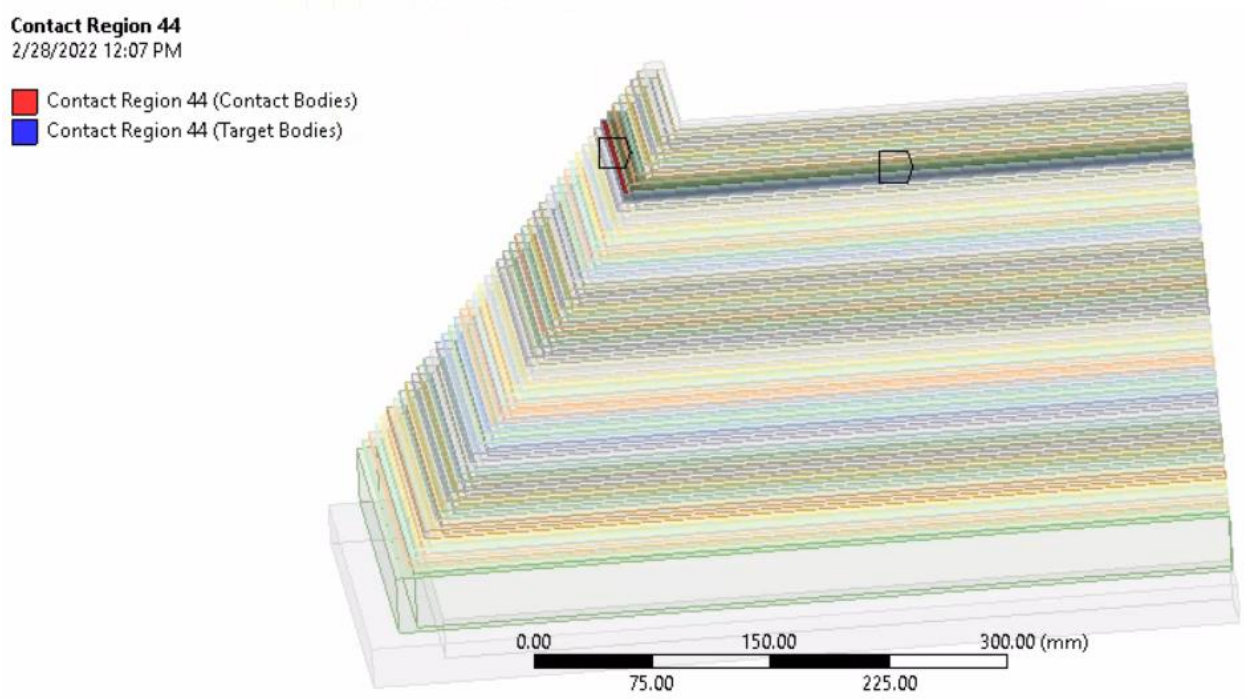

Figure 4-13. Contact regions between layers, selected as bonded contacts.

The thermal simulation analysis settings were setup to keep as many parameters as "Program Controlled", which means the standard settings in Ansys were used. This assumption was validated by comparing against the mesh sensitivity study. Utilizing the program-controlled functions reduced the potential for analysis errors in addition the time for each analysis to finish was not great enough to warrant changing the solver requirements to reduce overall computational time. For reference, Table 4-2 shows the radiosity, nonlinear, and output control settings used in the thermal analysis.

Table 4-2 Thermal simulation analysis settings.

Radiosity Controls	
Radiosity Solver	Program Controlled
Flux Convergence	1.e-004
Maximum Iteration	1000.
Solver Tolerance	1.e-007 W/mm²
Over Relaxation	0.1
Hemicube Resolution	10.
Nonlinear Controls	
Heat Convergence	Program Controlled
Temperature Converge...	Program Controlled
Line Search	Program Controlled
Nonlinear Formulation	Program Controlled
Output Controls	
Calculate Thermal Flux	Yes
Contact Data	Yes
Nodal Forces	No
Volume and Energy	Yes
Euler Angles	Yes
General Miscellaneous	No
Contact Miscellaneous	No
Store Results At	All Time Points
Result File Compression	Program Controlled

The simulation is expected to follow the following thermal governing equation [65]:

$$\underbrace{mc_p \frac{dT}{dt}}_{\text{Rate of energy storage inside the volume}} = \underbrace{k\left(\frac{\partial^2 T}{\partial x^2}+\frac{\partial^2 T}{\partial y^2}+\frac{\partial^2 T}{\partial x^2}\right)}_{\text{Rate of heat conduction}} + \underbrace{q}_{\text{Rate of heat flux/convection/radiation/internal heat generation inside the volume}} \qquad \textit{Equation 4-7}$$

$$q = hA_s\left(T - T_{film}\right) + \varepsilon\sigma A_s\left(T^4 - T_{surr}^4\right) \qquad \textit{Equation 4-8}$$

where

$m = \rho V =$ mass, Kg

$\rho =$ bead density, Kg/m^3

$V =$ volume, m^3

$c_p =$ heat capacity of the bead material, (J/K)/Kg

$T =$ bead temperature, °C

$T_{surr} =$ temperature of the surroundings to which the element radiates, °C

$T_{film} =$ film temperature for natural convection, °C

$\varepsilon =$ emissivity

$t =$ time, s

$L =$ bead width, m

$h =$ heat transfer coefficient, W/(K*m^2)

k = thermal conductivity, W/(K*m)

$A_s =$ surface area, m^2

$\sigma =$ Stefan-Boltzmann constant

Even though the Biot number calculated in Section in 4.2 was under 1, there is no penalty to calculate the temperature distribution through the layer. Therefore, equations 4-7 and 4-8 can be used to find the layer temperature and the temperature distribution through each layer.

4.3.3 Simulation Model – Structural Analysis

The structural simulation was also modeled in Ansys, where the model used was the same as the transient thermal model (Section 4.3.2), mesh and overall build (Section 4.3.1), and material properties (Section 4.3.4). The Ansys Workbench structural solver was used to take the transient thermal results file from the previous thermal simulation and use those results as the thermal load case. The temperature history from the transient thermal model was imported and used as the load case, as shown in Figure 4-14. The mesh and overall build were kept the same as the transient thermal model simulation.

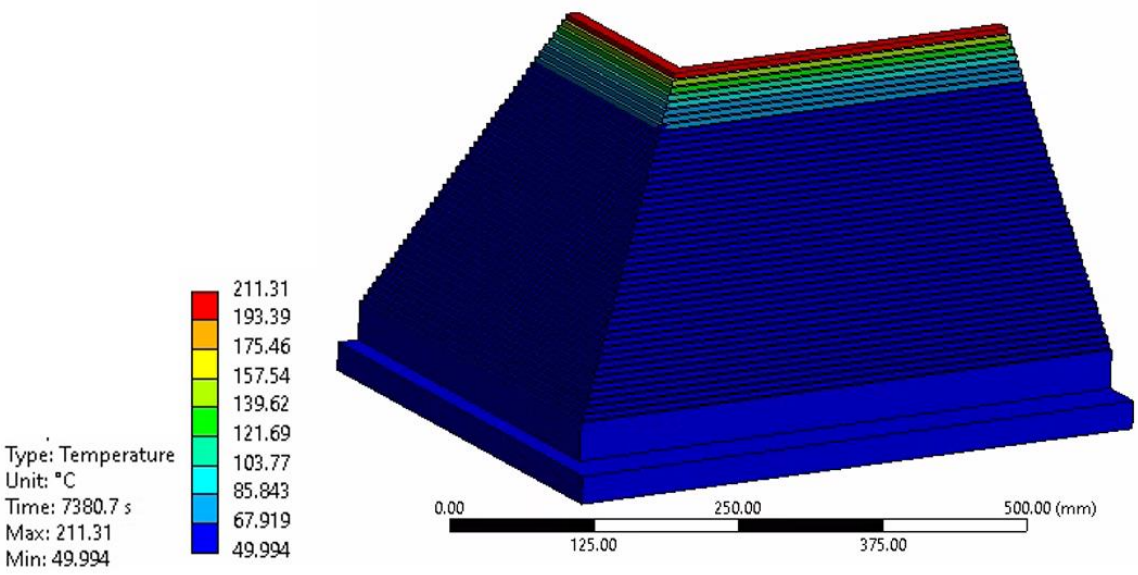

Figure 4-14. Example of the time-history thermal profile used as the load input to the structural simulation.

Since the same model, including the mesh, was used from the transient thermal model, only minor adjustments needed to be made to constrain the model and apply the additional structural analysis boundary conditions. The base plate, as mentioned previously, was set as structural steel and at a constant temperature from the thermal model. This ensures that there are little to no thermal stresses acting on the base plate and is consistent with the experimental set-up. The boundary conditions applied to the model are shown in Figure 4-15. The base plate was fixed in all directions to support the build. Since the model was reduced by symmetry, frictionless supports were added to the cross-sectional face of the symmetry planes. Frictionless supports are often used to constrain models when it is not desired to deflect in specific directions. In this case, the frictionless supports keep the symmetry plane cross-sections from moving normal to their respective symmetry planes. Standard Earth gravity was the only additional load case added to the model as shown in Figure 4-15.

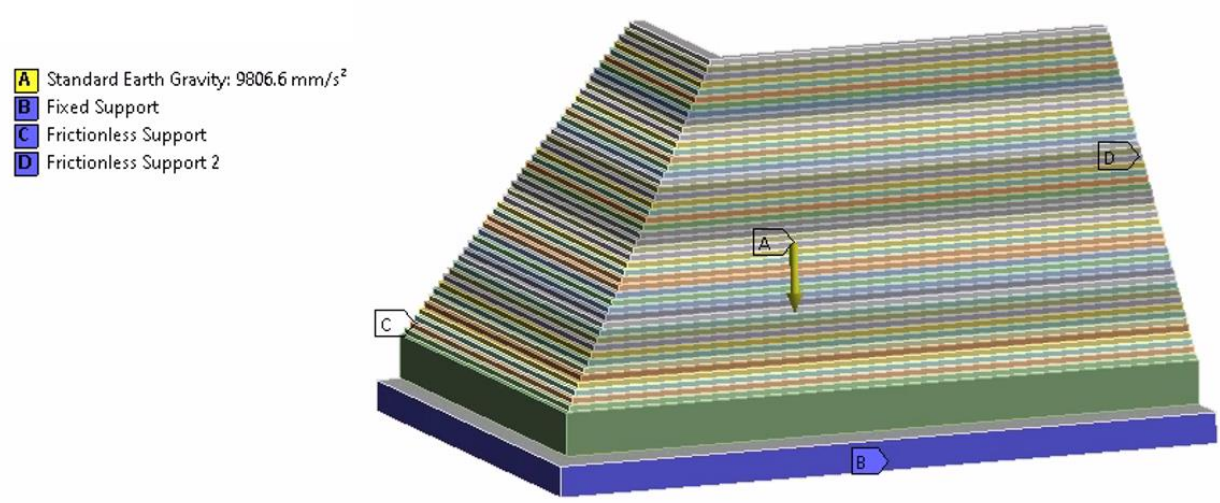

Figure 4-15. Structural simulation model showing the boundary conditions used in the simulation.

Layer model constraints were required for the structural analysis but not the thermal simulation analysis, as this was how the layer-to-layer and layer-to-base plate were connected. The build was set to have a mechanical tie to base plate. This approach was appropriate due to the assumption that there would be no delamination between the base plate and the first layer. Each layer was also set to be mechanically tied. The mechanical tie makes it, so the layers must be connected throughout the simulation. This is an appropriate assumption due to the size of the weld zone and the increasing heat retention in the model, which does not allow for delamination. Delamination was not experimentally observed to occur, which is the reason to not include it in the model. If delamination were more of a concern, then the layer friction and the size of the layer binding area could be introduced to the simulation.

The structural simulation analysis settings were setup to keep as many parameters as reasonable "Program Controlled." This assumption was validated by comparing against the mesh sensitivity study. Utilizing the program-controlled functions reduced the potential for analysis errors. In addition, the time for each analysis to finish was not significant enough to warrant

changing the solver requirements to reduce overall computational time. For reference, Table 4-3 shows the rotordynamics, nonlinear, and output control settings used in the structural analysis.

Table 4-3. Structural simulation analysis settings.

Solver Controls	
Solver Type	Program Controlled
Weak Springs	Off
Solver Pivot Checking	Program Controlled
Large Deflection	Off
Inertia Relief	Off
Quasi-Static Solution	Off
Rotordynamics Controls	
Coriolis Effect	Off
Nonlinear Controls	
Newton-Raphson Option	Program Controlled
Force Convergence	Program Controlled
Moment Convergence	Program Controlled
Displacement Convergence	Program Controlled
Rotation Convergence	Program Controlled
Line Search	Program Controlled
Stabilization	Program Controlled
Output Controls	
Stress	Yes
Surface Stress	No
Back Stress	No
Strain	Yes
Contact Data	Yes
Nonlinear Data	No
Nodal Forces	No
Volume and Energy	Yes
Euler Angles	Yes
General Miscellaneous	No
Contact Miscellaneous	No
Store Results At	All Time Points
Result File Compression	Program Controlled

The governing equations used in Ansys to determine the distortion of the model can be described as shown below in Equation 4-9. This equation takes into account the strain history and thermal strains seen at each node [113].

$$\boldsymbol{F^{ext}} = \int_{\boldsymbol{\Omega}} \boldsymbol{B^T D B u d\Omega} - \int_{\boldsymbol{\Omega}} \boldsymbol{B^T D B \varepsilon^{th} d\Omega} \qquad \textit{Equation 4-9}$$

where

$\boldsymbol{F^{ext}}$ = External loads

$\boldsymbol{u}$ = Displacement vector

$\boldsymbol{\varepsilon^{th}}$= (αΔT) Thermal strain vector

$\boldsymbol{\Omega}$ = Integration domain

$\boldsymbol{B}$ = Finite element shape function matrix

$\boldsymbol{D}$ = Elastic/relaxation modulus matrix

Since ABS is a viscoelastic material the thermal stress equations can be determined by accounting for the elastic and viscous responsese of the material. The following equations can be used to describe the total stresses (including thermal) seen in the model.

$$\boldsymbol{\sigma}_{n+1} = K\left(e_v^n - e_v^{(n+1)th}\right)I + 2G_\infty e_{n+1} + \sum_{i=1}^{N}(s_i^n)\exp\left(\frac{-\Delta\psi}{\tau_i}\right) + 2exp\left(\frac{-\Delta\psi_{1/2}}{\tau_i}\right)G_i\Delta e \qquad \textit{Equation 4-10}$$

$$\Delta\psi = \int_{t_n}^{t_{n+1}} A\big(T(s)\big)ds \quad and \quad \Delta\psi_{1/2} = \int_{t_{n+1/2}}^{t_{n+1}} A\big(T(s)\big)ds \qquad \textit{Equation 4-11}$$

$$G = G_\infty + \sum_{i=1}^{N} G_i \exp\left(-\frac{t}{\tau_i}\right) \ and \quad K = K_\infty + \sum_{i=1}^{N} K_i \exp\left(-\frac{t}{\tau_i}\right) \qquad \textit{Equation 4-12}$$

Where

σ_{n+1}= current stress step, Pa

$\tau_i(t)$ = (η/G) relaxation time at temperature, s

$e_v^n(t,T)$ = volumetric strain, m^3/m^3

$A(T(s))$ = shift function

t_n = time at load step, s

$G,\ G_\infty,\ G_i$ = shear modulus according to the relaxation kernel, Pa

$K,\ K_\infty,\ K_i$ = bulk modulus, Pa

s_i^n = shear stress history, Pa

E = relaxation modulus function, Pa

Δe = incremental deviatoric strain, m/m

e_v^{th} = volumetric thermal strain, m^3/m

I = identity tensor

η = viscosity, Pa-s

Equations 4-10 through 4-12 are used to describe the viscoelastic responses during the simulation [113]. However, Ansys is able to utilize the Prony series discussed in Section 3.10.3 to convert between the dynamic modulus, creep compliance, and the relaxation modulus [112]. Therefore, Equation 4-12 is shown as a reference to how the Prony series would look for the relaxation modulus, creep compliance, and dynamic modulus.

4.3.4 Material Properties

The material used in the simulation model is pure ABS. In general, ABS is one of the most widely used thermoset polymers in AM and traditional manufacturing techniques (i.e., extrusion molding or blow molding). ABS material properties are known to have high rigidity, good impact resistance, good insulating properties, good abrasion and stain resistance, good weldability, good dimensional stability over time, and high surface brightness when dyed [32, 46], these features make it a popular choice for use by material extrusion AM.

The material used in the experimental build from Reference [5] is ABS with 20% glass fiber by weight. This material is commonly used for large-area additive manufacturing since it

has reduced the final build's warpage compared to pure ABS material [13]. This difference in warpage or distortion is due to significant thermal expansion induced stresses caused by the heat input and cooling of the layers [13]. Even though the experimental build was created with ABS/glass fiber material, the simulation was modeled with pure ABS. The two main reasons to model the simulation with pure ABS instead of the ABS/glass fiber mixture are a review of open literature data on pure ABS showed minor differences in most of the material properties. All the ABS material properties needed for the simulation were found in peer-reviewed publications. As ABS/glass fiber material is less utilized, the number of sources for material properties are limited. The greatest differences in mechanical properties between pure ABS and ABS/glass fiber material is the coefficient of thermal expansion, tensile strength and Young's modulus. However, Young's modulus and tensile strength are very dependent on the orientation as ABS/glass fibers are more orientation sensitive than pure ABS. This shows that the two materials can actually have the same values when compared in orientations where the loads are normal to the welds [11].

Additionally, a slight difference in thermal conductivity, heat capacity, and Young's modulus do not significantly affect the predicted warpage [60]. However, it has been found that one of the most influencing factors for warpage is the coefficient of thermal expansion (CTE) [60]. Pure ABS has a larger CTE than ABS/glass fiber material, but as mentioned previously, the CTE can significantly vary from 7.0 to 15.0 x 10^{-5}/°C [59]. Therefore, a lower value (9.5 x 10^{-5}/°C) of pure ABS was chosen for this model [81]. A sensitivity study to determine the effects of different CTE determined that increasing the CTE increased the warpage by the same factor [60]. Therefore, the CTE is expected to be close to the actual test material CTE when the warpage predicted by the model is similar to that observed in the experiment. In addition, due to the

geometry of the build being a single wall thickness, it is not expected that the difference in material properties would significantly affect the results. Therefore, as described herein, there is no expectation that a model using these material properties should behave significantly different than the experimental results used for comparison in [5].

During the extrusion process, the material temperature at the nozzle is generally between 200 to 280C [28, 32, 50-52]. ABS prints, therefore, experience a temperature range from room temperature to at least 200C. Most material properties are a function of temperature, with ABS being no exception [53]. The material properties used in the FEA model is detailed in Chapter 3.10.3. The properties given in the chapter are temperature dependent, which increases the model's accuracy overall in comparison to previous efforts that used isothermal properties.

Several studies mentioned in Sections 3.12 and 3.13 show that orientation can have a significant effect on the final strength of the AM part. However, pure ABS tends to have more consistent properties regardless of orientation [11]. ABS/fiber materials tend to have greater differences in strength in the final part based on the orientation of the deposition and orientation of fibers. That is one of the bigger differences between pure ABS and ABS/fiber material, as the pure ABS tends to have more isotropic properties through the weld material versus the anisotropic properties through the weld for ABS/fiber materials. For typical material extrusion applications, the weakest orientation is in the Z-direction. This is due to the reduced weld and gaps between stacked layers. However, the bead is more oval-shaped for BAAM applications and has greater contact. Therefore, layer welding with the layers above and below the neighboring beads leads to improved mechanical properties in the Z-direction [11, 16, 88]. The material properties in the Z-direction are more significant to this study since the build is only one layer thick. It also can be expected that the short time between layer deposition improves the

weld and, therefore, mechanical properties for stacked layers, making the properties of each orientation more consistent. Therefore, the material properties are assumed to be isotropic for this study. For ABS/fiber material the fibers tend to align during extrusion and create greater strength in the deposition direction. However, since this study looks at a one bead thick build, and the fibers do not contribute the strength of the weld between layers, it can be assumed that the material has properties equal to that the pure ABS properties that make up the weld.

4.3.5 Experiment

Two different devices were used to record the experimental build progress in [5] for comparison with the model results. First, to measure the build progress, a Nest Drop Cam was used for a visual recording of the build. The Nest camera recording was also used to retrieve the printing layer time for any given layer in the build. The second device used for recording utilized a FLIR E60 thermal imaging camera to capture the temperature history. The IR camera captured the thermographic profile of the build. The camera was paired with a computer running the FLIR Tools software package to record, save, and later analyze the thermographic history [5]. Figure 4-16 shows a diagram of the build platform and the location of the monitoring during the printing. After the build was completed, to measure the deflection of the experimental builds, each completed print was laser scanned using a 9-foot Faro Platinum portable CMM arm equipped with a Faro Blue Line laser scanner (or Faro CMM). The data was captured and analyzed using Polyworks Inspector 2017 software [5].

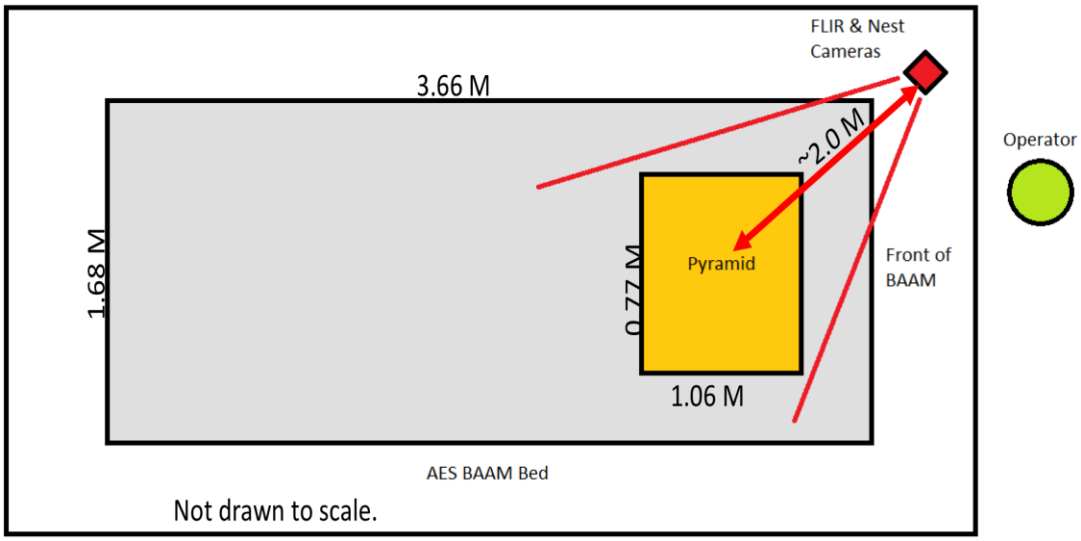

Figure 4-16. Schematic representation of the location of the printing and thermal recording devices [5].

4.4 Results and Discussion – Thermal Analysis

Figure 4-17 shows the thermography image for the build in mid-fabrication, after approximately 25 layers [5]. Emissivity settings used in the thermography was 0.87. It can easily be seen that the temperature decreases exponentially from the top layer until it reaches the constant temperature base plate (as seen in Figure 4-21). This is consistent with what has been seen in similar studies [79, 99, 102-104].

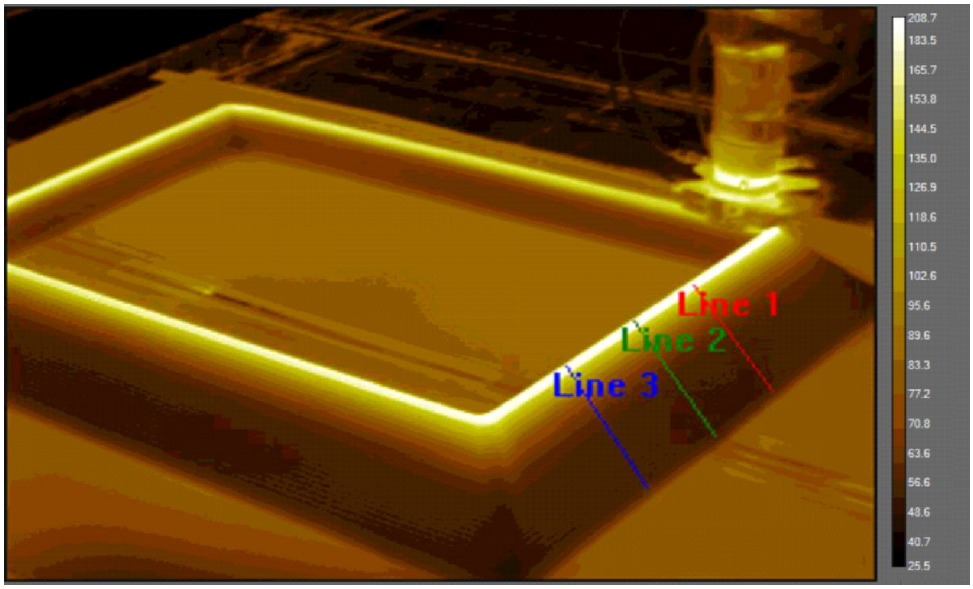

Figure 4-17. Infrared imaging of the fabrication with three vertical thermal profiles in Celsius [5].

The results from the thermal simulation are shown in Figure 4-18. The temperature varies from 200°C to 50°C from the top to the bottom layer [5].

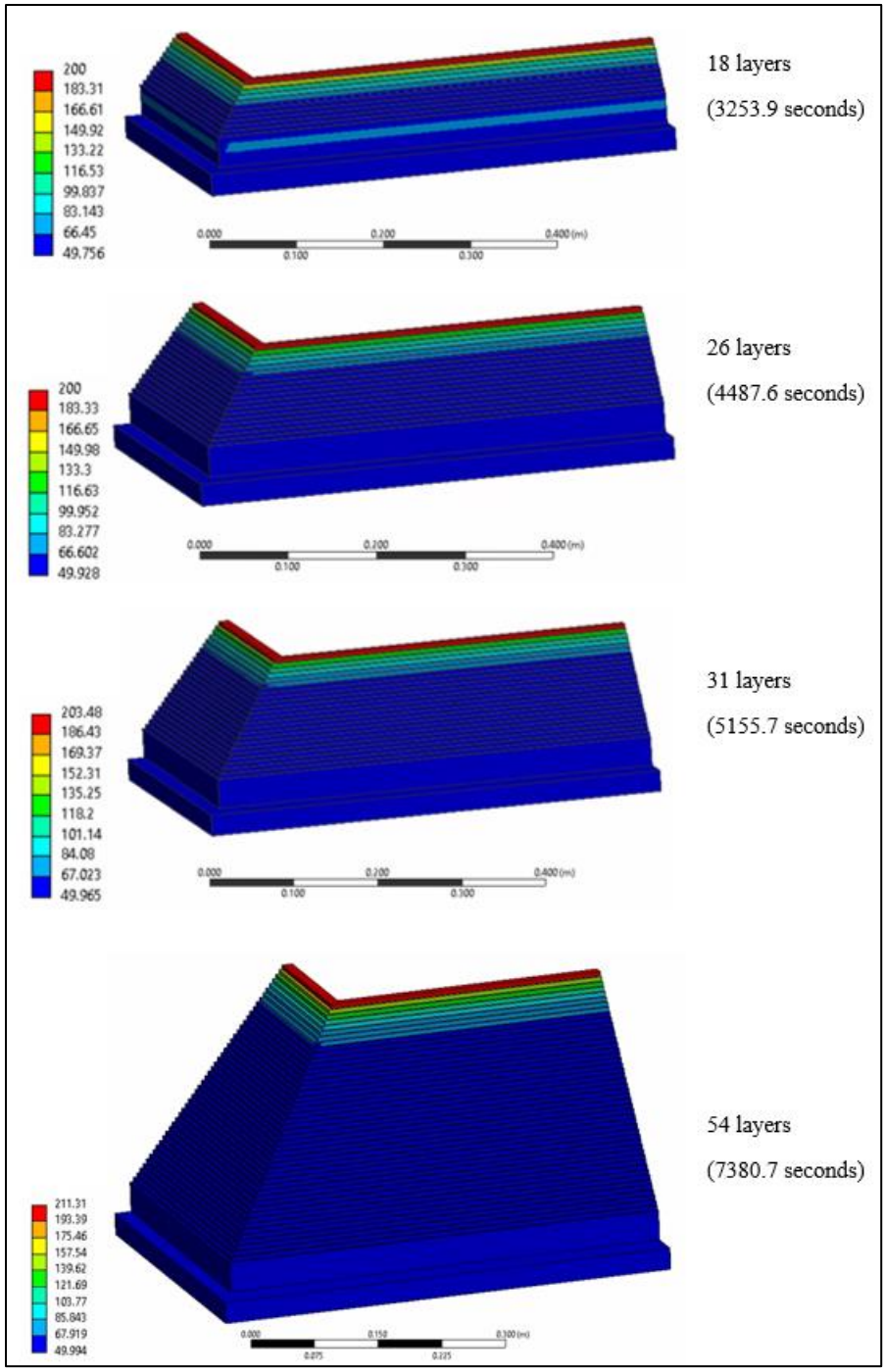

Figure 4-18. Temperature profile at different stages in the build.

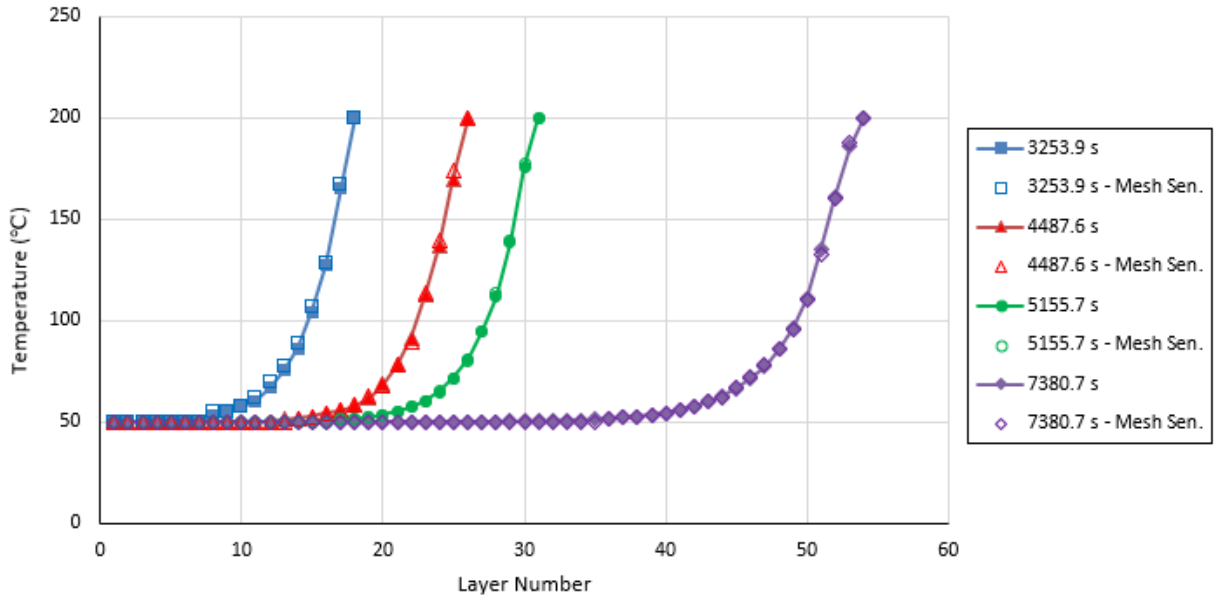

Figure 4-19. Thermal profile results of the FEA model – results gathered at 18 layers (3253.9 seconds), 26 layers (4487.6 seconds), 31 layers (5155.7 seconds), and 54 layers (7380.7 seconds). Mesh sensitivity results are also included for each of the results, indicated by the open markers.

The transient thermal analysis also shows that as the simulation height increases, the heat retained in lower layers increases. For example, when the model is only eighteen layers tall only a few immediate layers under the recently deposited layer are above the glass transition temperature. As the model increases to the fifty-third layer, roughly seven preceding layers are above the glass transition temperature, as shown in Figure 4-20. The model results show in Figure 4-20 that as the model increases in height and the layer deposition speed increases (due to the decreased road distance), the number of layers still above the glass transition temperature increases.

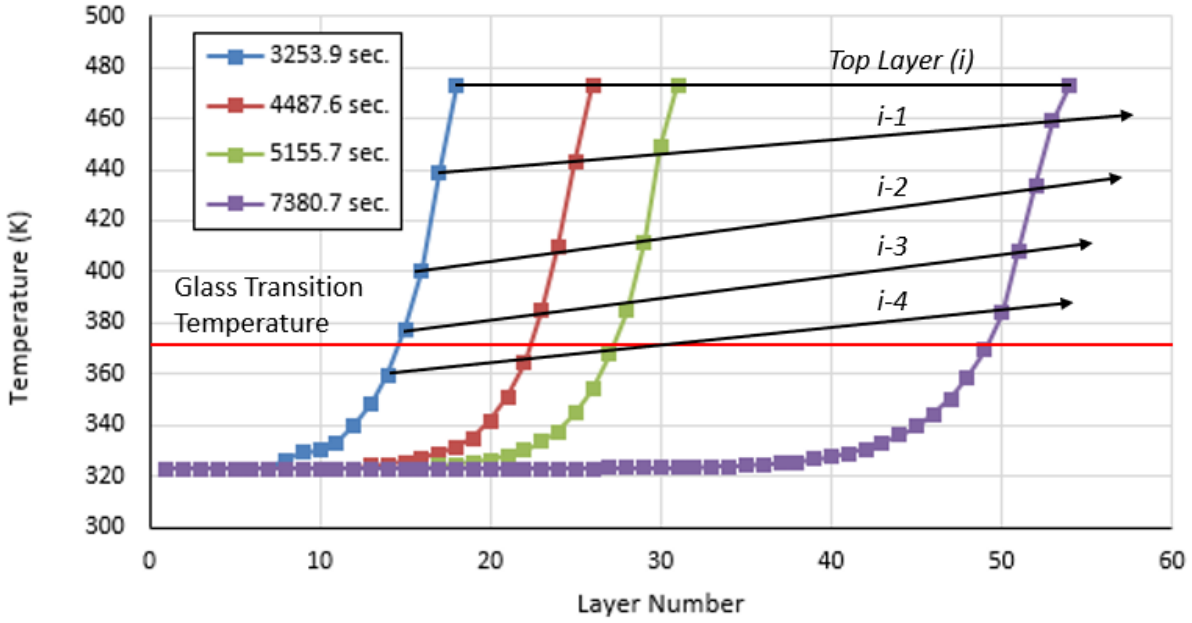

Figure 4-20. Thermal simulation results show an increase in heat retention of the immediate layers as a function of layer number.

Figure 4-21 shows a plot comparing the print layer to the corresponding temperature for the model and experimental data shown in Figure 4-17 after 25 layers have been printed. This plot illustrates the accuracy of the simulation of temperature. The model results are shown to be within 5 % of the experimental results. This confirms that the model can predict the temperature profile of an experimentally printed part.

The model is further validated by the mesh sensitivity study, which shows a maximum percent difference of 2%. This shows that the model's original mesh is satisfactory in predicting the temperature profile of the build.

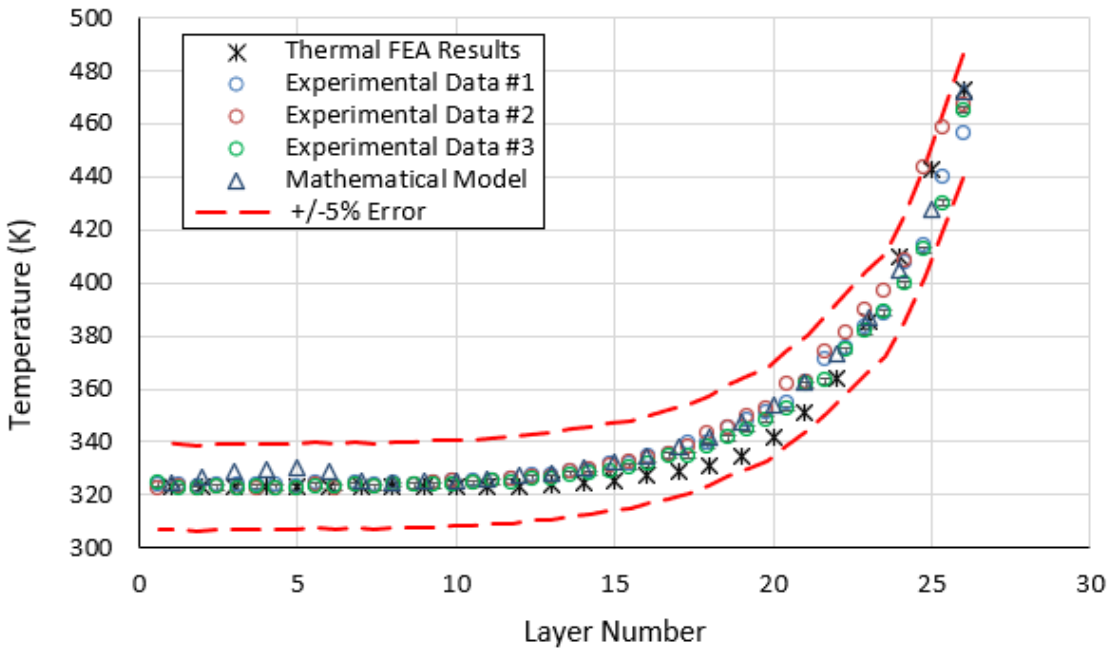

Figure 4-21. Comparison of the thermal model to the three lines identified in Figure 4-17.

Figure 4-17, shows that the thermal images captured three different vertical lines traversing all existing layers. Each pixel that makes up the lines recorded the temperature at that location on the structure. The data taken from the three lines and the thermal simulation show that the cooling present in the structure given in terms of temperature versus layer number follows an exponential form from the top layer to the bottom layer. Exponential cooling is often considered ideal for builds, as it allows for most of the lower layers to have low temperature material properties to structurally stabilize the base while only a few layers will be at higher temperatures (i.e., low mechanical strength properties) near the top of the build. The high temperature layers near the top are needed for proper welding for new layers. In this case, the building design utilizes an overhanging feature that reduces size as more layers are built. As the layer paths get smaller, the time to cool reduces, and more heat is added with subsequent layers.

Even though there is exponential cooling present, the cooling is insufficient to produce sufficiently stable layers before additional layers are added at the top layer and slumping occurs, as seen in Figure 4-1.

The results show how critical it is to have a smaller thermal mass when printing overhanging features. It can also be inferred that the exponential cooling is ideal for the printing process, as shown by how tall the build got before its collapse [5]. As the printed part adds additional layers, the base layers need to have solidified sufficiently to avoid slumping. This allows for overhanging features to be restrained. The lower setting temperature also allows for minimal material displacement during the print, allowing for higher efficiency. Utilizing these modeling techniques will aid BAAM designers in identifying the conditions that have the potential to result in slumping. Slumping is explicitly dependent on wall thickness, overhanging geometry, and high-temperature retention.

4.5 Results and Discussion – Structural Analysis

The transient thermo-mechanical analysis can study the entire thermal history of a part created by AM. The thermal history can include everything from the heat retention created by the AM process to the thermal stresses formed during manufacturing, giving important insight into how the part will function in service. The structural analysis was completed to determine the distortion and stress created during printing a single bead thickness pyramid. The only loads that are applied to the model are gravity and the time-history thermal profile created by the model previously described and given in [6]. This time-dependent thermal profile creates cyclic thermal stresses as each layer is subsequently added. The heating and cooling cycles and large temperature gradients are seen along with the build's height for the model results shown in Figure 4-18. This cycling of heat input and large temperature gradients makes the material

expand and contract, creating thermal stresses in the build. These thermal expansion induced stresses cause the material to distort from the desired geometry. This distortion can be common with AM builds, as most are subjected to the thermal cycling and temperature gradients, like in References [45, 60, 99, 105-106]. The distortion results are shown on the model in Figure 4-22. The distortion shown in Figure 4-22 are the total deformation of the model in all directions (i.e., x ,y, z directions). Distortion is defined here as the total deviation between the between the expected position of the wall from the designed model and the actual position from the experimental build. The distortion increases along the edge of the pyramid as the number of layers increase the model's overall height. The center of the walls in the model, close to the symmetry planes, is shown in Figure 4-22 to distort in a similar qualitative manner to the experimental build shown in Figure 4-23 where the wall buckles in the positive and negative direction along with the build's height. Note that in Figure 4-22, the shape of the desired geometry is shown by the black outlines, but the actual position is shown by the colored solid. Therefore, when the deformation pushes away from the inside of the model (positive direction), the outline is not visible. When the deformation distorts the inside of the pyramid (negative direction), the outline is visible.

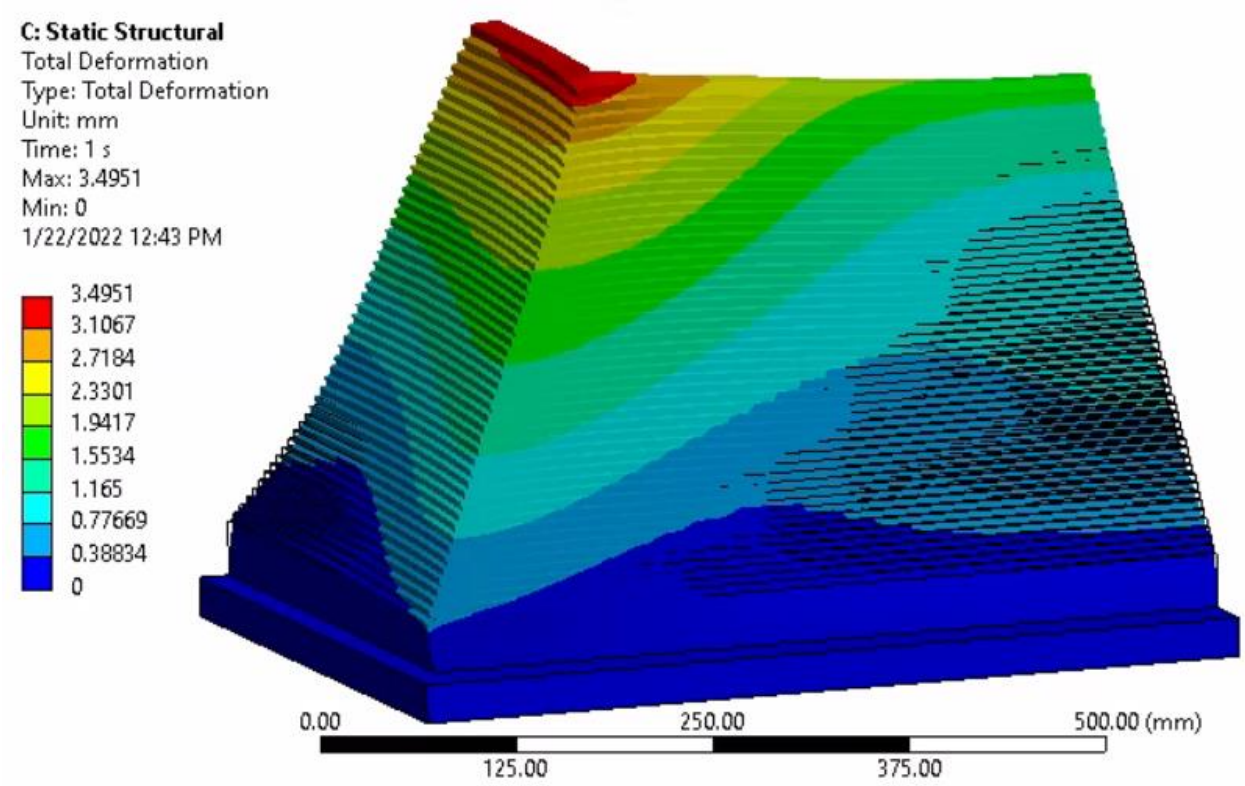

Figure 4-22. Distortion (shown in mm) mapped on the structural simulation model (deformation scale set to x24 to show distortion better).

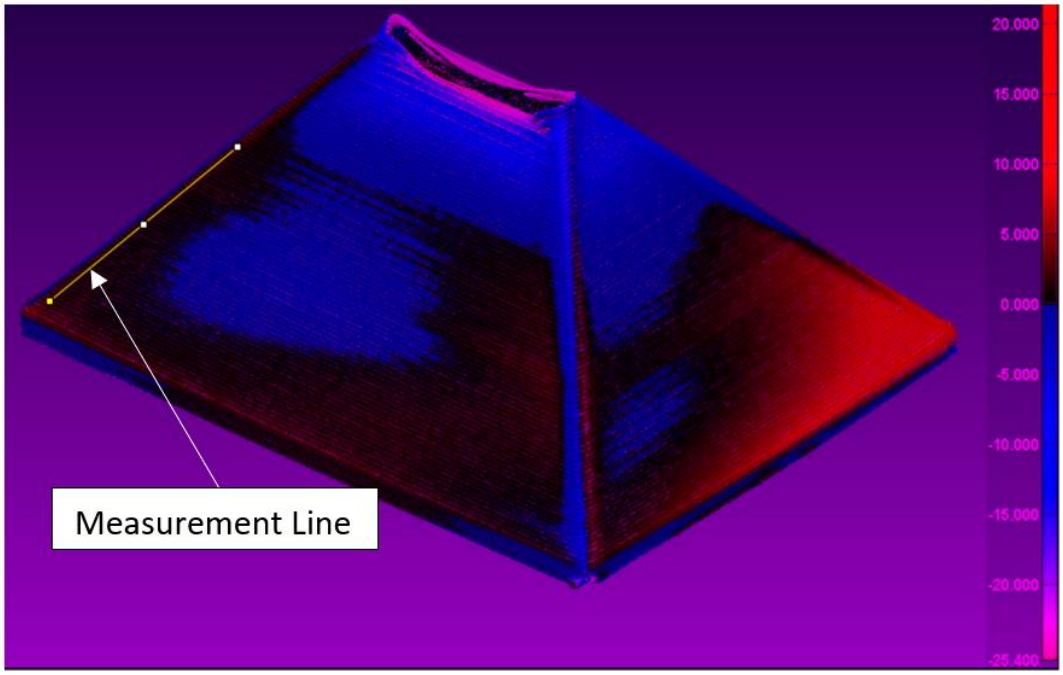

Figure 4-23. Experimental build 3D scan showing distortion of the build [5].

Once the experimental build terminated, the final structure was measured with a Faro CMM laser scanner to determine out-of-plane distortion during the build due to the printing process [5]. The out-of-plane distortion is the difference between the measured points from [5] and the designed geometry in terms of total distortion in the x, y, and z directions. Figure 4-24 shows the comparison between the structural simulation results and the experimental build. The line identified in Figure 4-23 shows where the data was gathered on the experimental build. Note this is not to the actual slumping point but instead to the area where there is gross deformation that is right before the slumping seems to start. Modeling past this point is subject for future work. The line pulls the out-of-plane distortion data between layer 14 to layer 53. Data points were selected from the structural simulation model to match the location of the experiment. Figure 4-24 shows the location on the line and layer number compared against the out-of-plane distortion of the build. As shown in Figure 4-24, the simulation and experimental results are in

good agreement. The error bars show the amount of variation (maximum and minimum values from each layer scanned) from the measurement of the experimental build. The variation is likely due to the internal and external corners of the experimental build as it is scanned creating local extremes in the dataset. The Faro CMM 3D scan shows greater data scatter due to the fine number of steps along the line and the high surface roughness or stepping effect of the printed pyramid. However, the average values from the measurement of the experimental build along the faces of each layer of the scanned surface are plotted in Figure 4-24 and are shown to be close to the values pulled from the same areas on the structural simulation. A short-range concentration of deformation around the pyramid's edges is also visible in Fig. 5. This deformation is assumed to be an artifact of the material extrusion process, where the corner has a small radius as the print head makes the turn around the corner instead of the perfect 90-degree corner used for the model simulation. This difference is expected to cause slight changes in distortion values for the immediate area.

Note that the model is further validated by the mesh sensitivity study, where the number of elements was doubled, shows a maximum percent difference of 6% between the results for the two meshes, as seen in Figure 4-24. This shows that the model's original mesh is satisfactory in predicting the distortion profile of the build.

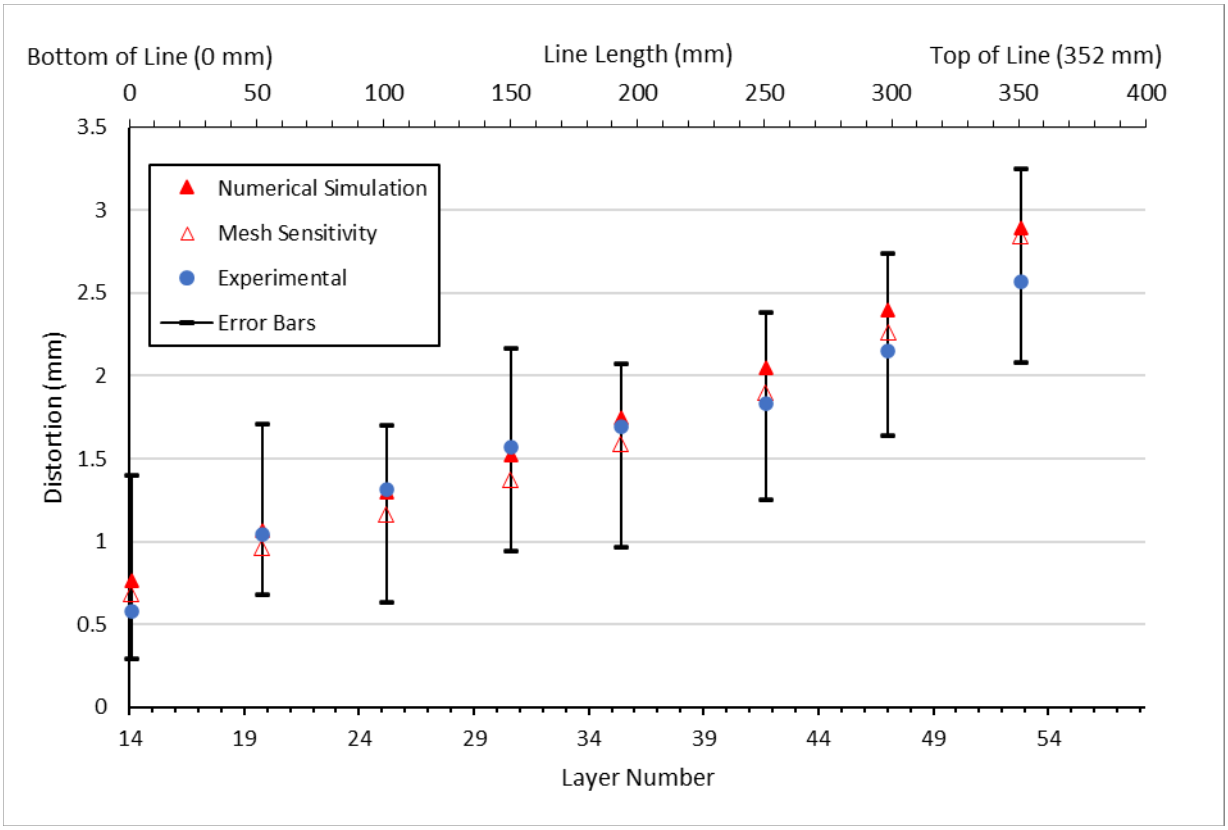

Figure 4-24. Comparison between the out-of-plane distortion versus layer number for the structural simulation and the experimental build.

Figure 4-24 shows that as the pyramid becomes taller, the out-of-plane distortion of the build becomes increasingly larger with greater distance from the desired geometry. As the distortion increases, the potential for undesirable final print geometry and even print failure increases.

The structural simulation also calculated the von-Mises stress during the build The von-Mises stress is mostly caused by the thermal induced stress and the weight of the build. The stress profile at the end of the simulation is shown in Figure 4-25. Figure 4-25 shows that the greatest stress occurs near the model's base, with little to no stress near the top layers. Since the greatest stress is around 16.847 MPa it is expected that there could be some distortion as the

local stress is close to the yield strength of the material. This finding is consistent with other simulation studies [95, 107-109]. The increased stress near the base is due to the rapid cooling causing material contraction near the top, causing the build's base to resist the stresses and results in the highest stress level. Structure weight also adds to the overall stresses seen in the system.

Conversely, the newly deposited layers have little stress as the material has enough heat retained to essentially stress relieve any of the stresses caused by the lower layers. The material properties of ABS at the temperatures in the top few layers are above the glass transition temperature, which does not allow residual stresses to increase to a significant level [55, 63, 110-111]. Additionally, the only substantial loads applied to the top layers are the weight of those layers.

As discussed in Section 4.4, the transient thermal analysis showed that as the number of layers added to the simulation increased with decreasing time to deposit, the number of preceding layers above the glass transition temperature would also increase. The number of layers with temperatures above the glass transition temperature has a significant effect on how to predict the slumping phenomenon. Section 3.10.3 discussed how the glass transition temperature, roughly 100°C for ABS, is the point where the material behaves as an easily deformable rubber so that most mechanical properties are reduced so significantly that they are essentially non-existent. As more layers are deposited, the weight of the structure also increases. These additional layers will eventually weigh enough to overcome the little mechanical stability that the lower layers possess. Therefore, as the height of the pyramid increases and there is no support material, the build will likely fail due to the slumping phenomenon.

This study shows that the most likely reasons for slumping to occur depend on (1) the combined weight of the layers above the layer that begins to fail, (2) if the temperature of those layers are significantly high enough for the material to still be in the rubbery region (i.e., above the glass transition temperature), and (3) the build geometry. The geometry is an important consideration, considering the greater the layers offset from each other, the less material can be welded. When the weld area is reduced significantly, the structure is not likely to support its weight due to the reduced contact area connecting the layers.

The glass transition temperature for ABS is around 95-110℃ [30, 55, 63, 72]. In Figure 4-18, once layer 54 is deposited, the thermal profile shows that the top 4 layers are above the glass transition temperature, and those layers show in Figure 4-25 very low levels of stress compared to the rest of the build. Figures 4-17 and 4-23 show the results for the experimental build while Figures 4-18 and 4-25 show the results for the simulations. Even though the model does not reach the slumping failure mechanism, when comparing the experimental and simulation results it can be seen that the increased heat retention leads to greater distortion which in turn leads to the slumping failure mechanism.

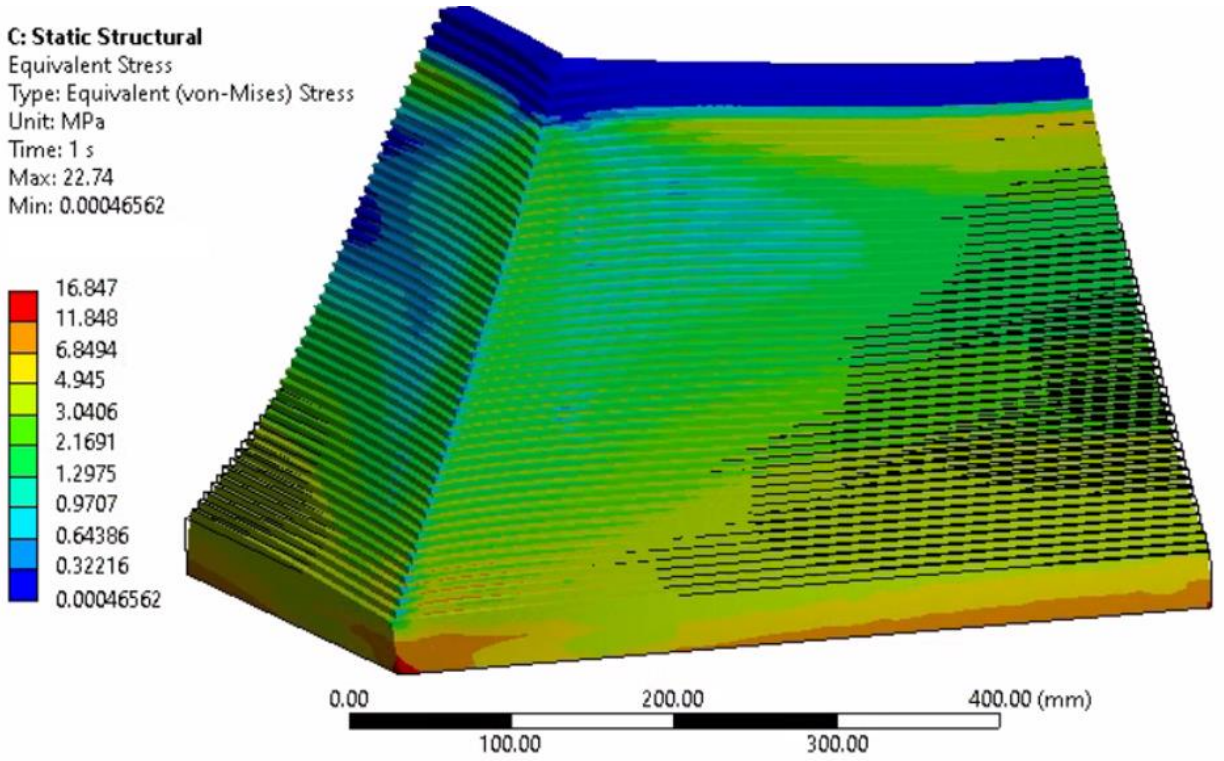

Figure 4-25. Von-Mises stress mapped on the structural simulation analysis (deformation scale set to x24 to show better distortion).

Build distortion is an additional contributor to cause the slumping failure. As shown in Figure 4-22, distortion increases near the top of the model. So as the top layer moves further away from the designed location, the print head typically cannot adjust to the new location of the last layer printed. This causes the new layer to be deposited in the incorrect location on the previous layer. In this case, the overhanging angle would be further increased, further weakening the structure contributing to the collapse by slumping.

This study is aimed at improving material extrusion AM builds. The work done here shows that simulating large builds before printing the structure can provide an understanding of how part failure occurs and be used to simulate a build. Use of this simulation method is expected to reduce overall part failure and increase the resolution of material extrusion builds.

The practical implications of this work apply to the consideration of the time it takes to extrude the material and the material costs that go into a build. If the failure happens at the end of the build, time and material are wasted. Therefore, upfront analysis and proper design are vital to quick and successful AM building.

4.6 Conclusion

This study produced a FEA model to predict the temperature profile of printed parts in terms of print layers using ABS material. The analysis also shows the structural stability of the part during the build process. The thermal model created accounted for conduction, convection, and radiation. Results from the thermal simulation are within 5% difference compared to the experimental data. The printed parts were monitored with cameras during fabrication to record in-situ thermal profiles, and geometrical deviations (or distortion) from the original design were measured in detail using a laser scanner. The results showed that the heat transfer during the printing process is an exponential trend for temperature versus layer number. This suggests that (1) when the print is near failure the previous layer has not sufficiently cooled to offer enough structural support for the next bead and (2) when the print is not near failure, exponential cooling from the top layer to the bottom layer is preferred since the lower setting temperature gives the print better structural performance when overhanging features are being printed.

This study also developed a structural simulation analysis to determine the deflection (or distortion) and thermal stress during the material extrusion AM build. The model was built utilizing symmetry and included temperature-dependent ABS material properties. The use of temperature dependent properties is shown in this work to improve the match between the simulation model and experiment. The results show that the deflection of the experimental build and the structural simulation are in good agreement. The stress analysis indicated that the

slumping failure mechanism is highly related to the geometry, heat retention, and material properties. This work can be used as a guide for modeling and creating a structural simulation for material extrusion AM using ABS or similar polymer materials to reduce the probability of print failure.

5 REFERENCES

[1] O. Abdulhameed, A. Al-Ahmari, W. Ameen and S. Hammad Mian, "Additive manufacturing: Challenges, trends, and applications," Advances in Mechanical Engineering, vol. 11, no. 2, pp. 1-27, 2019.

[2] T. D. Ngo, A. Kashani, G. Imbalzano, K. T. Q. Nguyen and D. Hui, "Additive manufacturing (3D printing): A review of materials, methods, applications and challenges," Composites Part B: Engineering, vol. 143, pp. 172-196, 2018.

[3] T.-M. Wang, J.-T. Xi and Y. Jin, "A model research for Prototype warp deformation in the FDM process," The International Journal of Advanced Manufacturing Technology, vol. 33, no. 11-12, pp. 1087-1096, 2006.

[4] A. Bhatia and A. K. Seghal, "Additive manufacturing materials, methods and applications: A review," Materials Today: Proceedings, In Proof.

[5] K. Choo, B. Friedrich, T. Daugherty, A. Schmidt, C. Patterson, M. A. Abraham, K. Rogers, P. Cortes and E. MacDonald, "Heat retention modeling of large area additive manufacturing," Additive Manufacturing, vol. 28, pp. 325-332, 2018.

[6] B. K. Friedrich and K. Choo, "Thermal Simulation of Big Area Additive Manufacturing," in Proceedings of the 7th International Conference on Fluid Flow, Heat and Mass Transfer (FFHMT'20), Niagara Falls, Canada, 2020.

[7] T. D'Amico and A. M. Peterson, "Bead parameterization of desktop and room-scale material extrusion additive manufacturing: How print speed and thermal properties affect heat transfer," Additive Manufacturing, vol. 34, 2020.

[8] V. Mechtcherine, F. P. Bos, A. Perrot, W. R. Leal da Silva, V. N. Nerella, S. Fataei, R. J. M. Wolfs, M. Sonebi and N. Roussel, "Extrusion-based additive manufacturing with cement-based materials – Production steps, processes, and their underlying physics: A review," Cement and Concrete Research, vol. 132, pp. 1-14, 2020.

[9] W. Li, A. Armani, A. Martin, B. Kroehler, A. Henderson, T. Huang, J. Watts, G. Hilmas and M. Leu, "Extrusion-based additive manufacturing of functionally graded ceramics," Journal of the European Ceramic Society, vol. 41, pp. 2049-2057, 2021.

[10] V. Kishore, C. Ajinjeru, A. Nycz, B. Post, J. Lindahl, V. Kunc and C. Duty, "Infrared preheating to improve interlayer strength of big area additive manufacturing (BAAM) components," Additive Manufacturing, vol. 14, pp. 7-12, 2017.

[11] C. Duty, V. Kunc, B. Compton, B. Post, D. Erdman, R. Smith, R. Lind, P. Lloyd and L. Love, "Structure and mechanical behavior of Big Area Additive Manufacturing (BAAM) materials," Rapid Prototyping Journal, vol. 23, no. 1, pp. 181-189, 2017.

[12] A. Roschli, K. T. Gaul, A. M. Boulger, B. K. Post, P. C. Chesser, L. Love, F. Blue and M. Borish, "Designing for Big Area Additive Manufacturing," Additive Manufacturing, vol. 25, pp. 275-285, 2019.

[13] S. Curran, P. Chambon, R. Lind, L. Love, R. Wagner, S. Whitted, D. Smith, B. Post, R. Graves, C. Blue, J. Green and M. Keller, "Big Area Additive Manufacturing and Hardware-in-the-Loop for Rapid Vehicle Powertrain Prototyping: A Case Study on the Development of a 3-D-Printed Shelby Cobra," in 2016 SAE World Congress, Detroit, MI, USA, 2016.

[14] N. Yaragatti and A. Patnaik, "A review on additive manufacturing of polymers composites," Materials Today: Proceedings, vol. 44, pp. 4150-4157, 2021.

[15] D.-A. Türk, Exploration and validation of integrated lightweight structures with additive manufacturing and fiber-reinforced polymers, ETH Zurich, 2017.

[16] J. Cantrell, S. Rohde, D. Damiani, R. Gurnani, L. DiSandro, J. Anton, A. Young, A. Jerez, D. Steinbach, C. Kroese and P. Ifju, "Experimental Characterization of the Mechanical Properties of 3D-Printed ABS and Polycarbonate Parts," Advancement of Optical Methods in Experimental Mechanics, vol. 3, pp. 89-105, 2016.

[17] ASTM Standard, F2792 - Standard Terminology for Additive Manufacturing Technologies, West Conshohocken: ASTM International, 2010.

[18] ISO / ASTM, 52900-15, Standard Terminology for Additive Manufacturing – General Principles – Terminology, West Conshohocken: ASTM International, 2015.

[19] "A timeline of 3D printing technology," Mechanical Engineering - The Magazine of ASME, [Online]. Available: https://www.asme.org/getmedia/3005f6dc-2618-4045-8445-da4242d41a46/infographic-a-timeline-of-3d-printing-technology_download.pdf?ext=.pdf. [Accessed 2021].

[20] A. I. Nurhudan, S. Supriadi, Y. Whulanza and A. S. Saragih, "Additive manufacturing of metallic based on extrusion process: A review," Journal of Manufacturing Processes, vol. 66, pp. 222-237, 2021.

[21] E. Castañeda, "Free-form architectural envelopes: Digital processes opportunities of industrial production at a reasonable price," Journal of Facade Design and Engineering, vol. 3, no. 1, pp. 1-13, 2015.

[22] J. Jafferson and D. Chatterjee, "A review on polymeric materials in additive manufacturing," Materials Today: Proceedings, Vols. 46, Part 2, pp. 1349-1365, 2021.

[23] D. B. Pedersen, Additive Manufacturing Multi Material Processing and Part Quality Control, The Technical University of Denmark, 2012.

[24] S. Zekovic, R. Dwivedi and R. Kovacevic, "Thermo-structural Finite Element Analysis of Direct Laser Metal Deposited Thin-Walled Structures," in 2005 International Solid Freeform Fabrication Symposium, 2005.

[25] I. Maskery and A. Thompson, Surface texture measurement of metal additively manufactured parts by X-ray computed tomography, University of Nottingham, 2019.

[26] B. Mummareddy, E. Burden, J. G. Carrillo, K. Myers, E. MacDonald, and P. Cortes, "Mechanical performance of lightweight ceramic structures via binder jetting of microspheres," SN Applied Sciences, vol. 3, no. 402, pp. 1-10, 2021.

[27] M. Spoerk, C. Holzer and J. Gonzalez-Gutierrez, "Material extrusion-based additive manufacturing of polypropylene: A review on how to improve dimensional inaccuracy and warpage," Journal of Applied Polymer Science, vol. 48545, pp. 1-16, 2019.

[28] B. N. Turner, R. Strong and S. A. Gold, "A review of melt extrusion additive manufacturing processes: I. process design and modeling," Rapid Prototyping Journal, vol. 20, no. 3, pp. 192-204, 2014.

[29] M. Pourali and A. Peterson, "Chapter 7 - Thermal Modeling of Material Extrusion Additive Manufacturing," American Chemical Society, pp. 1-16, 2019.

[30] M. Rahman, N. R. Schott and L. Kanta Sadhu, "Glass Transition of ABS in 3D Printing," in Proceedings of the 2016 COMSOL Conference, Boston, 2016.

[31] B. Graybill and A. Sherif El-Gizawy, Development of a Predictive Model for the Design of Parts Fabricated by Fused Deposition Modeling, Columbia, MO: University of Missouri--Columbia, 2010.

[32] A. Peterson, "Review of acrylonitrile butadiene styrene in fused filament fabrication: A plastics engineering-focused perspective," Additive Manufacturing, vol. 27, pp. 363-371, 2019.

[33] S. Park and K. Fu, "Polymer-based filament feedstock for additive manufacturing," Composites Science and Technology, vol. 213, no. 108876, 2021.

[34] F. Hajializadeh and A. Ince, "Finite element–based numerical modeling framework for additive manufacturing process," Material Design Process, vol. 28, pp. 1-7, 2018.

[35] K. Rane, M. Asad Farid, W. Hassan and M. Strano, "Effect of printing parameters on mechanical properties of extrusion-based additively manufactured ceramic parts," Ceramics International, vol. 47, pp. 12189-12198, 2021.

[36] K. Rane, S. Petrò and M. Strano, "Evolution of porosity and geometrical quality through the ceramic extrusion additive manufacturing process stages," Additive Manufacturing, vol. 32, pp. 1-111, 2020.

[37] H. Moustafa, "Highly flame retardant green composites using seashells," Plastics Research Online, pp. 1-4, 2016.

[38] M. Annoni, H. Giberti and M. Strano, "Feasibility Study of an Extrusion-based Direct Metal Additive Manufacturing Technique," Procedia Manufacturing, vol. 5, pp. 916-927, 2016.

[39] A. Perrot, D. Rangeard and A. Pierre, "Structural built-up of cement-based materials used for 3D-printing extrusion techniques," Materials and Structures, vol. 49, pp. 1213-1220, 2016.

[40] A. Perrot, D. Rangeard, V. Naidu Nerella and V. Mechtcherine, "Extrusion of cement-based materials - an overview," RILEM Technical Letters, 2018.

[41] C. Joh, J. Lee, T. Q. Bui, J. Park and I.-H. Yang, "Buildability and Mechanical Properties of 3D Printed Concrete," Materials, vol. 13, pp. 1-24, 2020.

[42] P. Song, Z. Cao and Q. Meng, "Effect of Lignin Incorporation and Reactive Compatibilization on the Morphological, Rheological, and Mechanical Properties of ABS Resin," Journal of Macromolecular Science Part B Physics, vol. 51, no. 4, pp. 720-735, 2012.

[43] V. E. Hutten, Process modeling of thermoplastics and thermosetting polymer matrix composites (PMCs) manufactured using fused deposition modeling, Dayton, Ohio, USA: University of Dayton, 2017.

[44] Y. Rao, N. Wei, S. Yao, K. Wang and Y. Peng, "A process-structure-performance modeling for thermoplastic polymers via material extrusion additive manufacturing," Additive Manufacturing, vol. 39, 2021.

[45] A. A. Samy, A. Golbang, E. Harkin-Jones, E. Archer, D. Tormey and A. McIllhagger, "Finite element analysis of residual stress and warpage in a 3D printed semi-crystalline polymer: Effect of ambient temperature and nozzle speed," Journal of Manufacturing Processes, vol. 70, pp. 389-399, 2021.

[46] S. Habib, "What Is ABS Plastic: How Is ABS Material Made: Key Properties of ABS: Applications of ABS Plastic: Advantages and Disadvantages of ABS Plastic," PlasticRanger, 11 August 2021. [Online]. Available: https://plasticranger.com/what-is-abs-plastic/. [Accessed 2021].

[47] A. En-Naji, N. Mouhib, M. Lahlou, H. Farid and M. El Ghorba, "Change of experimental Young's modulus with increasing temperature for an ABS material

subjected to tensile test," ARPN Journal of Engineering and Applied Sciences, vol. 14, no. 3, pp. 708-717, 2019.

[48] P. Lovell and J. Schork, "Fundamentals of Emulsion Polymerization," Biomacromolecules, vol. 21, no. 11, pp. 4396-4441, 2020.

[49] R. Auclair and R. Paul, "Emulsion polymerization process for ABS polyblends". United States Patent US4385157A, 1981.

[50] Y. Zhang and Y. Chou, "Three-dimensional finite element analysis simulations of the fused deposition modelling process," in Proc. IMechE Vol. 220 Part B: J. Engineering Manufacture, 2006.

[51] J. Wang and P. Papadopoulos, "Coupled thermomechanical analysis of fused deposition using the finite Coupled thermomechanical analysis of fused deposition using the finite," Finite Elements in Analysis and Design, vol. 197, pp. 1-21, 2021.

[52] A. Antony Samy, A. Golbang, E. Harkin-Jones, E. Archer and A. McIlhagger, "Prediction of part distortion in Fused Deposition Modelling (FDM) of semi-crystalline polymers via COMSOL: Effect of printing conditions," CIRP Journal of Manufacturing Science and Technology, vol. 33, pp. 443-453, 2021.

[53] S.-U. Zhang, J. Han and H.-W. Kang, "Temperature-Dependent Mechanical Properties of ABS Parts Fabricated by Fused Deposition Modeling and Vapor Smoothing," International Journal of Precision Engineering and Manufacturing, vol. 18, no. 5, pp. 763-769, 2017.

[54] R. V. Morgan, R. S. Reid, A. M. Baker, B. Lucero and J. D. Bernardin, "Emissivity Measurements of Additively Manufactured Materials," Los Alamos National Laboratory, 2017.

[55] Z. Weng, J. Wang, T. Senthil and L. Wu, "Mechanical and thermal properties of ABS/montmorillonite nanocomposites for fused deposition modeling 3D printing," Materials and Design, vol. 102, pp. 276-283, 2016.

[56] Z. Dobkowski, "Thermal analysis techniques for characterization of polymer materials," Polymer Degradation and Stability, vol. 91, pp. 488-493, 2006.

[57] W. M. Groenewoud, Characterization of Polymers by Thermal Analysis, New York: Elsevier Science, 2001.

[58] M. Nikzad, S. Masood and I. Sbarski, "Thermo-mechanical properties of a highly filled polymeric composites for Fused Deposition Modeling," Materials and Design, vol. 32, pp. 3448-3456, 2011.

[59] Omnexus: The Material Selection Platform, "Coefficient of Linear Thermal Expansion," Omnexus, 2022. [Online]. Available: https://omnexus.specialchem.com/polymer-properties/properties/coefficient-of-linear-thermal-expansion. [Accessed 02 03 2022].

[60] E. R. Fitzharris, N. Watanabe, D. W. Rosen and M. L. Shofner, "Effects of material properties on warpage in fused deposition modeling parts," International Journal of Advanced Manufacturing Technology, vol. 95, pp. 2059-2070, 2018.

[61] R. Sepe, A. Greco, A. De Luca, F. Caputo and F. Berto, "Influence of thermo-mechanical material properties on the structural response of a welded butt-joint by FEM simulation and experimental tests," Forces in Mechanics, vol. 4, no. 100018, pp. 1-16, 2021.

[62] W. Callister and D. Rethwisch, Fundamentals of Materials Science and Engineering: An Integrated Approach, Danvers: John Wiley & Son, Inc, 2008.

[63] A. Cattenone, S. Morganti, G. Alaimo and F. Auricchio, "Finite Element Analysis of Additive Manufacturing Based on Fused Deposition Modeling: Distortions Prediction Modeling: Distortions Prediction Modeling: Distortions Prediction Experimental Data," Journal of Manufacturing Science and Engineering, vol. 141, no. 011010, pp. 1-17, 2019.

[64] TORAY Group, "TOYOLAC™ ABS RESIN," TORAY Group, 2019. [Online]. Available: https://www.toray.jp/plastics/en/toyolac/technical/tec_006.html. [Accessed 2021].

[65] Y. A. Cengel and A. J. Ghajar, Heat and Mass Transfer - Fundamentals and Applications, New York, NY: McGraw Hill, 2015.

[66] N. Yuksel, Insulation Materials in Context of Sustainability, London: IntechOpen, 2016.

[67] W. dos Santos, J. de Sousa and R. Gregorio, "Thermal conductivity behavior of polymers around glass transition and crystalline melting temperatures," transition and crystalline melting temperatures, vol. 32, pp. 987-994, 2013.

[68] C. Kneidinger, M. Langauer, G. Zitzenbacher, S. Schuschnigg and J. Miethlinger, "Modeling and Estimation of the Pressure and Temperature dependent Bulk Density of Polymers," International Polymer Processing, vol. 35, no. 1, pp. 70-82, 2020.

[69] Cycolac, Sabic, ABS Density Response to Increasing Temperature, Data Provided Via Email., Sabic, 2021.

[70] J. Wang, "PVT Properties of Polymers for Injection Molding," in Some Critical Issues for Injection, Shanghai, InTech, 2012, pp. 1-30.

[71] G. T. Dee, T. Ougizawa and D. J. Walsh, "The pressure-volume-temperature properties of polyethylene, poly(dimethyl siloxane), poly(ethylene glycol) and poly (propylene

glycol) as a function of molecular weight," Polymer, vol. 33, no. 16, pp. 3462-3469, 1992.

[72] J. Menczel and R. B. Prime, Thermal Analysis of Polymers - Fundamentals and Applications, Hoboken, New Jersey: John Wiley and Sons, Inc., 2009.

[73] J. Li, Y. Jia, T. Li, Z. Zhu, H. Zhou, X. Peng and S. Jiang, "Tensile Behavior of Acrylonitrile Butadiene Styrene at Different Temperatures," Advances in Polymer Technology, vol. 2020, pp. 1-10, 2019.

[74] J. Cha, H. Yong Song, K. Hyun and J. Sang Go, "Rheological measurement of the nonlinear viscoelasticity of the ABS polymer and numerical simulation of thermoforming process," The International Journal of Advanced Manufacturing Technology, vol. 107, pp. 2449-2464, 2020.

[75] K. Hyun, M. Wilhelm, C. O. Klein, K. S. Cho, J. N. Nam, K. H. Ahn, S. J. Lee, R. H. Ewoldt and G. H. Mckinley, "A review of nonlinear oscillatory shear tests: Analysis and application of large amplitude oscillatory shear (LAOS)," Progress in Polymer Science, vol. 36, pp. 1697-1753, 2011.

[76] Instron, "Capillary Rheometer," Instron, [Online]. Available: https://www.instron.com/en/our-company/library/glossary/c/capillary-rheometer?region=Global%20Site. [Accessed 05 03 2022].

[77] T. Hofstaetter, R. Pimentel, D. B. Pedersen, M. Mischkot and H. N. Hansen, "Simulation of a Downsized FDM Nozzle," in COMSOL Conference 2015, Grenoble, 2015.

[78] B. Wang, G. Chang, X. Lin and W. Guo, "Analysis on Parameters of WLF Equation for Viscoelastic Damping Materials," in 4th International Conference on Mechanical Materials and Manufacturing Engineering, Wuhan, 2016.

[79] M. Roy, R. Yavari, C. Zhou, O. Wodo and P. Rao, "Prediction and Experimental Validation of Part Thermal History in the Fused Filament Fabrication Additive Manufacturing Process," Journal of Manufacturing Science and Engineering, vol. 141, 2019.

[80] S. Paul, "Finite element analysis in fused deposition modeling research: A literature review," Measurement, vol. 178, pp. 1-10, 2021.

[81] K. M. M. Billah, F. A. R. Lorenzana, N. L. Martinez, S. Chacon and R. B. Wicker, "Thermal Analysis of Thermoplastic Materials Filled with Chopped Fiber for Large Area 3D Printing," in Solid Freeform Fabrication, Austin, 2019.

[82] R. Wolfs and A. Suiker, "Structural failure during extrusion-based 3D printing processes," The International Journal of Advanced Manufacturing Technology, vol. 104, pp. 565-584, 2019.

[83] B. Compton, B. Post, C. Duty, L. Love and V. Kunc, "Thermal analysis of additive manufacturing of large-scale thermoplastic polymer composites," Additive Manufacturing, vol. 17, pp. 77-86, 2017.

[84] A. Garg and A. Bhattacharya, "An insight to the failure of FDM parts under tensile loading: finite element analysis and experimental study," International Journal of Mechanical Sciences, vol. 120, pp. 225-236, 2017.

[85] S. S. Babu, L. Love, R. Dehoff, P. William, T. Watkins and S. Pannala, "Opportunities and Challenges of Additive Manufacturing of Materials: Role of Economic Drivers,

Automation, Process Control, High Performance Computing and Neutron Characterization," Oak Ridge National Lab, Oak Ridge, TN, USA, 2015.

[86] S. S. Babu, L. Love, R. Dehoff, T. R. Watkins and S. Pannala, "Additive manufacturing of materials: Opportunities and challenges: Mrs. bulletin," Cambridge Core, 27 November 2015. [Online]. Available: https://www.cambridge.org/core/journals/mrs-bulletin/article/additive-manufacturing-of-materials-opportunities-and-challenges/80630AA7EDBE4DB562DE83249C4D12E2. [Accessed 2021].

[87] K. Pum, H. Baid, A. Hassen, A. Kumar, J. Lindahl, D. Hoskins, C. Ajinjeru, C. Duty, P. Yeole, U. Vaidya, F. Abdi, L. Love, S. Simunovic and V. Kunc, "Analysis on part distortion and residual stress in big Area additive manufacturing with Carbon fiber-reinforced thermoplastic using Dehomogenization Technique," 01 September 2019. [Online]. Available: https://www.osti.gov/servlets/purl/1607087. [Accessed 2021].

[88] C. S. Davis, K. E. Hillgartner, S. Hoon Han and J. E. Seppala, "Mechanical strength of welding zones produced by polymer extrusion additive manufacturing," Additive Manufacturing, vol. 16, pp. 162-166, 2017.

[89] R. Zou, Y. Xia, S. Liu, P. Hu, W. Hou and Q. Hu, "Isotropic and anisotropic elasticity and yielding of 3D printed material," Composites Part B, vol. 99, pp. 506-513, 2016.

[90] S. Bhandaria and R. Lopez-Anido, "Finite element analysis of thermoplastic polymer extrusion 3D printed material for mechanical property prediction," Additive Manufacturing, vol. 22, pp. 187-196, 2018.

[91] T. Webbe Kerekes, H. Lim, W. Yeol Joe and G. Jin Yun, "Characterization of process–deformation/damage property relationship of fused deposition modeling (FDM) 3D-printed specimens," Additive Manufacturing, vol. 25, pp. 523-544, 2019.

[92] N. Umetani and R. Schmidt, "Cross-sectional structural analysis for 3D printing optimization," SIGGRAPH Asia 2013 Technical Briefs, vol. 5, pp. 1-4, 2013.

[93] S. Guessasma, S. Belhabib, . H. Nouri and O. B. Hassana, "Anisotropic damage inferred to 3D printed polymers using fused deposition modelling and subject to severe compression," European Polymer Journal, vol. 85, pp. 324-340, 2016.

[94] Y. Lu, S. Zhu, Z. Zhao, T. Chen and J. Zeng, "Numerical simulation of residual stresses in aluminum alloy welded joints," Journal of Manufacturing Processes, vol. 50, pp. 380-393, 2020.

[95] X. Zhou, S.-J. Hsieha and Y. Sun, "Experimental and numerical investigation of the thermal behavior of polylactic acid during the fused deposition process," Virtual and Physical Prototyping, vol. 12, no. 3, pp. 221-233, 2017.

[96] L. Ji and T. Zhou, "Finite Element Simulation of Temperature field in Fused Deposition Modeling," Advanced Materials Research, Vols. 97-101, pp. 2585-2588, 2010.

[97] S. Costa, F. Duarte and J. Covas, "Thermal conditions affecting heat transfer in FDM/FFE: a contribution towards the numerical modelling of the process," Virtual and Physical Prototyping, pp. 1-12, 2014.

[98] K. Chou and Y. Zhang, "A parametric study of part distortions in fused deposition modelling using three-dimensional finite element analysis," Proceedings of the Institution of Mechanical Engineers, Part B: Journal of Engineering Manufacture, vol. 222, no. 8, pp. 959-968, 2008.

[99] H. Yang and S. Zhang, "Numerical simulation of temperature field and stress field in fused deposition modeling," Journal of Mechanical Science and Technology, vol. 32, no. 7, pp. 3337-3344, 2018.

[100] K. Hyun and M. Spalding, "Bulk Density of Solid Polymer Resins as a Function of Temperature and Pressure," Polymer Engineering and Science, vol. 30, no. 10, pp. 571-576, 1990.

[101] B. Bastian, E. Barocio, A. Favaloro, V. Kunc and R. B. Pipes, "Fused filament fabrication of fiber-reinforced polymers: a review," Additive Manufacturing, vol. 21, pp. 1-16, 2018.

[102] C. Kousiatza and D. Karalekas, "In-situ monitoring of strain and temperature distributions during fused deposition modeling process," Materials and Design, vol. 97, pp. 400-406, 2016.

[103] A.-D. Le, B. Cosson and A. Chateau Akue Asseko, "Simulation of large-scale additive manufacturing process with a single-phase level set method: a process parameters stud," The International Journal of Advanced Manufacturing Technology, vol. 113, pp. 3343-3360, 2021.

[104] J. Xiong, Y. Lei and R. Li, "Finite element analysis and experimental validation of thermal behavior for thin-walled parts in GMAW-based additive manufacturing with various substrate preheating temperatures," Applied Thermal Engineering, vol. 126, pp. 43-52, 2017.

[105] B. Shaqour, M. Abuabiah, S. Abdel-Fattah, A. Juidi, R. Abdallah, W. Abuzaina, M. Qarout, B. Verleije and P. Cos, "Gaining a better understanding of the extrusion process in fused filament fabrication 3d printing: a review," The International Journal of Advanced Manufacturing Technology, vol. 114, no. 1, pp. 1279-1291, 2021.

[106] N. Ramos, C. Mittermeier and J. Kiendl, "Experiments and numerical investigations on heat transfer in fused filament fabrication 3d printed specimens," The International Journal of Advanced Manufacturing Technology, vol. 118, no. 1, pp. 1367-1381, 2022.

[107] A. El Moumen, M. Tarfaoui and K. Lafdi, "Modelling of the temperature and residual stress fields during 3D Modelling of the temperature and residual stress fields during 3D," The International Journal of Advanced Manufacturing Technology, vol. 104, pp. 11661-1676, 2019.

[108] T. Mukherjee, V. Manvatkar, A. De and T. DebRoy, "Mitigation of thermal distortion during additive manufacturing," Scripta Materialia, vol. 127, pp. 79-83, 2017.

[109] E. Malekipour, S. Atteyoe and H. El-Mounayri, "Investigation of layer based thermal behavior in fused deposition modeling process by infrared thermography," in Procedia Manufacturing, Texas, USA, 2018.

[110] J. Fu and Y. Ma, "A Method to Predict Early-ejected Plastic Part Air-cooling Behavior towards Quality Mold Design and Less Molding Cycle Time," Robotics and Computer-Integrated Manufacturing, vol. 56, pp. 66-74, 2019.

[111] P. Sreejith, K. Kannan and K. Rajagopal, "A thermodynamic framework for additive manufacturing, using amorphous polymers, capable of predicting residual stress, warpage and shrinkage," International Journal of Engineering Science, vol. 159, no. 103412, pp. 1-23, 2021.

[112] W. Zhang, B. Cui, X. Gu, and Q. Dong, “Comparison of relaxation modulus converted from frequency- and time-dependent viscoelastic functions through numerical methods,” Applied Sciences, vol. 8, pp. 1-15, 2018.

[113] S. P. Madapusi, “A computational tool for numerical prediction of precision glass molding process,” Department of Mechanical Engineering, University of Florida, 2009.

Appendix I

Image Copyright Clearances

The following images have been previously published: Figure 3-24, Figure 3-25, and Figure 3-26. The novelty of the figures and any corresponding information is clearly referenced to the original authors. The image copyright clearances are shown in this appendix.

Clearance for Figures 3-24 and 3-25

EMERALD PUBLISHING LIMITED LICENSE
TERMS AND CONDITIONS

Mar 22, 2022

This Agreement between Youngstown State University -- Brian Friedrich ("You") and Emerald Publishing Limited ("Emerald Publishing Limited") consists of your license details and the terms and conditions provided by Emerald Publishing Limited and Copyright Clearance Center.

The publisher has provided special terms related to this request that can be found at the end of the Publisher's Terms and Conditions.

License Number	5274470833004
License date	Mar 22, 2022
Licensed Content Publisher	Emerald Publishing Limited
Licensed Content Publication	Rapid Prototyping Journal
Licensed Content Title	Structure and mechanical behavior of Big Area Additive Manufacturing (BAAM) materials
Licensed Content Author	Chad E. Duty, Vlastimil Kunc, Brett Compton, Brian Post, Donald Erdman, Rachel Smith, Randall Lind, Peter Lloyd, Lonnie Love
Licensed Content Date	Jan 16, 2017
Licensed Content Volume	23
Licensed Content Issue	1

	United States Attn: Youngstown State University
Publisher Tax ID	GB 665359306
Billing Type	Invoice
Type of Use	Dissertation/Thesis
Requestor type	Academic
Portion	Figures/table/illustration
Are you the author of the requested content?	No
Format	Print and electronic
Geographic Rights	World rights
Portion	Figures/table/illustration
Number of figures/tables	2
Will you be translating?	No
Number of copies	
Title	Numerical Simulation of a Failed Large Area Additive Manufacturing Build to Determine Thermal, Stress, and Distortion History
Institution name	Youngstown State University
Expected presentation date	Apr 2022
Portions	Figures 5 and 6
Requestor Location	Youngstown State University

Total 0.00 USD

Terms and Conditions

TERMS AND CONDITIONS

1. The publisher for this copyrighted material is Emerald Publishing Limited. By clicking "accept" in connection with completing this licensing transaction, you agree that the following terms and conditions apply to this transaction (along with the Billing and Payment terms and conditions established by Copyright Clearance Center, Inc. ("CCC"), at the time that you opened your RightsLink account and that are available at any time at http://myaccount.copyright.com).

2. Limited License. Publisher hereby grants to you a non-exclusive license to use this material. Licenses are for one-time use only with a maximum distribution equal to the number that you identified in the licensing process; any form of republication must be completed within 12 months from the date hereof (although copies prepared before then may be distributed thereafter).

3. Geographic Rights: Scope. Licenses may be exercised only in the geographic regions you identified in the licensing process.

4. Altering/Modifying Material: Not Permitted. You may not alter or modify the licensed material in any manner. For permission to translate the material into another language please contact permissions@emeraldinsight.com.

5. Reservation of Rights. Publisher reserves all rights not specifically granted in the combination of (i) the license details provided by you and accepted in the course of this licensing transaction, (ii) these terms and conditions and (iii) CCC's Billing and Payment terms and conditions.

6. License Contingent on Payment. While you may exercise the rights licensed immediately upon issuance of the license at the end of the licensing process for the transaction, provided that you have disclosed complete and accurate details of your proposed use, no license is finally effective unless and until full payment is received from you (either by publisher or by CCC) as provided in CCC's Billing and Payment terms and conditions. If full payment is not received on a timely basis, then any license preliminarily granted shall be deemed automatically revoked and shall be void as if never granted. Further, in the event that you breach any of these terms and conditions or any of CCC's Billing and Payment terms and conditions, the license is automatically revoked and shall be void as if never granted. Use of materials as described in a revoked license, as well as any use of the materials beyond the scope of an unrevoked license, may constitute copyright infringement and publisher reserves the right to take any and all action to protect its copyright in the materials.

7. Emerald always informs its authors of requests to republish their article. In the unlikely event that any author objects to the granting of the license to republish, Emerald reserves the right to revoke said license. The licensee will be informed and the license fee reimbursed within 10 working days.

8. Copyright notice: Disclaimer: You must include the following copyright and permission notice in connection with any reproduction of the licensed material and shall ensure that every published article gives due prominence on the title page to the original author/s, the journal title, volume, issue, page numbers and the copyright designation "© Emerald Publishing Limited all rights reserved."

9. Warranties: None. Publisher makes no representations or warranties with respect to the licensed material and adopts on its own behalf the limitations and disclaimers established by CCC on its behalf in its Billing and Payment terms and conditions for this licensing transaction.

10. Indemnity. You hereby indemnify and agree to hold harmless publisher and CCC, and their respective officers, directors, employees and agents, from and against any and all claims arising out of your use of the licensed material other than as specifically authorized pursuant to this license.

11. No Transfer of license. This license is personal to you and may not be sublicensed, assigned, or transferred by you to any other person without publisher's written permission.

12. No Amendment Except in Writing. This license may not be amended except in a writing signed by both parties (or, in the case of publisher, by CCC on publisher's behalf).

13. Objection to Contrary Terms: Publisher hereby objects to any terms contained in any purchase order, acknowledgment, check endorsement or other writing prepared by you, which terms are inconsistent with these terms and conditions or CCC's Billing and Payment terms and conditions. These terms and conditions, together with CCC's Billing and Payment terms and conditions (which are incorporated herein), comprise the entire agreement between you and publisher (and CCC) concerning this licensing transaction. In the event of any conflict between your obligations established by these terms and conditions and those established by CCC's Billing and Payment terms and conditions, these terms and conditions shall control.

14. Jurisdiction: This license transaction shall be governed by and construed in accordance with the laws of the United Kingdom. You hereby agree to submit to the jurisdiction of the courts located in the United Kingdom for purposes of resolving any disputes that may arise in connection with this licensing transaction.

15. Publisher (STM Signatory): Emerald is a signatory of the STM Permission Guidelines. Where, as part of this licensing transaction, you have indicated that you/your publisher is part of the STM Permissions Guidelines (by selecting 'Publisher (STM Signatory)', you warrant that the information included in the request is accurate and complete. Emerald requires you to complete the RightsLink process to obtain your license as proof of permissions cleared. Reuses falling within the limits of the STM Permissions Guidelines will be subject to a zero-rated (no fee) license. As per the terms of the STM Permission Guidelines, any license granted will apply to all subsequent editions and editions in other languages. All licenses falling outside of the limits of the guidelines may be subject to a permissions fee.

16. Special Terms: Should you submit your work for publication in the future, you will need to clear permission once more.

v 1.6

Questions? customercare@copyright.com or +1-855-239-3415 (toll free in the US) or +1-978-646-2777.

Clearance for Figure 3-26

ELSEVIER LICENSE
TERMS AND CONDITIONS

Mar 26, 2022

This Agreement between Youngstown State University -- Brian Friedrich ("You") and Elsevier ("Elsevier") consists of your license details and the terms and conditions provided by Elsevier and Copyright Clearance Center.

License Number	5276020328900
License date	Mar 25, 2022
Licensed Content Publisher	Elsevier
Licensed Content Publication	International Journal of Mechanical Sciences
Licensed Content Title	An insight to the failure of FDM parts under tensile loading: finite element analysis and experimental study
Licensed Content Author	Ashu Garg,Anirban Bhattacharya
Licensed Content Date	Jan 1, 2017
Licensed Content Volume	120
Licensed Content Issue	n/a
Licensed Content Pages	12
Start Page	225
End Page	236
Type of Use	reuse in a thesis/dissertation

Portion	figures/tables/illustrations
Number of figures/tables/illustrations	1
Format	both print and electronic
Are you the author of this Elsevier article?	No
Will you be translating?	No
Title	Numerical Simulation of a Failed Large Area Additive Manufacturing Build to Determine Thermal, Stress, and Distortion History
Institution name	Youngstown State University
Expected presentation date	Apr 2022
Portions	Fig 1
	Youngstown State University
Publisher Tax ID	98-0397604
Total	0.00 USD

Terms and Conditions

INTRODUCTION

1. The publisher for this copyrighted material is Elsevier. By clicking "accept" in connection with completing this licensing transaction, you agree that the following terms and conditions apply to this transaction (along with the Billing and Payment terms and conditions established by Copyright Clearance Center, Inc. ("CCC"), at the time that you opened your Rightslink account and that are available at any time at http://myaccount.copyright.com).

GENERAL TERMS

2. Elsevier hereby grants you permission to reproduce the aforementioned material subject to the terms and conditions indicated.

3. Acknowledgement: If any part of the material to be used (for example, figures) has appeared in our publication with credit or acknowledgement to another source, permission must also be sought from that source. If such permission is not obtained then that material may not be included in your publication/copies. Suitable acknowledgement to the source must be made, either as a footnote or in a reference list at the end of your publication, as follows:

"Reprinted from Publication title, Vol /edition number, Author(s), Title of article / title of chapter, Pages No., Copyright (Year), with permission from Elsevier [OR APPLICABLE SOCIETY COPYRIGHT OWNER]." Also Lancet special credit - "Reprinted from The Lancet, Vol. number, Author(s), Title of article, Pages No., Copyright (Year), with permission from Elsevier."

4. Reproduction of this material is confined to the purpose and/or media for which permission is hereby given.

5. Altering/Modifying Material: Not Permitted. However figures and illustrations may be altered/adapted minimally to serve your work. Any other abbreviations, additions, deletions and/or any other alterations shall be made only with prior written authorization of Elsevier Ltd. (Please contact Elsevier's permissions helpdesk here). No modifications can be made to any Lancet figures/tables and they must be reproduced in full.

6. If the permission fee for the requested use of our material is waived in this instance, please be advised that your future requests for Elsevier materials may attract a fee.

7. Reservation of Rights: Publisher reserves all rights not specifically granted in the combination of (i) the license details provided by you and accepted in the course of this licensing transaction, (ii) these terms and conditions and (iii) CCC's Billing and Payment terms and conditions.

8. License Contingent Upon Payment: While you may exercise the rights licensed immediately upon issuance of the license at the end of the licensing process for the transaction, provided that you have disclosed complete and accurate details of your proposed use, no license is finally effective unless and until full payment is received from you (either by publisher or by CCC) as provided in CCC's Billing and Payment terms and conditions. If full payment is not received on a timely basis, then any license preliminarily granted shall be deemed automatically revoked and shall be void as if never granted. Further, in the event that you breach any of these terms and conditions or any of CCC's Billing and Payment terms and conditions, the license is automatically revoked and shall be void as if never granted. Use of materials as described in a revoked license, as well as any use of the materials beyond the scope of an unrevoked license, may constitute copyright infringement and publisher reserves the right to take any and all action to protect its copyright in the materials.

9. Warranties: Publisher makes no representations or warranties with respect to the licensed material.

10. Indemnity: You hereby indemnify and agree to hold harmless publisher and CCC, and their respective officers, directors, employees and agents, from and against any and all claims arising out of your use of the licensed material other than as specifically authorized pursuant to this license.

11. No Transfer of License: This license is personal to you and may not be sublicensed, assigned, or transferred by you to any other person without publisher's written permission.

12. No Amendment Except in Writing: This license may not be amended except in a writing signed by both parties (or, in the case of publisher, by CCC on publisher's behalf).

13. Objection to Contrary Terms: Publisher hereby objects to any terms contained in any purchase order, acknowledgment, check endorsement or other writing prepared by you, which terms are inconsistent with these terms and conditions or CCC's Billing and Payment terms and conditions. These terms and conditions, together with CCC's Billing and Payment terms and conditions (which are incorporated herein), comprise the entire agreement between you and publisher (and CCC) concerning this licensing transaction. In the event of any conflict between your obligations established by these terms and conditions and those established by CCC's Billing and Payment terms and conditions, these terms and conditions shall control.

14. Revocation: Elsevier or Copyright Clearance Center may deny the permissions described in this License at their sole discretion, for any reason or no reason, with a full refund payable to you. Notice of such denial will be made using the contact information provided by you. Failure to receive such notice will not alter or invalidate the denial. In no event will Elsevier or Copyright Clearance Center be responsible or liable for any costs, expenses or damage incurred by you as a result of a denial of your permission request, other than a refund of the amount(s) paid by you to Elsevier and/or Copyright Clearance Center for denied permissions.

LIMITED LICENSE

The following terms and conditions apply only to specific license types:

15. **Translation**: This permission is granted for non-exclusive world **English** rights only unless your license was granted for translation rights. If you licensed translation rights you may only translate this content into the languages you requested. A professional translator must perform all translations and reproduce the content word for word preserving the integrity of the article.

16. **Posting licensed content on any Website**: The following terms and conditions apply as follows: Licensing material from an Elsevier journal: All content posted to the web site must maintain the copyright information line on the bottom of each image; A hyper-text must be included to the Homepage of the journal from which you are licensing at http://www.sciencedirect.com/science/journal/xxxxx or the Elsevier homepage for books at http://www.elsevier.com; Central Storage: This license does not include permission for a scanned version of the material to be stored in a central repository such as that provided by Heron/XanEdu.

Licensing material from an Elsevier book: A hyper-text link must be included to the Elsevier homepage at http://www.elsevier.com . All content posted to the web site must maintain the copyright information line on the bottom of each image.

Posting licensed content on Electronic reserve: In addition to the above the following clauses are applicable: The web site must be password-protected and made available only to bona fide students registered on a relevant course. This permission is granted for 1 year only. You may obtain a new license for future website posting.

17. **For journal authors:** the following clauses are applicable in addition to the above:

Preprints:

A preprint is an author's own write-up of research results and analysis, it has not been peer-reviewed, nor has it had any other value added to it by a publisher (such as formatting, copyright, technical enhancement etc.).

Authors can share their preprints anywhere at any time. Preprints should not be added to or enhanced in any way in order to appear more like, or to substitute for, the final versions of articles however authors can update their preprints on arXiv or RePEc with their Accepted Author Manuscript (see below).

If accepted for publication, we encourage authors to link from the preprint to their formal publication via its DOI. Millions of researchers have access to the formal publications on ScienceDirect, and so links will help users to find, access, cite and use the best available version. Please note that Cell Press, The Lancet and some society-owned have different preprint policies. Information on these policies is available on the journal homepage.

Accepted Author Manuscripts: An accepted author manuscript is the manuscript of an article that has been accepted for publication and which typically includes author-incorporated changes suggested during submission, peer review and editor-author communications.

Authors can share their accepted author manuscript:

- immediately
    - via their non-commercial person homepage or blog
    - by updating a preprint in arXiv or RePEc with the accepted manuscript
    - via their research institute or institutional repository for internal institutional uses or as part of an invitation-only research collaboration work-group
    - directly by providing copies to their students or to research collaborators for their personal use
    - for private scholarly sharing as part of an invitation-only work group on commercial sites with which Elsevier has an agreement
- After the embargo period
    - via non-commercial hosting platforms such as their institutional repository
    - via commercial sites with which Elsevier has an agreement

In all cases accepted manuscripts should:

- link to the formal publication via its DOI
- bear a CC-BY-NC-ND license - this is easy to do
- if aggregated with other manuscripts, for example in a repository or other site, be shared in alignment with our hosting policy not be added to or enhanced in any way to appear more like, or to substitute for, the published journal article.

Published journal article (JPA): A published journal article (PJA) is the definitive final record of published research that appears or will appear in the journal and embodies all value-adding publishing activities including peer review co-ordination, copy-editing, formatting, (if relevant) pagination and online enrichment.

Policies for sharing publishing journal articles differ for subscription and gold open access articles:

Subscription Articles: If you are an author, please share a link to your article rather than the full-text. Millions of researchers have access to the formal publications on ScienceDirect, and so links will help your users to find, access, cite, and use the best available version.

Theses and dissertations which contain embedded PJAs as part of the formal submission can be posted publicly by the awarding institution with DOI links back to the formal publications on ScienceDirect.

If you are affiliated with a library that subscribes to ScienceDirect you have additional private sharing rights for others' research accessed under that agreement. This includes use for classroom teaching and internal training at the institution (including use in course packs and courseware programs), and inclusion of the article for grant funding purposes.

Gold Open Access Articles: May be shared according to the author-selected end-user license and should contain a CrossMark logo, the end user license, and a DOI link to the formal publication on ScienceDirect.

Please refer to Elsevier's posting policy for further information.

18. **For book authors** the following clauses are applicable in addition to the above: Authors are permitted to place a brief summary of their work online only. You are not allowed to download and post the published electronic version of your chapter, nor may you scan the printed edition to create an electronic version. **Posting to a repository:** Authors are permitted to post a summary of their chapter only in their institution's repository.

19. **Thesis/Dissertation**: If your license is for use in a thesis/dissertation your thesis may be submitted to your institution in either print or electronic form. Should your thesis be published commercially, please reapply for permission. These requirements include permission for the Library and Archives of Canada to supply single copies, on demand, of the complete thesis and include permission for Proquest/UMI to supply single copies, on demand, of the complete thesis. Should your thesis be published commercially, please reapply for permission. Theses and dissertations which contain embedded PJAs as part of the formal submission can be posted publicly by the awarding institution with DOI links back to the formal publications on ScienceDirect.

Posting or linking by commercial companies for use by customers of those companies.

20. **Other Conditions**:

v1.10

Questions? customercare@copyright.com or +1-855-239-3415 (toll free in the US) or +1-978-646-2777.
